

**MULTIPARAMETRIC MRI OF THE PEDIATRIC SPINAL CORD:
APPLICATION, DEVELOPMENT, AND QUANTITATIVE
MEASUREMENTS OF NORMAL AND PEDIATRIC
SUBJECTS WITH SPINAL
CORD INJURY**

A Dissertation
Submitted to
the Temple University Graduate Board

In Partial Fulfillment
of the Requirements for the Degree
DOCTOR OF PHILOSOPHY

by
Shiva Shahrampour
August 2023

Examining Committee Members:

Nancy Pleshko, Ph.D., Advisory Chair, Department of Bioengineering
Feroze B. Mohamed, Ph.D., Thomas Jefferson University
Michel Lemay, Ph.D., Examining Chair, Department of Bioengineering
Laura Krisa, Ph.D., Thomas Jefferson University
Scott Faro, MD, Thomas Jefferson University

ABSTRACT

Quantitative magnetic resonance imaging (MRI) measurements of the pediatric spinal cord is important for both diagnostic and treatment planning. In recent years several quantitative MRI (qMRI) techniques that have been developed and tested to measure functional and structural information of the spinal cord tissue and microstructure. Several of the existing structural and functional imaging biomarkers (i.e., diffusion tensor imaging (DTI)) have demonstrated potential for providing microstructural information about the spinal cord. However, due to the lack of a standard anatomical template of the pediatric spinal cord, quantification of the spinal cord tissue has been challenging. Therefore, one of the goals of this work is to develop and test tools for quantification as well as the creation of a standard structural template of the typically developing (TD) pediatric spinal cord. This will allow automated measurement of normative values of the spinal cord cross-sectional area (SCCSA) at various levels of the spinal cord. Furthermore, to examine the white matter (WM) microstructure of the pediatric cord we developed a processing pipeline for the atlas-based generation of TD pediatric spinal cord WM tracts. This will facilitate the measurements of normative diffusion values for various WM tracts.

A group of 30 TD subjects (age range of 6-17 years old (12.38 ± 2.81)), who had no evidence of spinal cord injury or pathology were recruited. We utilized a multiparametric MRI protocol, including high-resolution $T2$ -w structural and diffusion-weighted MRI images to scan the subjects on a 3T MRI scanner. The diffusion data were acquired using a novel iFOV DTI sequence. For quantification, a post-processing pipeline was utilized to generate the structural pediatric template. Next, WM tracts were generated using an atlas-

based approach, and diffusion metrics (FA, MD, RD and AD) were quantified in 34 tracts identified in the processing pipeline. Normative SCCSA and DTI diffusion indices were generated for the TD population.

Lastly, we demonstrated that DTI indices (i.e. FA) can be a predictive measure of components of the clinical test for spinal cord injury, as well as an indicator of the white matter tracts integrity. Therefore, in the final step of this work, we expanded our quantitative analysis to look at the microstructural and macrostructural changes in 15 children with chronic spinal cord injury (SCI) (AIS A-D, mean age of 12.8 ± 3.1 years). This included measurements of SCCSA, diffusion metrics and T2* WM/GM ratio of various white matter tracts in the patient population. We also examined the relationships between all the metrics and the ISNCSCI clinical scores in SCI subjects. We then compared these measurements between the TD and SCI patients to evaluate the diagnostic utility of these techniques and biomarkers. Statistically significant difference was observed between the two populations in the studied metrics. The results show that the proposed techniques may have the potential to be used as surrogate biomarkers for the quantification of the injured spinal cord.

DEDICATION

*To my family,
who have embraced this long journey with me*

TABLE OF CONTENTS

	Page
ABSTRACT.....	ii
DEDICATION.....	iv
LIST OF TABLES.....	viii
LIST OF FIGURES	ix
 CHAPTER	
1. INTRODUCTION	1
1.1 Background.....	1
1.2 Anatomy of the spinal cord.....	2
1.2.1 Neurons and neuronal tissue	2
1.2.2 The human spinal cord structure and anatomy	3
1.3 Diseases/injuries affecting the spinal cord (Neurodegenerative disease, Traumatic injury).....	6
1.3.1 Traumatic Spinal Cord Injury (primary injury)	6
1.3.2 Traumatic Spinal Cord Injury (secondary injury)	8
1.3.3 Clinical Classification System for Spinal Cord Injury	10
1.4 Physics of Magnetic Resonance Imaging (MRI)	12
1.4.1 Spins and Magnetic Moments.....	13
1.4.2 Precession	14
1.4.3 The Bloch Equations and T1-weighted, T2-weighted MRI.....	16
1.4.4 MRI Pulse Sequences	18

1.4.5 Principles of Diffusion MRI	20
1.4.6 Diffusion Tensor Imaging (DTI)	23
2. STATE OF THE ART	27
2.1 Spinal Cord Quantitative MRI (qMRI).....	27
2.2 Spinal Cord MRI template and atlases	29
3. METHODOLOGY	39
3.1 Structure of the dissertation	40
3.2 Additional Publications	42
3.2.1 Peer-review journals	42
3.2.2 Conference abstracts	43
4. ARTICLE 1: DEVELOPMENT OF STANDARDIZED NORMATIVE PEDIATRIC SPINAL CORD STRUCTURAL TEMPLATE: DEMONSTRATION OF AUTOMATIC ESTIMATION OF SPINAL CORD CROSS SECTIONAL AREA MEASUREMENTS (SCCSA).....	46
Abstract.....	47
Objective and Background	48
Methods and Materials	48
Results.....	53
Conclusion	56
5. ARTICLE 2: ATLAS-BASED QUANTIFICATION OF DTI MEASURE IN A TYPICALLY DEVELOPING PEDIATRIC SPINAL CORD.....	57
Abstract	58
Introduction.....	58
Methods and Materials.....	61
Results.....	66

Discussion	74
Limitations	78
Conclusions.....	79
6. ARTICLE 3: QUANTITATIVE MAGNETIC RESONANCE IMAGING TO CHARACTERIZE THE MACRO AND MICROSTRUCTURAL CHANGES IN TYPICALLY DEVELOPING PEDIATRIC SUBJECTS AND PATIENTS WITH SPINAL CORD INJURY	80
Abstract	81
Introduction.....	82
Methods and Materials.....	84
Results.....	92
Discussion	99
Limitations of the study	104
Conclusion	105
7. CONCLUSION AND FUTURE WORK	107
BIBLIOGRAPHY.....	110
APPENDICES	
A. ASIA SCORING TEMPLATE.....	124
B. ROI NAMES.....	126
C. GROUP REGIONS NAMES	127
D. PERMISSION LETTER FOR INCLUSION OF COPYRIGHTED MATERIAL....	128

LIST OF TABLES

Table	Page
1. Table shows comparison of SCCSA (mm ²) measurements between the generated template and the average of all the 30 subjects along with Coefficient of Variation (CV) in selected intervertebral discs	56
2. Results of DTI normative values for 6 selected tracts illustrated in (figure 24-B)	71
3. The table illustrates the demographic of participants of this study (including 15 SCIs and 15TDs)	86

LIST OF FIGURES

Figure	Page
1. Schematic presentation of a neuron structure.....	3
2. Represents the structure of the human spinal cord.	4
3. Shows the cross-sectional view of the spinal cord white matter along with the sensory and motor tracts.....	6
4. Represent different phases of spinal cord injury (SCI)	9
5. ASIA scoring for neurological classification of the SCI.....	11
6. Illustrates precession of the proton in the magnetic field of (B0)	15
7. Illustrates two main magnetization patterns in MRI imaging.	17
8. Illustration of two common sequences in MRI.....	19
9. Illustrates water molecules movement in different environments.....	21
10. A schematic of the dMRI sequence.....	22
11. Ellipsoidal representation of the diffusion tensor field.	24
12. The template made by Stroman team in 2008.....	30
13. Template made by Eippert group in 2009.....	31
14. The templated created by Valsasina group in 2012.	32
15. The template figure from El Mendili et al. made in 2015.....	33
16. Illustrates the AMU40 template.	35
17. Illustrates MNI–Poly-AMU, T2-weighted template with vertebral labeling made by Fonov team (2014).....	36
18. T1-w and T2-w sagittal views of the PAM 50 template.....	37
19. Illustration of the structure of this thesis based on the chapters and the related specific aims of this thesis work.....	42
20. Illustrates a summary of template creation steps... ..	52

21. Illustrates the generated pediatric template.	54
22. The graph shows the comparison of the SCCSA measurements between the pediatric template and average of all the 30 subjects	55
23. Illustrates an overview of the template registration pipeline.	63
24. Illustrates the spinal cord WM atlas	67
25. Violin plots of normative FA (A), MD (B), AD (C), and RD (D) indices averaged across 30 healthy pediatric subjects for 34 ROIs.	69-70
26. Linear regression plots showing the relationship between age and FA (A), MD (B), AD (C), and RD (D) in the ventral, lateral, and dorsal funiculi.....	73
27. Illustrates a panel of qMRI metrics of our study demonstrating the measurements at C2-C3 level	90
28. Illustrates DTI metrics of FA (a, b), MD (c, d), RD (e, f) and AD (g, h) averaged across all TD and SCI subjects for 7 WM tracts showing mean and standard deviation bars.94
29. T2* WM/GM ratio averaged across all TD and SCI subjects for 7 WM tracts.	96
30. Violin plots of averaged cross-sectional area of the whole spinal cord (a,b), white matter(c,d), and gray matter(e,f) in all the15 SCI and 15 TD subjects...97	
31. Correlation matrix for MR imaging metrics.	99

CHAPTER 1

INTRODUCTION

1.1 Background

Magnetic Resonance Imaging (MRI) is a non-invasive medical imaging modality. It offers a powerful technique to monitor traumas affecting the spinal cord (i.e. traumatic and non-traumatic spinal cord injury). The unique advantages of MRI in evaluation of the spinal cord makes it an indispensable tool in the assessment of spinal cord injuries, tumors, and degenerative conditions. Particularly, spinal cord injury (SCI) which is a condition that arises from mechanical damage to the spinal cord resulting in disruption of the spinal cord column. Most of the current clinical MRI protocols for imaging the spinal cord in SCI rely on conventional techniques (i.e. detecting spinal cord atrophy) that lack the ability to study the spinal cord complications at the microstructural level. Quantitative MRI (qMRI), however, has huge potential to provide intrinsic and normative values to tissue properties that are useful for diagnosis, prognosis and monitoring the treatment progress.

Spinal cord is a signaling pathway between the extremities and the brain, and it plays a crucial role in the human body. The primary sensory and motor functions are conducted by the spinal cord which makes it a vector between the brain and the peripheral nervous system. Like other anatomical structures, the spinal cord can be affected by various complications (i.e.SCI) and neurodegenerative diseases such as Amyotrophic Lateral Sclerosis (ALS) and Multiple Sclerosis (MS). In particular, SCI is an insult to the spinal cord resulting in a temporary or permanent change, in the cord's normal motor, sensory, or autonomic function.

According to a report from the World Health Organization, the prevalence of spinal cord injury is estimated to be between 250,000 and 400,000 people in the United States , with an incidence of approximately 12,000 new cases per year [1]. The majority of spinal cord injuries occur in young men between the ages of 15 and 35, and the leading cause of spinal cord injuries is motor vehicle accidents. Other causes of spinal cord injuries include falls, violence, sports injuries, and medical malpractice. Novel qMRI techniques (e.g., diffusion imaging) were shown to provide efficient biomarkers can be utilized for diagnosis, prognosis and objective assessment of new treatments (i.e. drugs, nano-medicine)[2]–[4]. These techniques are sensitive to underlying microstructure and metabolism, hence providing insights into the pathogenesis of neurological diseases [5]. However, most of these techniques are not currently applied to the pediatric spinal cord studies, due to the smaller cord size in children and perhaps lack of appropriate image analysis tools dedicated to the children’s spinal cord.

1.2 Anatomy of the spinal cord

1.2.1 Neurons and neuronal tissue

Neurons are the fundamental structure of the nervous system. They comprise three parts: 1) the cell body, 2) dendrites, and 3) axon. The cell body contains the nucleus and other organelles responsible for the neuron's metabolic functions. Dendrites are small, branch-like structures that receive signals from other neurons or sensory receptors. The axon is a long projection that carries signals from the cell body and transmits them to other neurons or muscles or glands. The speed of axon transmission is raised by the insulator named myelin sheath (figure 1).

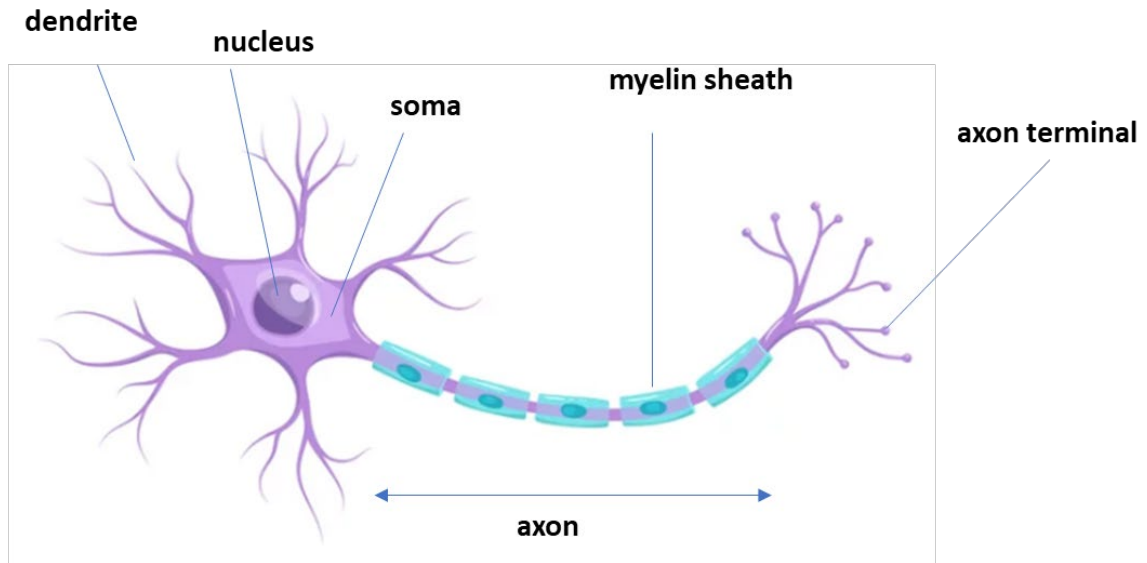


Figure 1: Illustration of a neuron, showing the soma (cell body), dendrites and an axon. Axons and dendrites are referred to as neurites. The figure was adapted from an image by L.Darin licensed via Adobe Stock <https://stock.adobe.com/>

Neurons contain various types of glial cells (i.e., astrocytes and oligodendrocytes). Glial cells help support the function of the neurons, like production of myelin and immune response. Neuronal tissue, on the other hand, is divided into gray matter (GM) and white matter (WM). GM embodies neuronal cell bodies, glial cells, as well as afferent and efferent myelinated and unmyelinated axons and capillaries. WM consists primarily of myelinated axons and connects the GM regions to other GM areas and to the periphery.

1.2.2. The human spinal cord structure and anatomy

The spinal cord is made up of 31 segments, each of which is associated with a pair of spinal nerves that emerge from the cord and innervate different parts of the body. The cord is divided into four regions: cervical (upper), thoracic (middle), lumbar (lower), and sacral

(bottom). The anatomical structure of the spinal cord consists of the butterfly-shaped region referred to as GM and bundles of ascending and descending pathways carrying the signal to the brain and peripheral nervous system known as WM. The spinal cord WM contains a wide range of fibers that are different in size, density, and functionality. A graphical representation of spinal cord anatomy is shown in (figure 2) (Standring 2008).

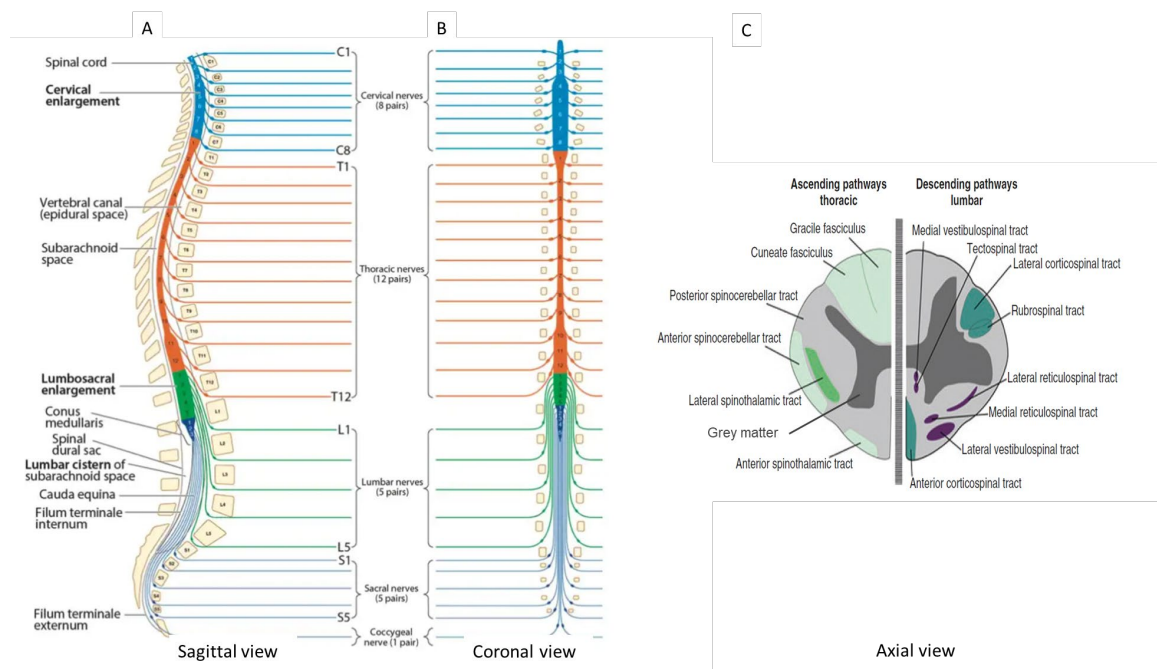


Figure 2: The structure of the human spinal cord . Representation of the vertebral levels and spinal segments (Sagittal view) (A), same representation in coronal view (B). Axial view of the cord showing gray matter and white matter along with the descending (motor) and ascending (sensory) tracts of the white matter adapted from (Standring 2008).

The WM of the spinal cord is essentially divided into 3 major columns: a) the dorsal column, b) the lateral spinal cord and c) the anterior column.

a) The dorsal column (posterior spinal cord): consists of ascending sensory pathways and

engages in two modes of proprioception; pressure and vibration sensation and epicritic touch (differentiation of two points). The Dorsal column consists of two pairs of fascicles: the left and right gracile fascicle of Goll (that transfers information from the lower body) and the cuneate fascicle of Burdach (sends information from the upper body).

b) The lateral spinal cord contains both ascending (sensory) and descending (motor) tracts. The sensory pathways transfer pain, temperature and gross touch information. These pathways consist of the spinoreticular, the spinocerebellar, the spinothalamic and the spinotectal fascicles. Whereas, the motor tracts of the lateral spinal column are corticospinal, reticulospinal fascicles and rubrospinal tracts. These descending pathways control voluntary movements.

c) The anterior cord also consists of ascending and descending pathways. The ascending spinotectal tract of the anterior cord is responsible for reflex of eye and head movements. The spino-olivary sensory tract is responsible for relaying light touch information to the cerebellum and the ascending ventral spinothalamic tract transfers the deep touch and pressure sensations. The motor pathways of the anterior cord are comprised of vestibulospinal, medial reticulospinal and anterior corticospinal tracts. All these 3 motor tracts are responsible for movement control. A cross-sectional view of the spinal cord with all the detailed WM tracts is presented in (figure 3) (Deer 2019).

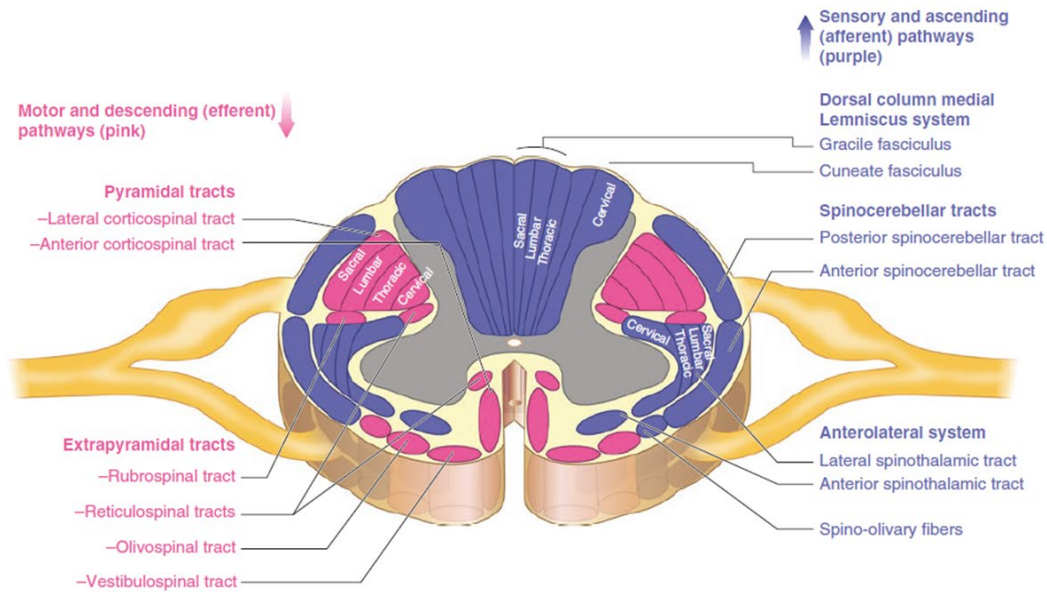


Figure 3: The cross-sectional view of the spinal cord white matter along with the sensory and motor tracts. (adapted from (Deer 2019)).

1.3 Diseases/injuries affecting the spinal cord (Neurodegenerative disease, Traumatic injury)

1.3.1 Traumatic Spinal Cord Injury (primary injury):

As mentioned before, despite its small size, the spinal cord has major functions such as sending motor commands from the brain to the body and sensory information from the body to the brain, and coordinating reflexes. Therefore, pathologies associated with the spinal cord can have severe consequences on these vital functions. As there are various known spinal cord complications, study of spinal cord WM and characterizing its microstructure is essentially helpful in early diagnosis of disease and pathologies (i.e. autoimmune or neurodegenerative diseases). Neurodegenerative diseases are a group of disorders that involve the progressive loss of function and affect the neurons in the brain and/or spinal cord. Some common examples of spinal cord neurodegenerative diseases

include; Amyotrophic lateral sclerosis (ALS) and Multiple sclerosis which is an autoimmune disorder that affects the myelin sheath that surrounds the nerve fibers in the spinal cord. Injury to the spinal cord can result from both traumatic and non-traumatic processes. Traumatic spinal cord injury (tSCI) is a condition that affects the spinal cord after a traumatic event (i.e. motor-vehicle accidents). The initial mechanical forces inserted to the spinal cord at the time of injury is known as *primary injury* which is identified by four different characteristic mechanisms. The primary injury is where there's "disc materials and bone fragments or tear into the spinal cord tissue" [6]–[8]. When the spinal cord is subjected to a sudden and severe impact, the vertebrae may fracture or dislocate, causing damage to the spinal cord. The most common type of primary injury is *impact plus persistent compression*, which happens through bone fragments compressing the spinal cord or through fracture-dislocation injuries [7], [9], [10]. Regardless of the form of the primary injury, the mechanical insult to the cord damages the WM pathways and disrupts blood vessels and cell membranes[4], [11]. This can result in spinal block, vasospasm, ischemia, systemic hypotension and neurotransmitter accumulation[12]. Therefore, it's paramount to understand the underlying cellular and molecular mechanisms at the microstructural level in SCIs to enhance the effective treatments for this condition. In general, the severity and location of the injury (i.e. extent of primary injury) determines the clinical outcomes of the SCI which could result in partial or complete loss of sensory and/or motor functions in these patients. Overall, SCIs are divided into either *complete* or *incomplete*. Patients with *incomplete* injuries preserve some functions, whereas neurological assessments show no spared motor/sensory functions below the level of injury in *complete* patients[13].

1.3.2 Traumatic Spinal Cord Injury (secondary injury):

The term of secondary injury refers to the injury that occurs shortly after the initial injury and continues for weeks/months which leads to progressive damage of the spinal cord[6]. In fact, secondary injury is a complex phenomenon involving a cascade of cellular, molecular and biochemical events [14], [15] and is often associated with major clinical disabilities. This type of injury is divided into acute and sub-acute and chronic phases. The acute phase starts immediately after the injury. Cord inflammation, edema, necrotic cell death, excitotoxicity and calcium influx are phenomena occurring during the acute phase [16], [17]. Following the acute phase, comes the sub-acute phase of the injury. This phase involves apoptosis, Wallerian degeneration, demyelination of surviving axons and appearance of glial scar around the injury site. In the chronic phase of the injury the cystic cavities begin to form and glial scars start to mature [18]–[20]. The (figure 4) adapted from Anam Anjum (2020), summarizes the types of spinal cord injury and the pathophysiology of traumatic spinal cord injury.

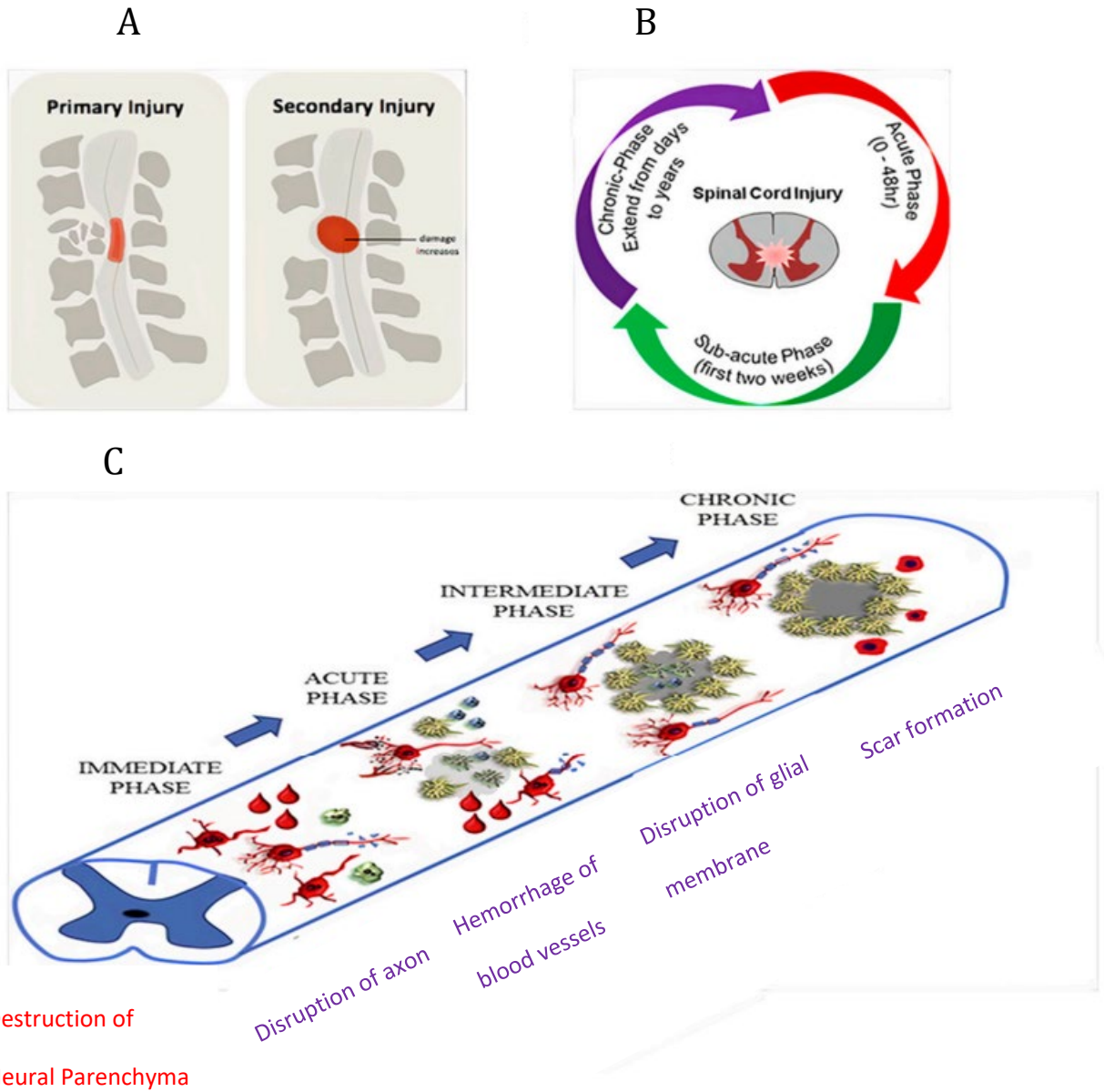


Figure 4: Spinal cord injury (SCI) (A) different phases of SCI, (B) schematic of the cycle of the secondary injury (C) pathophysiological events according to SCI phases, (adapted from Anam Anjum(2020)).

1.3.3 Clinical Classification System for Spinal Cord Injury:

To measure the severity of injury, functional classification of SCI has been developed, which provides a reproducible scoring system. The International Standards for Neurological Classification of Spinal Cord Injury (ISNCSCI) scoring system, developed by the American Spinal Injury Association (ASIA), determines the level and severity of SCI. The system can facilitate the measurement, comparison and correlation with the clinical grades [16]. As mentioned before the SCI can be classified as either complete or incomplete. Among all the other scoring systems, the ASIA system is the most accepted one for scoring SCI (figure 5). The accuracy and reproducibility of ASIA system in prediction of patients' outcome have made it a reliable clinical scoring system in SCI. The classification includes the assessments of motor, sensory and sacral functions. Majority of the other systems became obsolete due to some disadvantages in the evaluation method of these functions.

ASIA INTERNATIONAL STANDARDS FOR NEUROLOGICAL CLASSIFICATION OF SPINAL CORD INJURY (ISNCSCI) **ISICOS**

Patient Name _____ Date/Time of Exam _____
 Examiner Name _____ Signature _____

RIGHT

MOTOR KEY MUSCLES

UER (Upper Extremity Right)

C2
C3
C4
C5
C6
C7
C8
T1

LER (Lower Extremity Right)

L2
L3
L4
L5
S1

(VAC) Voluntary Anal Contraction (Yes/No)

RIGHT TOTALS (MAXIMUM)

UER + UEL = UEMS TOTAL (50) (25)
 LER + LEL = LEMS TOTAL (50) (25)

• Key Sensory Points

SENSORY KEY SENSORY POINTS

Light Touch (LTR) Pin Prick (PPR)

C2
C3
C4
C5
C6
C7
C8
T1
T2
T3
T4
T5
T6
T7
T8
T9
T10
T11
T12
L1
L2
L3
L4
L5
S1
S2
S3
S4-5

SENSORY SUBSCORES

LTR + LTL = LT TOTAL (56) (56)
 PPR + PPL = PP TOTAL (56) (56)

LEFT

MOTOR KEY MUSCLES

UEL (Upper Extremity Left)

C5 Elbow flexors
C6 Wrist extensors
C7 Elbow extensors
C8 Finger flexors
T1 Finger abductors (5th finger)

MOTOR (SCORING ON REVERSE SIDE)

0 = total paralysis
1 = palpable or visible contraction
2 = active movement, gravity eliminated
3 = active movement, against gravity
4 = active movement, against some resistance
5 = active movement, against full resistance
N = normal corrected for pain/tissue
NT = not testable

SENSORY (SCORING ON REVERSE SIDE)

0 = absent 2 = normal
1 = altered NT = not testable

LEL (Lower Extremity Left)

L2 Hip flexors
L3 Knee extensors
L4 Ankle dorsiflexors
L5 Long toe extensors
S1 Ankle plantar flexors

(DAP) Deep Anal Pressure (Yes/No)

LEFT TOTALS (MAXIMUM)

UEL + UEL = UEMS TOTAL (50) (25)
 LEL + LEL = LEMS TOTAL (50) (25)

NEUROLOGICAL LEVELS Steps 1-5 for classification as on reverse

1. SENSORY R L

2. MOTOR R L

3. NEUROLOGICAL LEVEL OF INJURY (NLI)

4. COMPLETE OR INCOMPLETE?
 Incomplete = Any sensory or motor function in S4-S5

5. ASIA IMPAIRMENT SCALE (AIS)

(In complete injuries only)
ZONE OF PARTIAL PRESERVATION
 Most caudal level with any innervation

SENSORY R L
 MOTOR R L

Figure 5: ASIA scoring for neurological classification of the SCI; a sample scoring sheet used for ASIA scoring in clinical setting. (adapted from: <http://asia-spinalinjury.org>)

The impairment score (AIS) ranges from (AIS A) referring to complete loss of sensation and movement to (AIS E) presenting a normal neurological function. It is important to first identify the neurological level of injury (NLI) in the SCI patients to be able to use the AIS scoring more accurately. If a patient is identified with the complete injury (AIS A), some segments below the NLI could maintain some sensory or motor function. In the case of complete loss of motor and preservation of some sensory functions the injury is classified as AIS B. If the motor function is also partially maintained in addition to the

sensory score (below the NLI) the AIS score is C or D [12].

As per clinical management of SCI, the neurological assessment decision is normally made within 72 hours after injury using ASIA scoring system[21] . It is shown that 72 hours time frame provides a more accurate assessment of neurological impairments after injury[22] . Patients with incomplete SCI, could gain some of the motor and sensory functions back. Most of the functional recovery occurs during the first 3 months and usually reaches a plateau 9 months post injury [12]. The adaptation and recovery process of the spinal cord functions after injury is known as neuronal plasticity [23]. The spinal cord reorganization and recovery process post injury can be better assessed by utilizing the quantitative and functional MRI techniques (i.e, DTI, NODDI, BOLD).

A comprehensive explanation of motor and sensory clinical assessment using ISNCSCI scoring system is in *appendix A*.

1.4 Physics of Magnetic Resonance Imaging (MRI)

Magnetic Resonance Imaging (MRI) is a non-invasive diagnostic imaging technique that is used to create multi-dimensional anatomical and physiological images of the body. MRI is based on the nuclear magnetic resonance (NMR) effect, which is the interaction between nuclei magnetic moments and a static magnetic field. In theory MRI, uses a strong magnetic field to produce images of the body's structures and organs. The technique is based on the fact that the human body is composed of water molecules, which contain hydrogen atoms. When a tissue is exposed to a magnetic field and an externally applied radio frequency (RF) pulses, a contrast is created between and within-tissue. In other words, the MRI scanner excites protons in water molecules of the human body using

a strong magnetic field and RF excitation, then measures their response to this excitation. In addition, MRI machines exploit spatially variant magnetic fields (magnetic field gradients) to encode the position of the measured signals. Unlike other imaging modalities (i.e. X-rays), MRI doesn't use ionizing radiation therefore it is a favorable tool to image the central nervous system (CNS) in the pediatric subjects.

An MRI protocol is normally designed in such a way that generates signals of a specific tissue and suppresses the undesired areas. The available mathematical models are able to measure the signals generated based on the tissue properties of the imaged structures (i.e. myelin content). These quantitative approaches are often referred to as quantitative MRI (qMRI). qMRI has the potential to provide novel and sensitive biomarkers capable of enhancing diagnosis and prognosis in a number of conditions.

The focus of this thesis is utilizing new qMRI techniques and biomarkers on the healthy pediatric spinal cord and children with spinal cord injury.

In this section, the basic concepts of magnetic properties of the nuclei are initially introduced. We then described the different MRI contrasts and sequences used in this study.

1.4.1 Spins and Magnetic Moments

Spin is a fundamental property of particles. Nuclei (with an even number of protons and neutrons) are characterized by certain physical properties such as an intrinsic *angular momentum* \mathbf{L} , or otherwise *spin*. The *angular momentum* creates a *magnetic moment* μ that interacts with the external magnetic fields. The following equation shows the relationship between the angular moment and the magnetic moment.

$$\mu = \gamma \mathbf{L} \tag{1.1}$$

where γ is the *gyromagnetic ratio*, its value depends on the nucleus in question.

In other words, protons are small magnetic dipoles that are also electronically charged.

The proton magnetic moment is the actual source of signals measured by MRI machines.

As the 70% of the human tissue is comprised of water, MRI imaging could be a helpful tool for clinical use.

1.4.2 Precession

If a magnetic dipole is placed in a magnetic field (B_0) it experiences a net torque equivalent to:

$$\tau = \mu \times B_0 \quad (1.2)$$

The torque induces a potential energy of $-\mu$ to the dipole. Any rotation caused by the torque will change the angular momentum in the direction perpendicular to both μ and B_0 . As mentioned in equation (1.1) the proton angular momentum (\mathbf{L}) is parallel to μ which leads to proton magnetic moment to precess with the rate of γB in the magnetic field (figure 6).

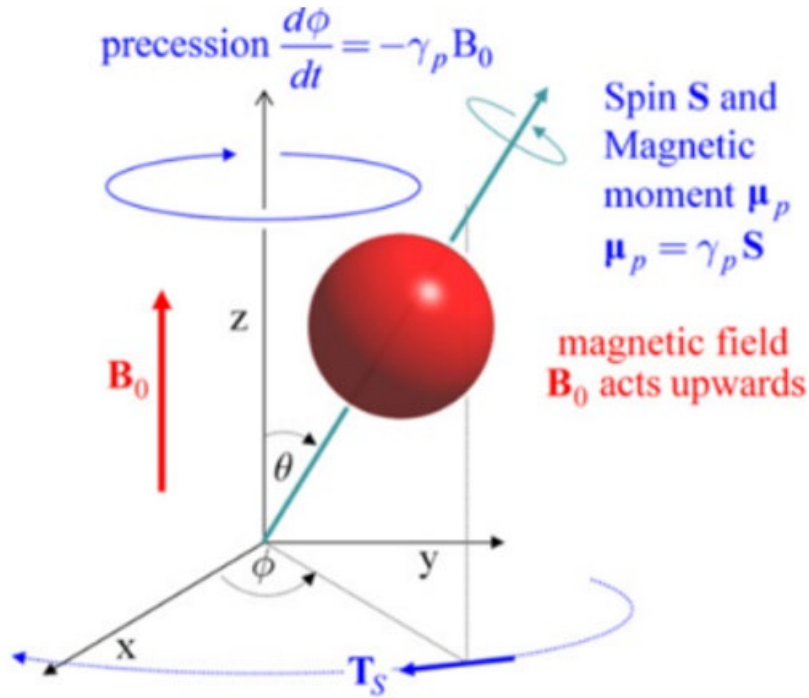


Figure 6: Illustration of precession of the proton in the magnetic field of (B_0) (adapted from R. Ansorge 2016).

Considering the temporal component of the angular momentum is written as

$\frac{dL(t)}{dt} = \tau(t)$, from equation (1.1), $L(t) = \frac{\mu(t)}{\gamma}$, and substituting the expression of $\tau(t)$ from equation (1.2), the partial differential equation describing the spin dynamics induced by an external magnetic field of B_0 is shown as:

$$\frac{d\mu(t)}{dt} = \gamma\mu(t) \times B_0(t) \quad (1.3)$$

Equation (1.3) states that under a magnetic field of $B_0(t)$ the magnetic moment $\mu(t)$, rotates with an angular velocity of $\omega(t) = -\gamma B_0(t)$ proportional to the $B_0(t)$ at any given time of t . This phenomenon is called *Larmor precession* and the frequency of $\omega(t)$ is called *Larmor frequency*.

1.4.3 The Bloch Equations and T1-weighted, T2-weighted MRI

Considering the magnetic moment of μ for a single spin, we can define the net magnetization of the spins in a volume as \mathbf{M} . At equilibrium, the net magnetization vector is aligned with the applied magnetic field \mathbf{B}_0 and is called the equilibrium magnetization \mathbf{M}_0 . If the vector \mathbf{M} is perturbed so it requires a component of \mathbf{M}_\perp perpendicular to \mathbf{B}_0 . \mathbf{M}_\perp will precess around \mathbf{B}_0 and produces a signal. The time evolution of \mathbf{M} is shown with an ordinary differential equation called *Bloch equations*[24]. The *Bloch equation* models the Larmor precession of \mathbf{M} about a static field, and describes the return of \mathbf{M} to its equilibrium state called *Relaxation*. The precession equation is as follows:

$$\frac{d\mathbf{M}}{dt} = \gamma \mathbf{M} \times \mathbf{B}_0 \quad (1.4)$$

After protons are excited in a magnetic field, it takes time for the proton spins to reach equilibrium. The spins reach equilibrium in an exponential manner. The time constant here is expressed by T_1 , therefore:

$$\frac{dM_{\parallel}}{dt} = \frac{(M_0 - M_{\parallel})}{T_1} \Rightarrow M_{\parallel}(t) = M_0 \left(1 - e^{-\frac{t}{T_1}}\right) \quad (1.5)$$

In this equation (1.5), M_{\parallel} is a component of the magnetization vector that is parallel to \mathbf{B}_0 and has the equilibrium value of M_0 . Since the M_{\parallel} is parallel to \mathbf{B}_0 it doesn't precess. As explained before, if the M_{\parallel} is perturbed from being parallel to \mathbf{B}_0 it results in a net component \mathbf{M}_\perp in transverse (x-y) plane. The \mathbf{M}_\perp will start decaying exponentially with the time constant of T_2 which yields the *Bloch equation* [24]:

$$\frac{d\mathbf{M}}{dt} = \gamma \mathbf{M}_\perp \times \mathbf{B}_0 - \mathbf{M}_\perp / T_2 - (M_{\parallel} - M_0) / T_1 \quad (1.6a)$$

or

$$\frac{dM_{\parallel}}{dt} = -\frac{M_{\parallel} - M_0}{T_1} \quad \text{and} \quad \frac{dM_{\perp}}{dt} = -\frac{M_{\perp}}{T_2} \quad (1.6b)$$

Where T_1 and T_2 are fundamentals of MRI imaging (figure 7).

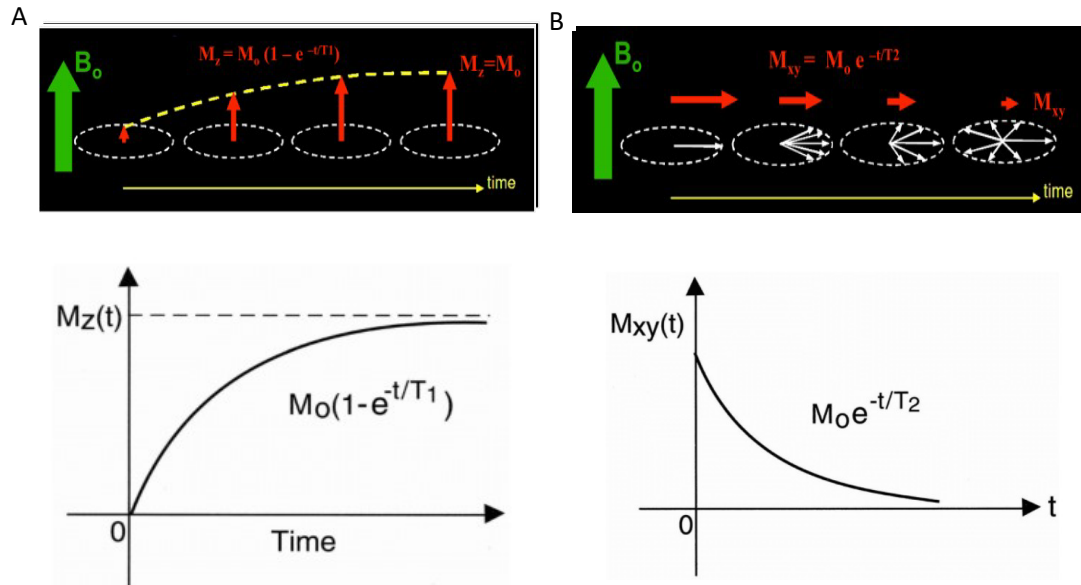


Figure 7: Illustration of A) The graph of recovery of longitudinal magnetization with the growth rate of T_1 , B) The graph of transverse magnetization with the decay rate of T_2 and RF off (figures are adapted from <https://mriquestions.com/>).

Both T_1 and T_2 provide information about the structure and composition of tissues being scanned. T_1 , refers to the longitudinal relaxation time, which is the time it takes for the protons to realign with the magnetic field after RF excitation. In T_1 -weighted MRI imaging, a short TR (repetition time) is used to minimize the recovery of longitudinal magnetization between excitations, resulting in a relatively high signal from tissues with short T_1 relaxation times, such as fat. Whereas, T_2 , refers to the transverse relaxation time, which is the time it takes for the transverse magnetization of protons to decay after

excitation. In T2-weighted MRI imaging, a long TE (echo time) is used to allow the transverse magnetization of protons to decay naturally, resulting in a relatively high signal from tissues with long T2 relaxation times, such as water.

1.4.4 MRI Pulse Sequences:

In each pulse sequence, the timing of an RF pulse and gradient pulse could be adjusted. Two important parameters of each sequence are TR and TE.

TR, is the time between successive RF pulses. It determines the overall length of the imaging sequence and the amount of time allowed for the recovery of the longitudinal magnetization of the protons in the tissue. TE, is the time between the initial RF pulse and the detection of the resulting signal. When pulse programming, SE (spin echo) sequence, is used to produce T1-weighted and T2-weighted images. Another important and commonly used sequence is GRE (gradient echo). T1-weighted and T2-weighted GRE sequences are pulse sequences that use gradient magnetic fields and RF pulses to create images with T1-weighted or T2-weighted contrast. In contrast to SE sequences, which use two RF pulses to create a spin echo signal, GRE sequences use a single RF pulse and a gradient magnetic field to create a gradient echo signal (figure 8). As shown in (figure 8a) the diagram's top line illustrates the RF pulses. Starting with a 90-degree RF pulse followed by a 180-degree RF pulse applied TE/2 later. The second line shows the timing of the slice-select gradient (z Gradient), which is activated positively while the RF pulses are sent to target only one slice of tissue. The slice-select gradient is intermittently reversed to reduce dephasing of transverse magnetization. The third line demonstrates the timing of the frequency-encoding or "readout" gradient (x Gradient), which separates signals in the second in-plane direction perpendicular to both the slice-select and frequency-encoding

directions during signal measurement. The fourth line displays the phase-encoding (y Gradient) gradient's timing, which is applied orthogonally to the slice-select gradient (z Gradient) along one of the two in-plane directions. For each repetition of the pulse sequence, the strength and duration of the phase-encoding gradient are different to provide varying degrees of phase encoding. Lastly, the bottom line shows the signal from the selected slice, with the highest echo signal appearing TE amount of time after the initial 90-degree pulse.

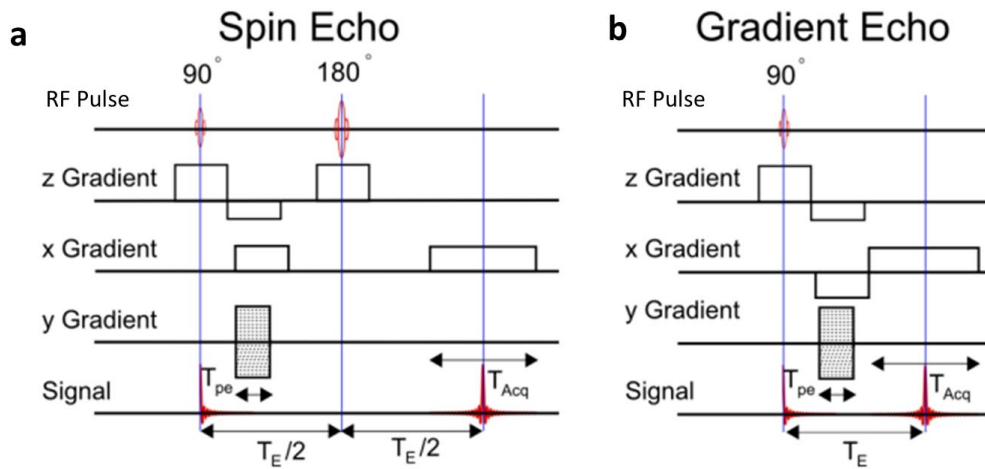


Figure 8: Illustration of a) spin echo sequence b) gradient echo sequence (adapted from Karl T. Edler, 2010)

In (figure 8b), a schematic of GRE sequence is shown. Each line of the diagram has a similar explanation (figure 8a). A 90-degree RF pulse is applied (this Rf pulse could be $\leq 90^\circ$). The 180-degree pulse is substituted with the reversal of the frequency-encoding gradients (x Gradient) at TE/2. The signal echo still takes place at the TE. With this approach, there's no need to wait for the longitudinal magnetization to regrow [25].

1.4.5 Principles of Diffusion MRI

Diffusion MRI (dMRI) is a non-invasive imaging method that relies on the physical principles of diffusion NMR to assess water diffusion within a given spatial area in in-vivo tissue. In theory, dMRI measures the movements of water molecules, which can describe the structure of the underlying tissue microstructure. Water molecules in tissues move randomly in all directions and this movement is known as Brownian motion [26]. The flux of water molecules in each direction is explained by Fick's first law ([27]) and can be written as follows:

$$J = -D \nabla C \quad (1.7)$$

where J is the mass flux (units: mass/time), D is the diffusion coefficient (units: area/time) and C is the concentration of water molecules (units: mass/volume). The estimated value of the diffusion coefficient is generally referred to as the “apparent diffusion coefficient (ADC)” [28], and it depends on the orientation of the tissue fibers.

If the water molecules are in a non-restricted environment (i.e. glass of water), they can diffuse isotropically in any direction and the root-mean-square displacement of this motion over a time interval of T_d is:

$$r = \sqrt{6DT_d} \quad (1.8)$$

On the other hand, considering confined structures (i.e. fibrous tissues such as white matter), the movements of water molecules will be restricted, and they tend to diffuse along the fibers. In other words, structures like white matter are compartmentalized structures that restrict the diffusion of water molecules. This type of diffusion is characterized by anisotropic diffusion (figure 9). Based on this property of water diffusion

in WM, some structural and geometric characteristics of WM can be extracted.

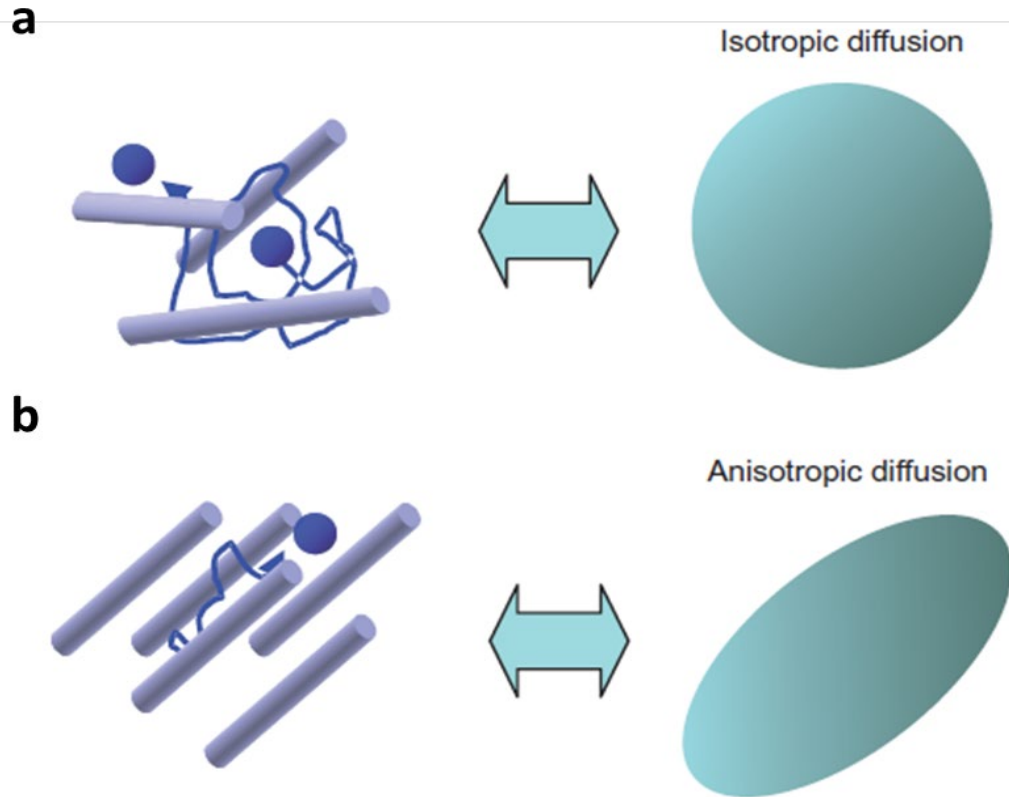


Figure 9: Illustration of water molecules movement in different environments a) Isotropic diffusion b) Anisotropic diffusion (adapted from Mori and Tournier 2014) [29])

There are several reconstruction models proposed for diffusion MRI (i.e. diffusion tensor imaging (DTI), neurite orientation dispersion and density imaging (NODDI), Q-Ball imaging (QBI)). The most popular one is diffusion tensor imaging (DTI) [30]. Here we will review DTI model as we have used it in our work. Using DTI, both equations (1.7) and (1.8) could be generalized and the scalar diffusion coefficient can be written as

$$D = \begin{pmatrix} D_{xx} & D_{xy} & D_{xz} \\ D_{xy} & D_{yy} & D_{yz} \\ D_{xz} & D_{yz} & D_{zz} \end{pmatrix} \quad (1.9)$$

D is referred to as Diffusion Tensor and represent the matrix of spins displacements.

In order to quantify diffusion, an MRI sequence is required, which includes two diffusion-encoding gradients symmetrically placed around the 180-degree RF pulse. [31] (figure 10). The figure shows a schematic of dMRI sequence. ‘B’ represents the static magnetic field which is uniform before applying the ‘g’ gradient. After the first gradient is applied (right before the 180-degree pulse), the signal loses its uniform phase (‘Dephasing’ process begins: protons begin to precess at different rates of ω . The color encoding shows the amount of this precession rate). After the second ‘g’ is applied, the ‘Rephasing’ process begins, and the uniform phase is restored. ‘M’ is a vector component representing the sum of the magnetic spin moments.

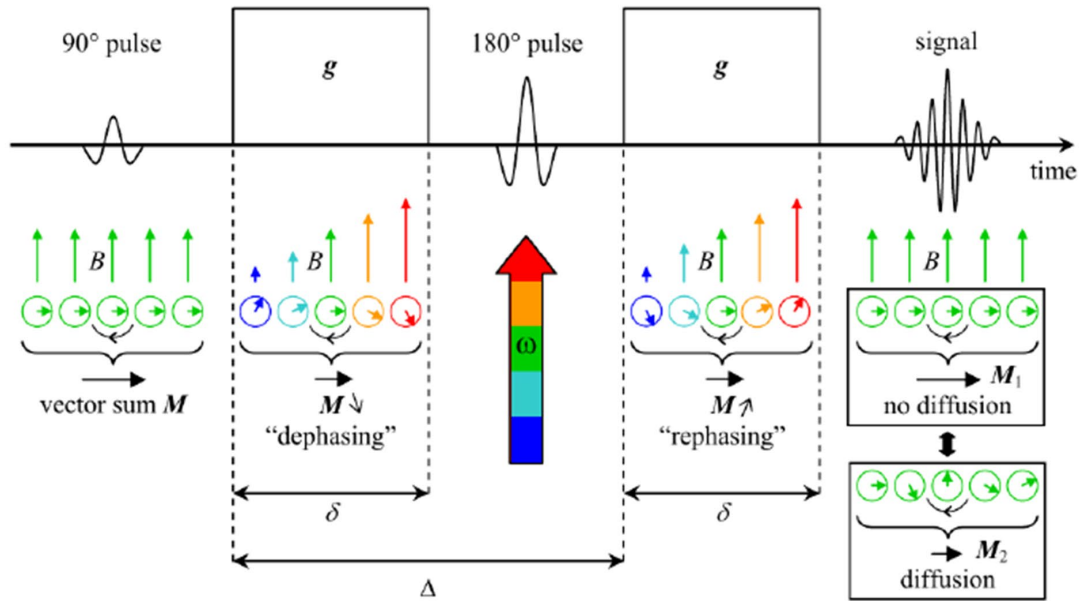


Figure 10: A schematic of the dMRI sequence. ‘B’ represents the static magnetic

field, 'M' is a vector component representing the sum of the magnetic spin moments, 'g' is the diffusion encoding gradients. Image adapted from Snoussi_Haykel PhD report.

1.4.6 Diffusion Tensor imaging (DTI)

One of the techniques that enable the measurement of the directional diffusivity of water is DTI. MRI images can be acquired with applying diffusion-weighting in each of several directions. For simple isotropic Gaussian diffusion, the signal attenuation for the diffusion gradient pulses is measured with *so-called* Stejskal-Tanner equation as follows:

$$s/s_0 = e^{-bD} \quad (1.10)$$

where S is the diffusion-weighted (DW) signal, S_0 is the signal without any DW gradients, D (mm²/s) is the apparent diffusion tensor, and b (s/mm²) is the diffusion-weighting (b-values characterize the degree of diffusion sensitivity). Using the Stejskal-Tanner equation, the diffusion tensor of D can be estimated. As described before, D contains 6 elements. Meaning that 6 scans (in 6 directions) are required for a simple diffusion acquisition to measure the displacement of the water molecules.

Considering the shape of the molecular diffusion is represented with an ellipsoid, the diffusion tensor matrix of D can be decomposed into its components as eigenvalues and eigenvectors. In DTI, the eigenvalues and eigenvectors of the diffusion tensor describe the direction and strength of diffusion in the tissue. The eigenvalues are the three values that result from the diagonalization of the diffusion tensor, and they represent the magnitude of diffusion along each of the three main axes of the tissue. The eigenvectors are the corresponding vectors that describe the direction of the diffusion along each of the

principal axes. Therefore, if the diffusion tensor matrix of D is represented with its components, we will have the following:

$$D = E \cdot \Lambda \cdot E^{-1} \quad (1.11)$$

Where E (eigenvectors) and Λ (eigenvalues) are as follows

$$E = (e_1, e_2, e_3) \text{ and } \Lambda = \begin{pmatrix} \lambda_1 & 0 & 0 \\ 0 & \lambda_2 & 0 \\ 0 & 0 & \lambda_3 \end{pmatrix}$$

(figure 11) illustrates the eigenvector and eigenvalues in a diffusion tensor field.

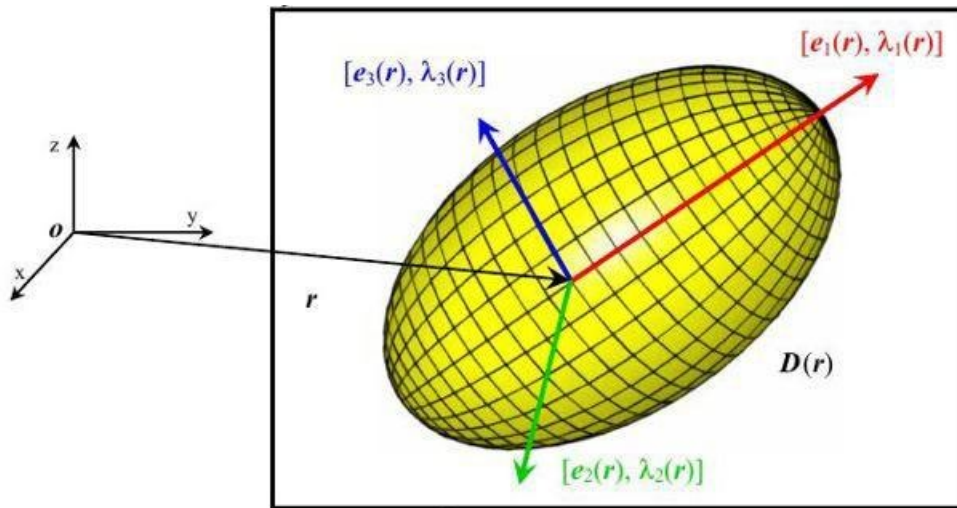


Figure 11: Ellipsoidal representation of the diffusion tensor field. Note that every voxel corresponding to position r of a dMRI scan, is described by the eigenvectors $e(r)$ and eigenvalues $\lambda(r)$ of the diffusion tensor $D(r)$. Image source: A. Leemans's PhD report.

In DTI, eigenvalues and eigenvectors are used to compute a variety of measures that are used in DTI analysis. These are *so-called* DTI metrics and are comprised of fractional

anisotropy (FA), mean diffusivity (MD), axial diffusivity (AD) and radial diffusivity (RD). These measures can provide information about the microstructure of the tissue, such as the presence of white matter tracts or the degree of tissue damage in neurodegenerative diseases.

FA is generally used to measure the amount of diffusion anisotropy. Therefore, it is expected that FA values obtained from WM tracts are higher when compared to that of GM or cerebrospinal fluid (CSF). Unlike FA, MD values are higher in CSF as opposed to WM structure. This is because of the fact that MD measures the average displacement of water molecules. The next following equations describe the mathematical presentation of the DTI metrics using eigenvalues.

$$MD = \frac{\lambda_1 + \lambda_2 + \lambda_3}{3} = \bar{\lambda} \quad (1.12)$$

where $\bar{\lambda}$ is the average all the eigenvalues.

$$FA = \sqrt{3/2} \frac{\sqrt{(\lambda_1 - \bar{\lambda})^2 + (\lambda_2 - \bar{\lambda})^2 + (\lambda_3 - \bar{\lambda})^2}}{\sqrt{\lambda_1^2 + \lambda_2^2 + \lambda_3^2}} \quad (1.13)$$

AD, is a representative of diffusion along the λ_1 . Considering the WM structure, AD represents the diffusion of water molecules along the axis of the axons.

$$AD = \lambda_1 \quad (1.14)$$

Despite AD, RD represents the rate of water diffusion perpendicular to the axons of white matter tracts. In other words, RD represents the diffusion of water molecules across the axons.

$$RD = \frac{\lambda_2 + \lambda_3}{2} \quad (1.15)$$

The DTI model is used increasingly in studying the spinal cord and its associated disease.

The focus of these studies is to show the sensitivity of the DTI metrics to detect spinal cord pathologies and diffusion changes at the microstructural level. The majority of these studies are targeting adult population. Here we investigated the diffusion changes in the pediatric spinal cord in healthy and spinal cord injury populations. We will explain this in the next chapter of this manuscript.

CHAPTER 2

STATE OF THE ART

2.1 Spinal Cord Quantitative MRI (qMRI)

In the last few decades, there has been a growing number of studies addressing the potential of qMRI in the diagnosis and prognosis of spinal cord complications such as multiple sclerosis (MS) [32], spinal cord injury (SCI) [15], [33], [34] or amyotrophic lateral sclerosis (ALS) [35]. Contrary to the brain, studying spinal cord anatomy and its complications is challenging. This is mainly because of the small size of the cord and its specific anatomical arrangement, exacerbating its imaging [36], hence, warranting the need for high-resolution scans to discern the cord structures (i.e. GM, WM). Other challenges associated with imaging the cord are related to physiological artifacts (i.e. heartbeat, breathing,...), which add distortions to the images [37], [38]. Other than physiological artifacts, other types of distortions induced during MRI spinal cord acquisitions arise from magnetic susceptibility between the spinal cord and the surrounding tissue. One way to alleviate the consequences of these artifacts is to use cardiac gating or pulse oximetry during the acquisitions [39]. Both methods allow the acquisition of images based on the heart cycle of each individual (the period of the cardiac cycle happens where the flow effects are minimal)[39].

Despite the aforementioned challenges in imaging the spinal cord, most diffusion MRI studies use DTI to quantify the diffusion changes in the spinal cord [40]. In recent years, DTI has shown promise as a noninvasive imaging biomarker for evaluating tissue microstructure [41]. The highly directional structure of the spinal cord enables DTI to localize WM accurately, separate WM from GM, and assess structural damage of the cord

by modeling the direction and magnitude of water diffusion [42]. Therefore, it's safe to consider DTI as a biomarker that is sensitive to the integrity of the cord and specifically WM. Numerous spinal cord studies used DTI to assess the WM microstructure in the adult population [43], [44]. However, pediatric spinal cord studies have been rare [45], [46]. This emphasizes the importance of studying children's spinal cord anatomy at the microstructural level, which also enables obtaining and establishing diffusion normative values for various WM tracts. Hence, one of the objectives of this thesis is to establish normative DTI values of the several WM tracts found in the pediatric spinal cord in typically developing (TD) population and use those values as a potential imaging biomarker to discriminate between TD pediatric cord and spinal cord injury (SCI) patients. As an example, the corticospinal tract (CST), one of the descending tracts of the lateral motor system, is among the most studied WM tracts [47]. Therefore, it's crucial to probe the disparity between dorsal column sensory tracts and lateral corticospinal tracts, specifically in the pediatric cohort. Some studies [48], [49] have shown the usefulness of normative DTI-derived values, presenting a good correlation with the values acquired from clinical examination of motor and sensory levels in SCI patients. Few other works in pediatric patients have demonstrated DTI indices differences between age and cord region [45], [46] using manual region of interest (ROI) extraction. However, no studies, to date, to our knowledge, have analyzed the WM tract diffusion changes in the pediatric cervical spine using automated tract delineation as suggested in our work. Despite the feasibility of pediatric spinal cord DTI acquisitions with recent scanning improvements, there are still efforts required to be made toward the development of publicly available processing tools and imaging references targeting spinal cord MRI data. For instance, the lack of a common

template makes it difficult to process multi-parametric data within a standard framework. A common template of the spinal cord can facilitate the development of biomarkers sensitive to white matter damage and neuronal function. A template would also provide the researchers with a tool to process qMRI data and to compare results between groups and subjects.

2.2 Spinal cord MRI template and atlases

The existing brain templates (i.e MNI template) have helped researchers for years by allowing sharing, comparing, and validation of their findings between groups. However, such templates are rare in the spinal cord and non-existent in the pediatric population. Earlier works of several research groups have specified the spinal cord templates based on their unique applications. In 2008 *Stroman* group [50] used fMRI data from 24 experiments in eight volunteers that were normalized and combined to create the first anatomical (T2-w) reference volume (figure 12). This template was then extended to 10 subjects and was further modified to improve the representation of the spinal levels.

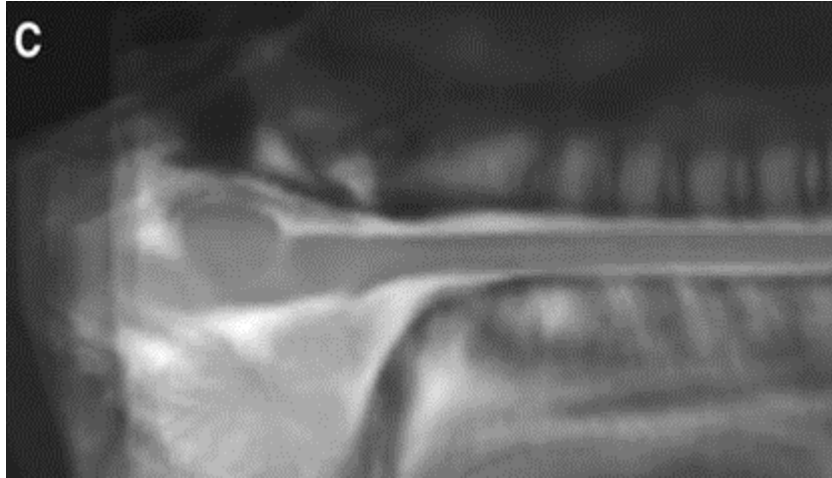


Figure 12: shows the midline slice averaged over 24 experiments in eight volunteers. (adapted from P. Stroman et al., Magnetic resonance imaging 26.6 (2008))

Later in 2009, *Eippert et al.* made a T1-w template of the cervical spinal cord [51]. The template was created out of 15 images with the limitation of arbitrarily selecting one subject that served as a target for registering all the other subjects (figure 13).



Figure 13: The average structural image. The black box indicates the sagittal section, and the red line indicates the transverse line. (adapted from F. Eippert et al., Science (2009))

Valsasina et al. [52] generated a T1-w template of the cervical spinal cord for use in spinal cord atrophy. This was done by proposing a normalization procedure based on a semi-automated segmentation approach. The template averages 90 images of healthy subjects to create a straight template of the spinal cord (figure 14).

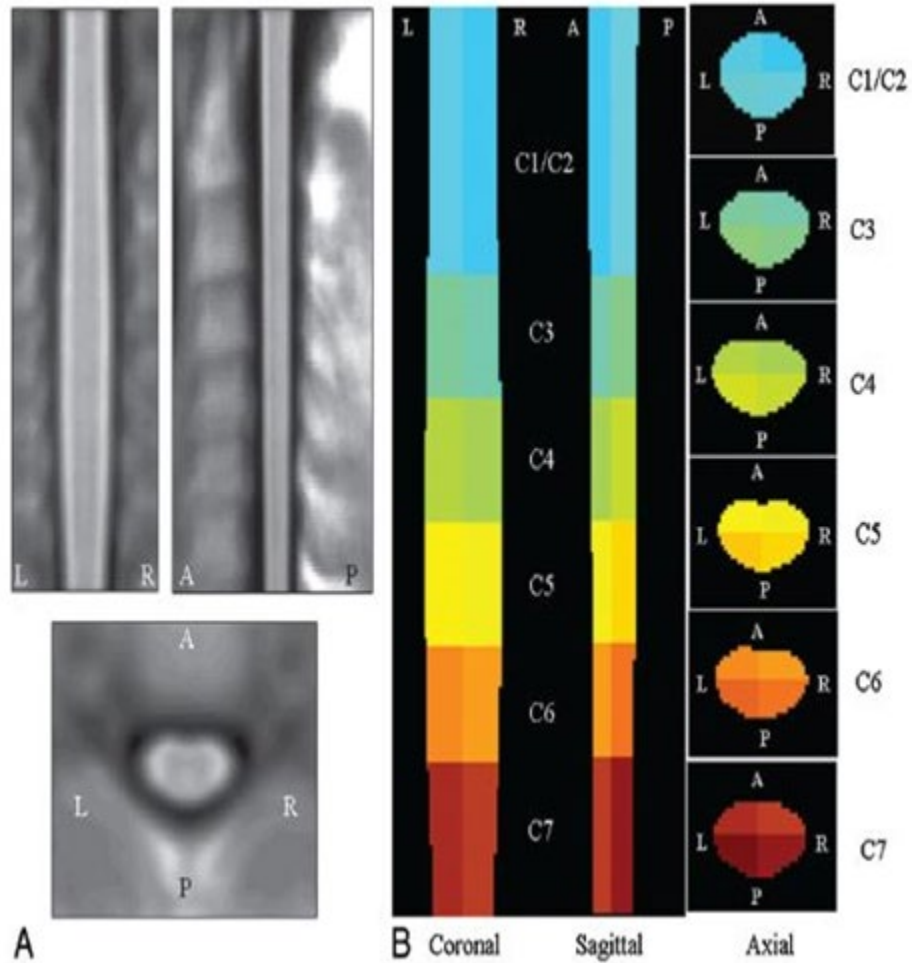


Figure 14: The picture shows: **A**, Coronal, sagittal, and axial views of the cervical cord template created as the average of all the healthy subjects in the study. **B**, Coronal, sagittal, and axial sections of the corresponding color-coded normalized region-label mask reporting the 24 reference anatomic regions (anterior, posterior, left, and right sections of C1/C2, C3, C4, C5, C6, and C7) . (the figure and the paragraph adapted from P. Valsasina ., et al, American Journal of Neuroradiology (2012))

After Valsasina group, *El Mendili et al.* [53] introduced a template of the cervical spinal cord, based on a similar approach to *Valsasina*. The difference between the two templates was using different normalization methods (figure 15).

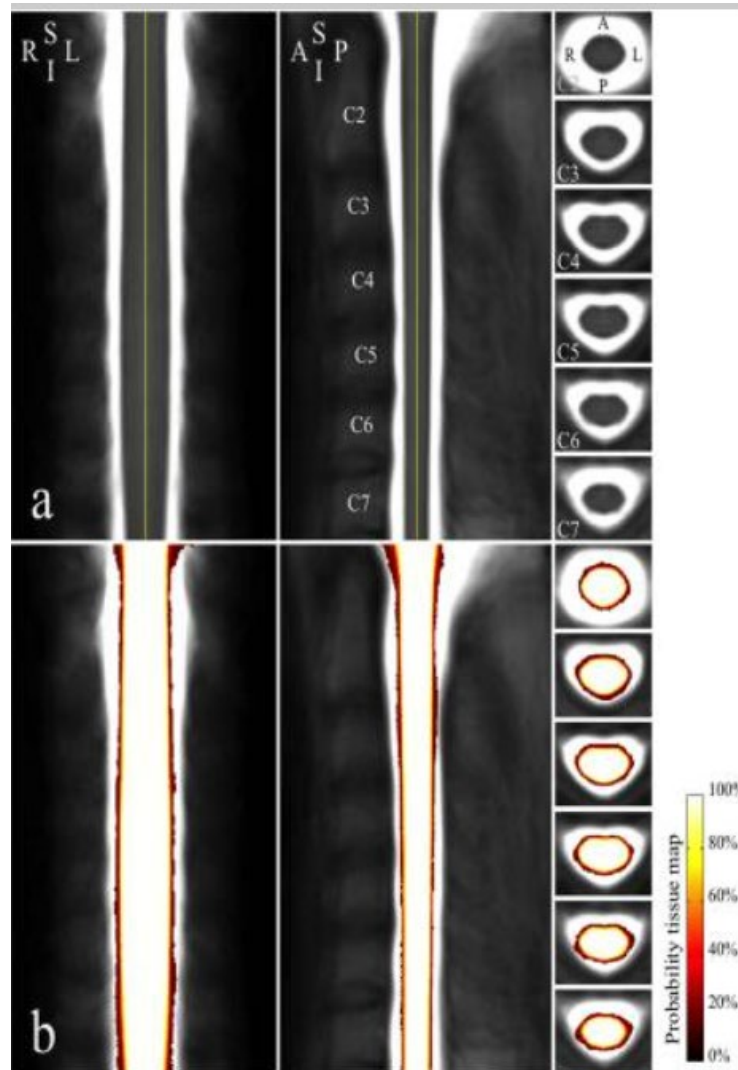


Figure 15: The image illustrates the cervical spinal cord template along with the probability tissue map. **(a)** a coronal view is presented on the top left section, the middle image represents a sagittal view and the top right figure is presenting axial view of the cervical cord at different levels (from C2- C7). **(b)** the bottom row shows the probability tissue maps. The probability map shows the voxel value from

0 to 1. With 0 representing a voxel outside of the spinal cord and 1 being a voxel that belongs to the spinal cord.

* (A, anterior; I, inferior, L, left, P, posterior, R, right; S, superior)

figure and the paragraph adapted from *M. El Mendili et al., (2015)*

AMU40 template was generated with *Taso* group in 2015 [54]. It was the first template to enclose probabilistic white and gray matter atlases. This template was used to study the morphometry mapping of the adult population based on age (figure 16). For example, the group was able to show anterior gray matter atrophy in elderly volunteers when compared to a young population. AMU40 is a T2*-w template of the cervical spinal cord from 40 healthy subjects.

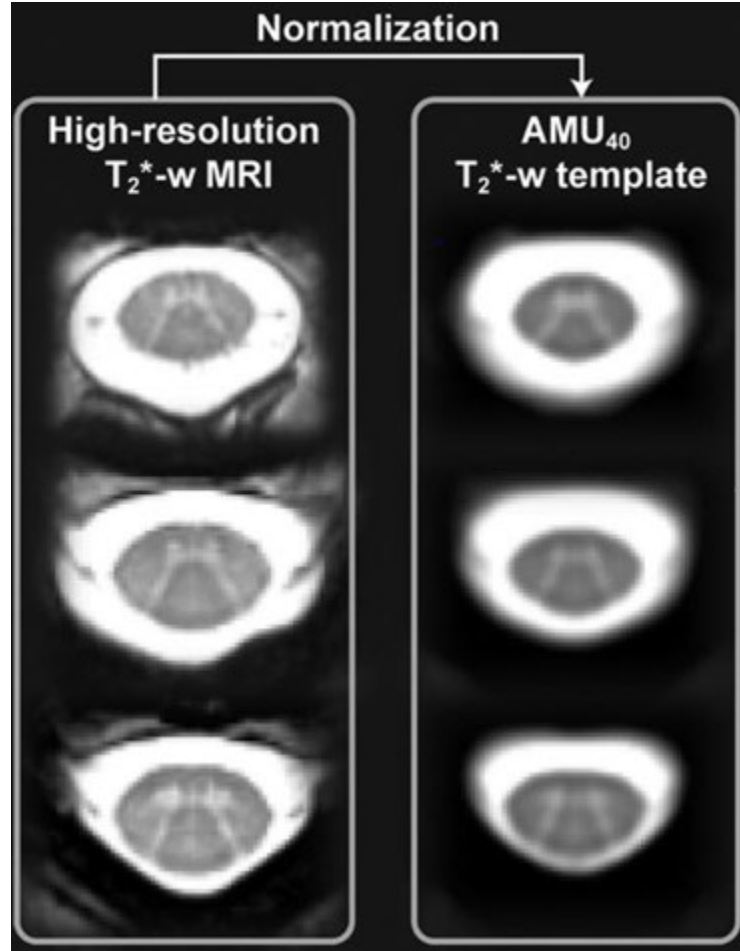


Figure 16: Illustrates the AMU40 template. The template represents the T2*-weighted template of the cervical spinal cord from 40 healthy subjects (AMU40). (Image adapted from M. Taso et al., Neuroimage (2015)).

In 2014, Fonov's et al., [55] generated the MNI-Poly-AMU, an unbiased template of T2-w scans from 16 healthy adult subjects (figure 17). The template covers from C1 up to T6 vertebral level, along with probabilistic atlases of the white and gray matter. The template was then integrated into Spinal Cord Toolbox (SCT) [56]. The SCT is a comprehensive and open-source software for analyzing multiparametric MRI data of the spinal cord. One

of the limitations of this template is that it only covers C1 to T6 levels and is only available in T2 contrast.



Figure 17: Illustrates MNI-Poly-AMU, T2-weighted template with vertebral labeling. First three panels from left, represent coronal, sagittal and labeled sagittal view of the spinal cord covering C1 to T6 levels. Panel on the right shows axial views of vertebral levels, with an overlay of the spinal cord and CSF contours. Figure and the paragraph are adapted from (V.S. Fonov et al., Neuroimage (2014)) * (A, anterior; I, inferior, L, left, P, posterior, R, right; S, superior)

Finally and very recently (2017), *De Leener et al*, introduced, to date, the most comprehensive template of adult's population called PAM50 [57] which addresses the aforementioned limitations in the existing templates. PAM50 covers the entire spinal cord and is available in T1-w and T2-w contrasts (figure 18). The template is also compatible with existing brain templates enabling the study of brain and spinal cord association. Despite these past investigations on spinal cord templates, no group has proposed the generation of a pediatric spinal cord template which is one of the main objectives of this thesis work.

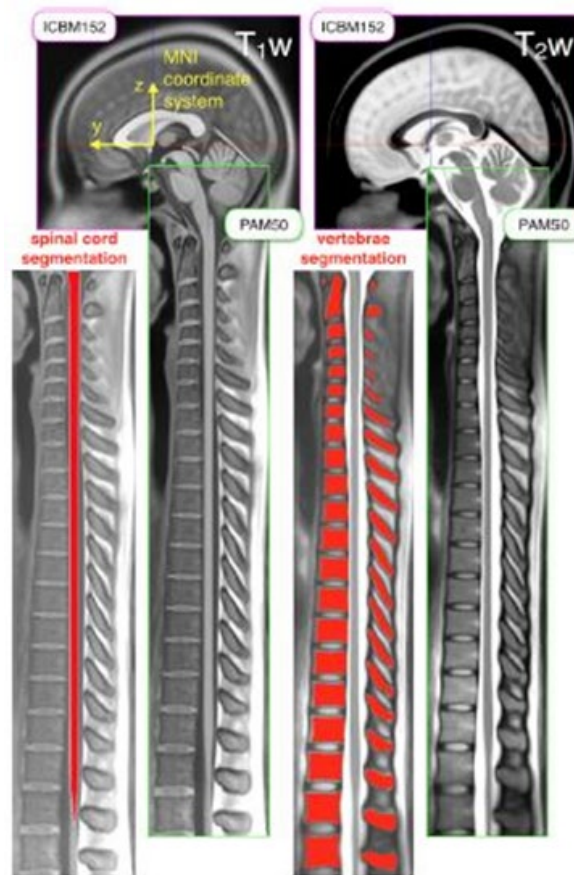


Figure 18: T1-w and T2-w sagittal views of the PAM 50 template, which covers the brainstem and the full spinal cord along with segmentation of the spinal cord and vertebrae. The PAM50 template is registered with the

ICBM152 “MNI” brain template at the level of the brainstem. Figure and the paragraph are adapted from (B. DeLeener et al., Neuroimage (2018))

In this work, we have focused on developing, to our knowledge, the first standardized spinal cord template of TD pediatric subjects as well as applying multiparametric MRI data in measuring and quantifying the microstructural and macrostructural changes in TD pediatric spinal cord and children with SCI. The next few chapters will explain the efforts made in this study to achieve the result.

CHAPTER 3

METHODOLOGY

Based on the previous chapters from the introduction to literature review, we can summarize the following statements regarding the methods in qMRI data of the pediatric spinal cord:

- The standardized normative template will facilitate group and single-subject analysis in a standardized 3D space, thereby controlling for the variability among the subjects. In addition, template base analysis of the cord allows for reproducible and comparable analysis of the large group of patients providing enhanced diagnostic tools for spinal cord disease.
- There are not many (adult) templates of the spinal cord in the literature that covers the full spinal cord, and to our knowledge, no such template for the pediatric spinal cord exists.
- Normative references are a mainstay of pediatric practice and facilitate the interpretation of values and clinical decision-making about treatment and treatment effectiveness. This will also increase the specificity and sensitivity of these noninvasive biomarkers for detecting lesions in children with SCI. In addition, these imaging biomarkers and the template could be extended to other pediatric spinal cord diseases in the future.
- The DTI metrics of FA, MD, RD, and AD values obtained from TD subjects could establish the normative range of diffusion metrics at defined vertebral levels. These values can be used as a potential imaging biomarker to discriminate between TD pediatric cord and SCI patients.

According to the above summary, the research question posed is, “ *how to create MRI pediatric template of the spinal cord that would allow the template-based analysis of the*

pediatric spinal cord as well as providing normative references that could be used as imaging biomarkers to facilitate clinical decision making in children with SCP”.

Therefore, the *main objectives* of this PhD thesis are as follows:

Specific Aim 1: Develop a standardized pediatric spinal cord template using a high resolution T2-w scan of 30 typically developed subjects with an age range of 6-17 years old.

Aim 1.1: Establish normative values of spinal cord cross sectional area (SCCSA) measurement using the isotropic T2-w scan in 30 typically developed subjects between 6-17 years.

Specific Aim 2: Establish the atlas-based normative values of the diffusion tensor imaging (DTI) indices for various white matter tracts in 30 typically developing subjects (age range 6-16 years old) at the C3 level of the cervical cord.

Aim 2.1 : Compare the obtained DTI metrics (as well as other qMRI metrics) from TD subjects to that of SCI patients. More specifically, to examine sites cephalad and caudal to a lesion and compare those values with values of the TD population.

3.1 Structure of the dissertation

As illustrated in (figure 19), chapter 4 explains the efforts made as part of this thesis work towards creating the T2-w pediatric template of 30 TD subjects (specific aim 1). It also explains one of the main utilization of the created template in measuring and establishing normative SCCSA values for selected levels of the cord (specific aim 1, aim 1.1). This work has been presented in the American Society of Neuroradiology (ASNR) 57th Annual Meeting in Boston, USA, 2019 as an oral presentation, which won the Derek Harwood Nash award of 2019 at this conference (2019 ASPNR DEREK HARWOOD-NASH

AWARD). This award is granted for the most outstanding pediatric neuroradiology paper at the ASNR annual meetings. This work was published in the proceeding of the International Society of Magnetic Resonance in 2019, as well. [58]

Chapter 5, presents the work concerned with obtaining the normative values of DTI metrics in TD subjects (specific aim 2). This work was published in the American Journal of Neuroradiology (AJNR) in 2021, titled as “Atlas-Based Quantification of DTI Measures in a Typically Developing Pediatric Spinal Cord” [59]. In this work, we developed a processing pipeline for the atlas-based generation of the TD pediatric spinal cord WM tracts that help with establishing the normative diffusion values. The age-related changes in these normative DTI metrics were also investigated.

Chapter 6, extends the result of the previous article from chapter 5 by translating the clinical applications of our findings in children with SCI (specific aim 2, aim 2-1). This study is submitted to the Journal of Neurotrauma in 2023 as an original research article titled as “Quantitative Magnetic Resonance Imaging to Characterize the Macro and Microstructural Changes in Typically Developing Pediatric Subjects and Patients with Spinal Cord Injury”. The purpose was to measure macrostructural and microstructural neurodegenerative changes remote from a spinal cord injury lesion in children with SCI and compare them with TD children using qMRI measures. We hypothesized that the observed changes in those regions of the cord can provide insights into the full extent of the injury.

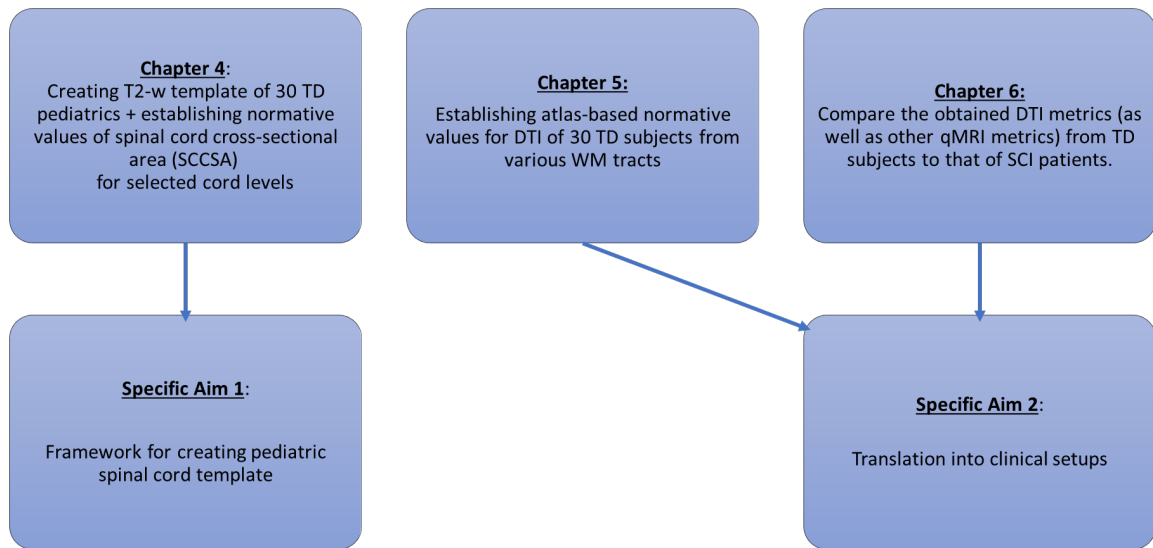


Figure 19: Illustration of the structure of this thesis based on the chapters and the related specific aims of this thesis work.

3.2 Additional publications

The present dissertation introduces two original articles that have been published/submitted during my Ph.D. work. Several other related articles and conference proceedings were also published during this timeframe and are listed below:

3.2.1 Peer-review journals

- 1) C. Blanc, **S. Shahrampour**, F. B. Mohamed, and B. de Leener, “Combining PropSeg and a convolutional neural network for automatic spinal cord segmentation in pediatric populations and patients with spinal cord injury,” *Int. J. Imaging Syst. Technol.*, vol. n/a, no. n/a, Feb. 2023, doi: 10.1002/ima.22859. [60]
- 2) Middleton DM, **Shahrampour S**, Krisa L, Liu W, Nair G, Jacobson S, Conklin CJ, Alizadeh M, Faro SH, Mulcahey MJ, Mohamed FB. Correlations of diffusion tensor imaging and clinical measures with spinal cord cross-sectional area measurements in pediatric spinal cord injury patients. *J Spinal Cord Med.* 2021 Dec 2:1-8. doi: 10.1080/10790268.2021.1997027. Epub ahead of print. PMID: 34855576.[61]

- 3) Saksena S, Mohamed FB, Middleton DM, Krisa L, Alizadeh M, **Shahrampour S**, Conklin CJ, Flanders A, Finsterbusch J, Mulcahey MJ, Faro SH. Diffusion Tensor Imaging Assessment of Regional White Matter Changes in the Cervical and Thoracic Spinal Cord in Pediatric Subjects. *J Neurotrauma*. 2019 Mar 19;36(6):853-861. doi: 10.1089/neu.2018.5826. Epub 2018 Oct 3. PMID: 30113265; PMCID: PMC6484353.[62]

3.2.2 Conference abstracts

- 1) **S. Shahrampour**, I. Vel, D. M. Middleton, M. Alizadeh, S.Naghizadehkashani, L. Krisa, A. E. Flanders, S. H. Faro, J. Cohen-Adad, F. B. Mohamed; “Magnetization Transfer Imaging in Normal Pediatric Spinal Cord: Evaluation and Assessment of Normative Data Across Various White Matter Tracts.” The Radiological Society of North America (RSNA), Chicago, USA, 2022 (Oral presentation).
- 2) Colline Blanc, **Shiva Shahrampour**, Feroze B Mohamed, Benjamin De Leener. “Automatic spinal cord segmentation in pediatric MR images: Preliminary Results”. 31st International Society for Magnetic Resonance in Medicine (ISMRM) Annual Meeting & Exhibition. London, UK, 2022.
- 3) J Heholt, **S Shahrampour**, F Mohamed, M Alizadeh, N Wintering, A Newberg. “N-Acetylcysteine Administration Affects Cerebral Blood Flow as Measured by Arterial Spin Labeling MRI in Patients with Multiple Sclerosis”. 59th Annual Meeting of the American Society of Neuroradiology (ASNR). San Francisco, CA, 2021.
- 4) **Shiva Shahrampour**, Benjamin De Leener, Mahdi Alizadeh, Devon Middleton, Laura Krisa, Adam Flanders, Scott Faro, Julien Cohen-Adad , and Mohamed FB. "Atlas-based Quantification of DTI measures in Typically Developing Pediatric Spinal Cord". 29th International Society for Magnetic Resonance in Medicine (ISMRM) Annual Meeting & Exhibition. Virtual Meeting, 2021 (Oral presentation).
- 5) **Shiva Shahrampour**, Benjamin De Leener , Devon Middleton , Mahdi Alizadeh , Laura Krisa , Adam Flanders , Scott Faro , Julien Cohen-Adad , and Feroze Mohamed. “Atlas-based Quantification of DTI measures in Typically Developing Pediatric Spinal Cord”.24th American Society of Spine Radiology (ASSR), virtual conference, 2021.
- 6) **Shahrampour S**, De Leener B, Middleton D, Jonnavithula K, Alizadeh M, Pedyakkal H, Krisa L, Flanders A, Faro S, Cohen-Adad J, Mohamed F. “Development of a Standardized Normative Pediatric Spinal Cord structural template”. 46th American Spinal Injury Association annual meeting (ASIA), virtual meeting, 2020. Award nominee (Oral presentation).

- 7) **Shiva Shahrampour** , Benjamin De Leener , Mahdi Alizadeh, Devon Middleton, Laura Krisa , Adam Flanders , Scott Faro , Julien Cohen-Adad , and Feroze Mohamed. "Development of Pediatric Spinal Cord White Matter Atlas: Preliminary Analysis". 28th International Society for Magnetic Resonance in Medicine (ISMRM) Annual Meeting & Exhibition. virtual conference, 2020.
- 8) **S Shahrampour**, B De Leener , D Middleton, M Alizadeh, L Krisa, A FLANDERS ,S Faro, J CohenAdad, FMohamed. Development of Pediatric Spinal Cord White Matter Atlas: Preliminary Analysis. 58th American Society of Neuroradiology meeting (ASNR), virtual conference, 2020.
- 9) **Shiva Shahrampour** , Benjamin De Leener , Devon Middleton , Kavya Jonnavithula , Mahdi Alizadeh , Hiba F Pedyakkal , Laura Krisa , Adam Flanders , Scott Faro , Julien Cohen-Adad , and Feroze Mohamed. "Development of a Standardized Normative Pediatric Spinal Cord structural template: Demonstration of an automatic estimation of Spinal Cord Cross Sectional Area measurements (SCCSA)." ISMRM 27th Annual Meeting & Exhibition. Montreal, Canada, 2019.
- 10) **S Shahrampour**, B De Leener , D Middleton , K Jonnavithula, M Alizadeh, H Pedyakkal, L Krisa, A Flanders, , S Faro, J Cohen-Adad, F Mohamed. "Development of Standardized Normative Pediatric Spinal Cord structural template: Demonstration of automatic estimation of Spinal Cord Cross Sectional Area measurements (SCCSA)". The American Society of Neuroradiology (ASNR) 57th Annual Meeting & The Foundation of the ASNR Symposium. Boston, MA, USA, 2019 (Oral Presentation).
- 11) Sona Saksena, Mohamed FB, Devon Middleton, Laura Krisa, Mahdi Alizadeh, **Shiva Shahrampour**, Adam Flanders, Scott H. Faro. "DTI of Spinal Cord Lesions of Varying Severity Based on MRI in the Entire Pediatric Spinal Cord". 57th Annual meeting of the American Society of Neuroradiology (ASNR), Boston, USA, 2019.
- 12) **S Shahrampour**, B De Leener , D Middleton , A Flanders , S Faro , J Cohen-Adad , M Alizadeh , L Krisa , F Mohamed. "Volumetric Analysis of Pediatric Spinal Cord Structural MRI data using SCT". The American Society of Neuroradiology (ASNR) 56th Annual Meeting & The Foundation of the ASNR Symposium. Vancouver, Canada, 2018. (Oral Presentation).
- 13) Devon Middleton, **Shiva Shahrampour**, Sona Sakesena, Chris J Conklin, Mahdi Alizadeh, Scott H Faro, Laura Krisa, MJ Mulcahey, Mohamed FB. "Spinal cord cross section and DTI by vertebral level correlate superior and inferior to injury". 27th Joint Annual Meeting ISMRM-ESMRMB. Paris, France, 2018.
- 14) Jennifer Muller BS MS; Mahdi Alizadeh; Sara Thalheimer BA; John James Pearce; Victor M. Romo MD; **Shiva Shahrampour** ; Feroze Mohamed ; Ashwini

D. Sharan MD; Chengyuan Wu MD, MSBmE. "Feasibility of White Matter Trajectory Analysis in Postoperative Diffusion Weighted Images for Patients with Deep Brain Stimulation". American Society for Stereotactic and Functional Neurosurgery; Biennial Meeting, assfn. Denver, USA, 2018.

- 15) Devon M Middleton, **Shiva Shahrampour**, Scott H Faro, Sona Saksena, Mahdi Alizadeh, Chris J Conklin, Laura Krisa, MJ Mulcahey, Mohamed FB. "Correlation of DTI Metrics to Spinal Cord Cross Sectional Area in Pediatric Subjects with Spinal Cord Injury". Annual meeting of the American Society of Neuroradiology (ASNR), Washington, USA, 2016.
- 16) Mohamed FB, **Shiva Shahrampour**, Devon M Middleton, Pallav Shah, Laura Krisa, MJ Mulcahey. "Pediatric Spinal Cord Atrophy Imaging". 4th joint meeting of ISCoS and ASIA. Montreal, CA, 2015.
- 17) **Shiva Shahrampour**, Devon M. Middleton, Winston Liu, Govind Nair, Steven Jacobson, Mahdi Alizadeh, John P. Gaughan, Pallav Shah, Scott H. Faro, Laura Krisa, MJ Mulcahey, Mohamed FB. "Pediatric Spinal Cord Atrophy Imaging: Quantitative Measures in Normal and Patients with Spinal Cord Injury". 53rd Annual meeting of the American Society of Neuroradiology (ASNR). Chicago, USA, 2015.
- 18) Mahdi Alizadeh, Mohamed, FB, Scott H. Faro, Pallav Shah, Chris J. Conklin, Devon M. Middleton, Sona Saksena, **Shiva Shahrampour**, MJ Mulcahey, "Intensity Inhomogeneity Correction in Clinical Pediatric Spinal Cord MRI Images", 41st Annual Northeast Bioengineering Conference, IEEE, 17-19 April, Troy NY, 2015.

CHAPTER 4

ARTICLE 1: DEVELOPMENT OF STANDARDIZED NORMATIVE PEDIATRIC SPINAL CORD STRUCTURAL TEMPLATE: DEMONSTRATION OF AUTOMATIC ESTIMATION OF SPINAL CORD CROSS SECTIONAL AREA MEASUREMENTS (SCCSA)

This paper presents the development of the structural pediatric template and demonstrates one of the utilization of the generated template as automated spinal cord cross sectional computation (SCCSA).

This work has been presented and published in the :

- 46th Spinal Cord Injury Association annual meeting (ASIA) in 2020.
- 27th International Society for Magnetic Resonance in Medicine Annual Meeting (ISMRM) in 2019.
- 57th American Society of Neuroradiology (ASNR) in 2019.

Title: Development of Standardized Normative Pediatric Spinal Cord Structural template: Demonstration of automatic estimation of Spinal Cord Cross Sectional Area measurements (SCCSA).

Authors: Shahrampour S., De Leener B., Middleton D., Jonnavithula K., Alizadeh M., Pediyakkal H, Krisa L., Flanders A., Faro S., Cohen-Adad J., Mohamed F.

Abstract:

The purpose of this work was to create a structural MRI based template of the normal pediatric spinal cord by combining T2w MR scans of several TD subjects and show its utility. For that, T2w 3D images from 30 TD subjects (6-16 yrs) were acquired in two slabs and stitched using a 3.0T MRI with the following imaging parameters: voxel size = $1 \times 1 \times 1$ mm³, TR=1500ms, TE=122ms. The following pre-processing steps were performed on all subjects before the actual template generation: (I) spinal canal centerline extraction. (II) Semi-automatic identification of intervertebral discs using a template-matching detection algorithm. (III) Slice-based intensity normalization: to normalize image intensity of the inside of spinal cord to the average intensity of the entire dataset. After successful preprocessing, the following steps were performed: (I) the spinal cord centerline and the intervertebral discs positions were semi-automatically extracted on all images using tools from Spinal Cord Toolbox. (II) The cord was then straightened, and vertebral levels were aligned using a Non-Uniform Rational Bezier Spline based nonlinear transformation. (III) An unbiased left-right symmetric template was constructed using a hierarchical group-wise nonlinear image-registration method (Automatic Nonlinear Image Matching and Anatomical Labeling). The template generation algorithm computes the average of all subjects iteratively and registers the images to this average nonlinearly. As a demonstration of the utilization of this template, spinal cord cross sectional area (SCCSA) was computed at disc levels in all the subjects.

We were able to illustrate the generated template, sagittal and coronal views along with the labeled vertebral bodies and segmented cord. Probabilistic map of white and gray matter and Cerebrospinal Fluid (CSF) as well as cord segmentation were also presented. The

similarity of the SCCSA measurements between the produced pediatric template and all the 30 subjects suggests the intactness of the overall structure of the spinal cord after straightening and deformation process during template registration.

To the best of our knowledge this work is the first to create a standardized template of spinal cord in pediatric subjects. We demonstrated the utility of this template in automatically estimating the SCCSA. Future work with a larger cohort with varied age ranges and gender is warranted.

Objective and Background:

Creation of the templates will allow for examination of the spinal cord in a standardized space for group studies and would remove, or greatly reduce, user variability during the analysis process. Although an adult template was recently created [57], there are no pediatric spinal cord templates which would enable group analysis and permit researchers to share, compare, and validate their results [43], [55], [63], [64]. The purpose of this study was to create the first known normative structural template for the pediatric spinal cord in the typically developing (TD) population. The proposed approach was following the process currently used by the Neuropoly team based at Polytechnique Montreal [65], to generate pediatric templates across the pediatric age range that will produce an unbiased average anatomical template of the pediatric spinal cord.

Methods and Materials:

- a) ***Subject sampling:*** A sample of 30 TD children between 6 and 17 years of age (12.38 ± 2.81) were recruited for this study. Subjects and parents provided written information assent and consent of the institutional review board (IRB) approved protocol. Children

were excluded if they were unable to tolerate MRI without sedation; have infantile, juvenile or adolescent idiopathic scoliosis or any abnormality of the nervous and/or musculoskeletal system, or chromosomal or genetic diagnosis. All subjects underwent a single scan without contrast that will include data collection for aims one and two outlined before. Prior to imaging data collection, subjects and guardians were interviewed about the subjects past medical history and known disabilities. Subjects also underwent a brief screen to assess muscle strength, balance, and sensation by trained research personnel.

- b) ***Image acquisition:*** The scans were performed using a 3T Verio MR scanner (Siemens, Erlangen, Germany) with four channel neck and an eight-channel spine matrix coil. All the subjects followed the scan protocol consisting of initial T2- w gradient-echo scout sagittal acquisition of cervical and thoracic spinal cord. The sagittal scans were used to prescribe axial sections of both cervical and thoracic spine. Imaging was then followed by obtaining an axial T2- w gradient echo (GRE), a sagittal T2-w 3D SPACE sequence; a sagittal turbo spin- echo (TSE) T1-w; a sagittal TSE T2-w and an axial diffusion-weighted scans. Diffusion tensor images were acquired axially using 2 overlapping slabs, to cover the entire cervical and thoracic spinal cord using an inner Field of View (iFOV) spin echo-based EPI pulse sequence with a tilted excitation plane. The iFOV DTI sequence consists of a spatially selective 2D radio frequency (RF) excitation profile[66]. The tilted excitation plane provides shorter 2DRF pulses and excludes the sidelobes in the refocusing plane. This sequence has the advantage of improving the signal to noise ratio (SNR) of the spinal cord as well as reducing distortion artifacts in DTI scans by enabling shorter phase encoding readout in the AP

direction. Manual shim and fat saturation volume adjustments were also performed before data acquisition to restrict the adjustment volume to the anatomy of interest as much as possible and to limit residual distortions and chemical-shift artifacts.

The imaging parameters of DTI acquisition for each slab is as follow: FOV=164 mm, phase FOV=28.4% (47 mm), 3 averages of 20 diffusion directions, 6 b0 acquisitions, b=800 s/mm², voxel size= 0.8×0.8×6 mm³, number of slices =40, TR = 7900ms, TE=110ms, acquisition time= 8:49 minutes per slab. The T2-weighted SPACE imaging parameters used were: voxel size 1×1×1 mm³, TR= 1500ms, TE= 122ms, flip angle= 140°, number of averages=2 and acquisition time=3 minutes and 17 seconds (for each overlapping slab). Cardiac gating was not used in this study as this will increase acquisition time which is not desirable in pediatric imaging. No subject was anesthetized in this study.

b-1) Optimization of DTI acquisition using reduced-field-of-view sequence: In order to optimize the rFOV sequence for imaging of the pediatric spinal cord, several diffusion directions (6, 12, 20 and 30), multiple signal intensity averages (1 to 4), and different b-values (0, 700, 800, 900, 1000 and 1200 s/mm²) were examined. The final parameters (number of directions=20, b=800s/mm², and number of averages=3) were selected to ensure the relatively short acquisition time tolerable for pediatric imaging while maintaining high spatial resolution that provides good accuracy for the estimate of the diffusion tensor.

c) **Image Processing:** This processing step is following the approach by Neuropoly team based at Polytechnique Montreal [67] . Initially, an intensity normalization procedure was applied to all images to normalize image intensity of the inside of spinal cord (the

cord as opposed to CSF) to the average intensity of the entire dataset. Then the following sequence of steps were performed to generate the template: **1.** The spinal cord centerline was automatically identified using a regularized support vector machine method trained on T2 images.[68] **2.** The spinal cord was automatically segmented using a 3D mesh propagation algorithm [69] **3.** The intervertebral disc positions were automatically extracted using a template-matching detection algorithm [70] **4.** The spinal cord was then straightened and vertebral levels were aligned using a Non-Uniform Rational Bezier Spline (NURBS) based nonlinear transformation [71]. An additional step of straightening procedure was the vertebral level alignment using vertebral based referential system [72] which was also performed. **5.** An unbiased left-right symmetric template was constructed using a hierarchical group-wise image-registration method [73], (Figure 20) illustrates a summary of template creation steps. The image registration method used in this procedure is based on the nonlinear registration engine of Automatic Nonlinear Image Matching and Anatomical Labeling (ANIMAL) [74]. Overall, this template generation algorithm was performed by iteratively computing the average of all images and nonlinearly registering the images on that average. This procedure was repeated several times with finer grid size and blurring kernels: 4 iterations at 4 mm resolution, 4 iterations at 2 mm, 4 iterations at 1 mm and 4 iterations at 0.5 mm. Left-right symmetry was achieved by flipping all initial images in the left-right direction and integrating them as input into the iterative template generation procedure. While the original images have a 1 mm³ isotropic resolution, the iterative nonlinear averaging process allowed to increase resolution of the final template and to keep high-contrasted structures. Therefore, the final resolution

of the template is set to $0.5 \times 0.5 \times 0.5 \text{ mm}^3$ for a size of $201 \times 201 \times 1200$ voxels. A slice-based intensity normalization procedure was also applied on the final template to homogenize the image intensity inside the spinal cord and thus correct for the intensity bias related to inhomogeneous transmit and receive B1 fields. **6.** The white and gray matter probabilistic atlas was registered to the generated template using BSplineSyN transformation, as previously described [75]. This entire procedure was undertaken for all the 30 subjects from various age groups, and a structural template was created. Recently, this procedure has been well tested and used to create the first adult spinal cord template by the Neuropoly team[65].

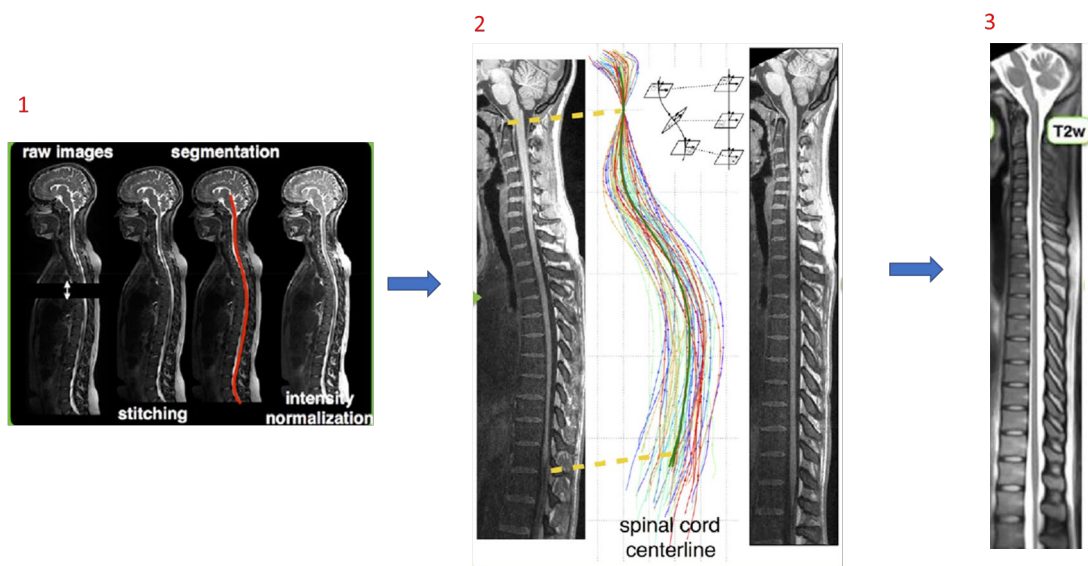


Figure 20: Illustrates a summary of template creation steps. 1) shows pre-processing of T2-w stitched spinal cord data. spinal cord canal is also semi-automatically extracted. 2) shows the straightening process of the spinal cord for each subject. 3) illustrates non-linear registration of T2-w images into PAM 50 space. The image and the paragraph were adapted from (De Leener. B. et al, Neuroimage (2018)) .

To perform the SCCSA measurements, T2-w images from both 3D isotropic acquisitions were stitched together using Siemens composing software in order to create a single contiguous volume containing the entire cervical and thoracic spinal cord. Images were reviewed post-stitching in order to verify success of the operation and to ensure a contiguous cord without gaps. Measurements of SCCSA were then performed using volumetric spinal cord masks generated by the spinal cord toolbox (SCT)[56] following the creation of the template, SCCSA measurements along with the Coefficient of Variance (CV) were computed for both generated template and individual TD subjects (averaged across the subjects) for selected cord levels. The Intra Class Correlation (ICC) is used to examine the agreement of the measurements between the two groups.

Results:

To illustrate the generated template, sagittal and coronal views along with the labeled vertebral bodies and segmented cord are depicted (figure 21). Probabilistic map of white and gray matter and Cerebrospinal Fluid (CSF) as well as cord segmentation are also presented.

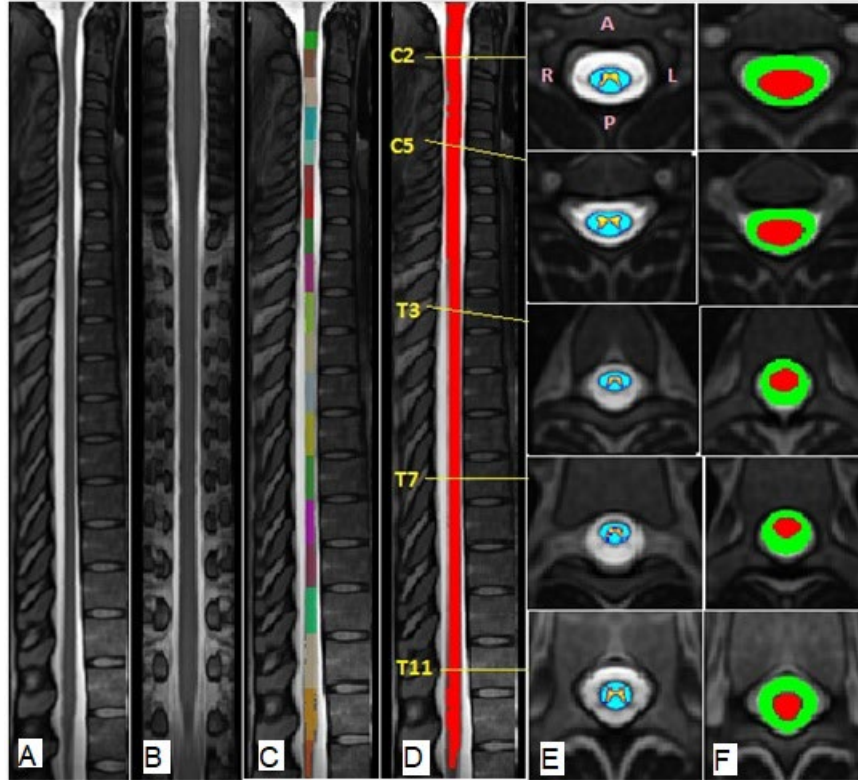


Figure 21: Illustrates the, generated pediatric template. The left four images show the (A) sagittal and (B) coronal view of the template along with the (C) vertebral labels and (D) segmented cord in red. The right two images show (E) probabilistic map of white and gray matter as well as (F) Cerebrospinal Fluid (CSF) and cord segmentation.

The SCCSA of the produced pediatric template is computed as $46.5 \text{ mm}^2 \pm 12.5$ (average across levels) and the same measurement of average SCCSA across all 30 subjects is $47 \text{ mm}^2 \pm 9.6$. Both SCCSA measurements are plotted and the similarity in the shapes of the plots suggests the intactness of the overall structure of the spinal cord after the straightening and deformation process during template registration (figure 22).

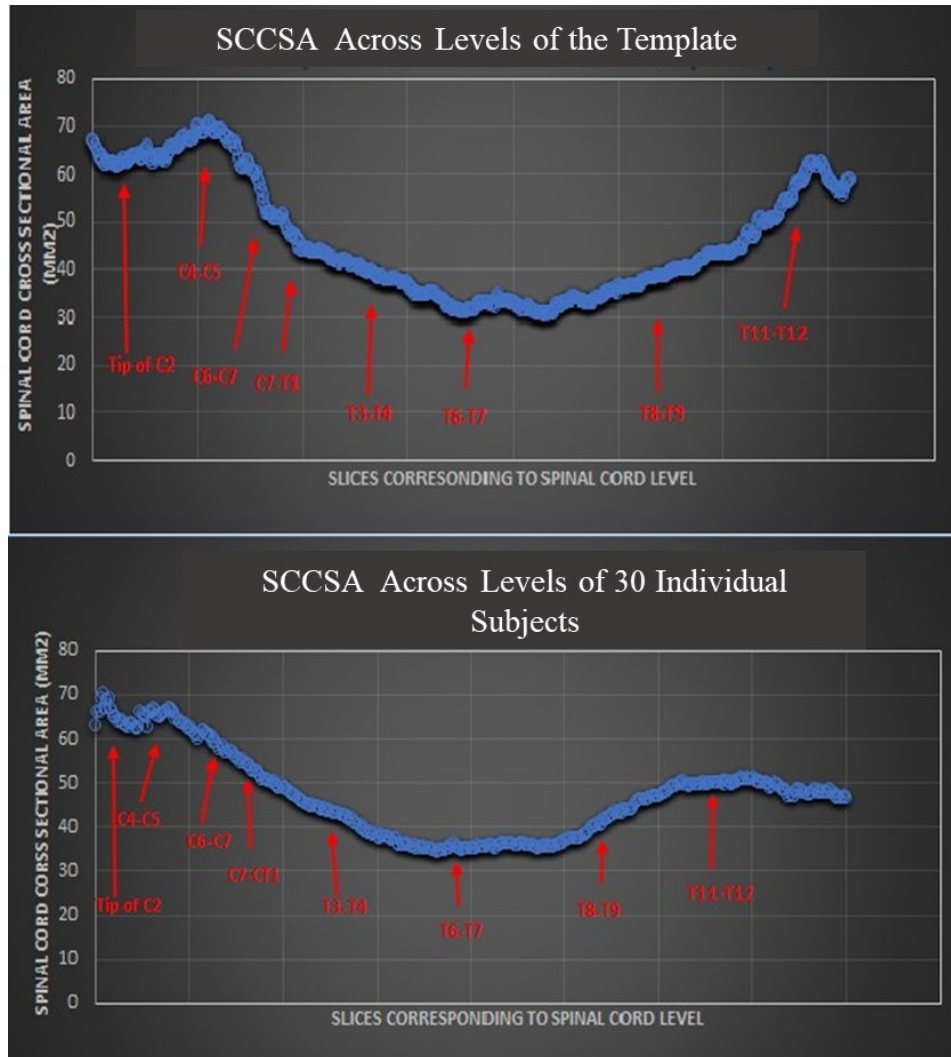


Figure 22: The graph shows the SCCSA of the pediatric template (average across levels: $46.5 \text{ mm}^2 \pm 12.5$)(top panel). This average is compared to average SCCSA across all 30 subjects (average across levels: $47 \text{ mm}^2 \pm 9.6$)(bottom panel). This suggests that SCCSA is preserved between native subjects' space and the template.

The SCCSA measurements for both groups along with the Coefficient of Variance (CV) for selected disc levels are shown in (table-1). The (ICC) of 0.94, indicates a strong agreement between the measurements in both groups.

	Pediatric Template		Average of all 30 Subjects	
	SCCSA mm ² ±Sd	CV%	SCCSA mm ² ±Sd	CV%
C1-C2	62.27± 0.53	0.00%	64.08 ±0.95	0.01%
C4-C5	68.78± 0.6	0.00%	65.15 ±1.4	0.02%
C6-C7	48.62 ±1.64	0.03%	57.23 ±0.89	0.01%
C7-T1	44.72 ±1.03	0.02%	49.4 ±0.71	0.01%
T3-T4	35 ±0.54	0.01%	42.93 ±0.41	0.00%
T6-T7	33.33 ±0.65	0.01%	35.16 ±0.27	0.00%
T8-T9	38.89 ±0.23	0.00%	43.67 ±0.38	0.00%
T11-T12	56.21 ±1.76	0.03%	50.11 ±0.17	0.00%

Table-1 : Table shows comparison of SCCSA (mm²) measurements between the generated template and the average of all the 30 subjects along with Coefficient of Variation (CV) in selected intervertebral discs.

Conclusion:

To our knowledge, this work is the first to create a standardized template of spinal cord in pediatric subjects. The utility of this template in automatically estimating the SCCSA is also demonstrated and this will warrant future work with larger cohorts.

CHAPTER 5

ARTICLE 2: ATLAS-BASED QUANTIFICATION OF DTI MEASURES IN A TYPICALLY DEVELOPING PEDIATRIC SPINAL CORD.

Normative data characterizes what is usual in a defined population at a specific point or period of time. Normative data contributes to research and clinical practice, improve the understanding of the natural history of common conditions, and support the development of appropriate standards of clinical care for physicians. Therefore, the motive for this article was, to establish a range of atlas-based normative values of 34 white matter tracts at the C3 level of spinal cord for children (male and female), ages 6-17 years old. To the best of our knowledge such data sets are not currently available and will immensely help in evaluation of pediatric spine neurodevelopment, comparisons with patients with SCI, and have the potential to aid in clinical diagnosis.

This study has been published in the American Journal of Neuroradiology (AJNR) in Sep 2021, vol. 42(9), 1727-1734.

DOI: <http://dx.doi.org/10.3174/ajnr.A7221>

Title: Atlas-Based Quantification of DTI Measures in a Typically Developing Pediatric Spinal Cord.

Authors: Shahrampour S., De Leener B., Alizadeh M., Middleton D. , Krisa L., Flanders A., Faro S., Cohen-Adad J., Mohamed F.

Abstract:

Using multi-parametric MRI data of the spinal cord in typically developing pediatric subjects, this study had three objectives: i) to develop a processing pipeline for generating pediatric spinal cord white matter tracts using atlas-based methods, ii) to derive normative values of DTI indices for various white matter tracts, iii) and to examine age-related changes in the normative DTI indices along the extracted tracts. For that, diffusion weighted and T2 weighted scans of 30 subjects between the ages of 6 and 16 were acquired and registered to a template in the Spinal Cord Toolbox. The DTI indices for various white matter regions were extracted at C3 vertebral level and examined for the effects of laterality, functionality, and age on all the 34 extracted WM regions. The atlas-based approach used in this study proposed an automated pipeline incorporating post-processing steps and template registration technique that improved the accuracy and speed of measurements and provided normative values for white matter tracts in typically developing pediatric subjects.

Introduction:

In humans, the spinal cord functions as a signaling pathway between the extremities and the brain structures. All the primary sensory and motor functions are conducted through the spinal cord. The spinal cord WM contains a wide range of fibers that are different in size, density, and functionality [76]. For example, fasciculus gracilis, which is involved in transmitting various functions such as vibration, conscious proprioception, and fine touch sensations are composed of small size packed fibers whereas spinocerebellar tracts (which carry proprioceptive and cutaneous information) are composed of large-size and less dense fibers[77], [78]. Injury caused to the spinal cord due to traumatic or non-traumatic events

and subsequently to these specialized white matter tracts in general leads to specific dysfunction and various clinical disabilities. Clinical entities that lead to axonal loss (e.g multiple sclerosis) [79] are associated with symptoms such as loss of motor functions and sensation, while spinal cord injury can produce paraplegia or quadriplegia [80]. Therefore, study of spinal cord WM and characterizing its microstructure non-invasively will help in accurate understanding and diagnosis of disease and pathologies. Furthermore, identifying the WM pathways in the cord that may have been damaged is crucial in helping the prognosis and functional recovery and disease management.

In recent years DTI, have shown promise as a non-invasive imaging biomarker for evaluating the integrity of the spinal cord WM. DTI provides information related to tissue microstructure and fiber organization of the WM in a non-invasive manner [41]. For that, DTI is a strong biomarker candidate for detecting spinal cord pathologies through quantification of its metrics such as fractional anisotropy (FA), mean diffusivity (MD), radial diffusivity (RD) and axial diffusivity (AD) [46], [81]. Despite challenges associated with spinal cord DTI imaging such as small area of the cord, reduced signal-to-noise ratio (SNR), cerebral spinal fluid (CSF) pulsation, and patient motion, various improvements in scanning methodologies and post processing methodologies, such as zoomed and reduced field of view MRI techniques and optimized protocols has made spinal cord imaging clinically feasible. In the last decade, numerous studies have demonstrated the utility of DTI as a non-invasive tool to assess normal and abnormal adult spinal cord WM microstructure [43], [44], [82]–[84]. However, studies addressing the pediatric spinal cord have been limited [45], [46]. This stresses the importance of studying pediatric spinal cord anatomy, specifically all the various white matter structures at a microstructural level, and

establishing normative values for various diffusion-derived indices obtained from these WM structures. This information could help with monitoring normal spinal cord development in growing children and evaluating age-related differences in the specific WM tracts (i.e. corticospinal tracts). Recent studies [48], [49] have shown the usefulness of these normative values, showing a good correlation with the values acquired from clinical examination of motor and sensory levels in patients. Few other works in pediatric patients have demonstrated DTI indices differences between age and cord regions [45], [46]. However, all of these studies have used manual delineation of the white matter structures in the pediatric spinal cord using expert pediatric neuroradiologists or neuroscientists [45]. Recently, automated methods have been developed for the extraction of various white matter structures on the adult spinal cord. This enables better quantification and alleviates any subjectivity not only in the identification of these small structures but also in accurate measurements of functional and structural metrics. In this work, we have extended these methods to the pediatric spinal cord. To the best of our knowledge, there are no studies to date that have used automated methods to delineate WM structures in the pediatric spinal cord. Therefore, the aim of this work was 3-fold: i) to develop a processing pipeline for the atlas-based generation of pediatric spinal cord WM tracts. ii) to derive atlas-based normative values of the DTI parameters for various WM pathways at the C3 level of the TD pediatric spinal cord. iii) to examine the age-related changes in the derived normative DTI parameters along the extracted pathways.

Methods and Materials:

Study Design and Population:

All subjects provided written informed consent obtained under a protocol approved by the Temple University institutional review board (IRB). The study used 30 typically developing (TD) pediatric subjects (age range 6-16 years, mean age 12.38 ± 2.81). All subjects went through a brief assessment, using a standard neurologic screening form, requesting information on medical history related to neurologic injuries as well as a physical assessment of sensory and motor functions. Subjects with any abnormality of the nervous system were excluded. Only subjects with no evidence of spinal cord injury or neurologic deficit were included in the study.

MR Imaging Protocol:

The scans were performed using a 3T Verio MR scanner (Siemens, Erlangen, Germany) with a four-channel neck and an eight-channel spine matrix coil. All the subjects followed the scan protocol consisting of initial T2-weighted gradient-echo scout sagittal acquisition of the cervical and thoracic spinal cord. The sagittal scans are used to prescribe axial sections of both the cervical and thoracic spine. Imaging was then followed by obtaining an axial T2-weighted gradient echo (GRE), a sagittal T2-weighted 3D SPACE sequence; a sagittal turbo spin-echo (TSE) T1-weighted; a sagittal TSE T2-weighted and an axial diffusion-weighted scans. We only used the 3D SPACE and diffusion data in this study. Diffusion tensor images were acquired axially using two overlapping slabs, to cover the entire cervical and thoracic spinal cord using an inner Field of View (iFOV) spin echo-based EPI pulse sequence with a tilted excitation plane. The iFOV DTI sequence consists of a spatially selective 2D radio frequency (RF) excitation profile [66]. The tilted excitation

plane provides shorter 2DRF pulses and excludes the sidelobes in the refocusing plane. This sequence has the advantage of reducing distortion artifacts in diffusion-weighted scans by enabling faster k-space encoding via a reduction of phase-encoding steps. Manual shim and fat saturation volume adjustments were also performed before data acquisition to restrict the adjustment volume to the anatomy of interest as much as possible to limit residual distortions and chemical-shift artifacts. The imaging parameters of diffusion weighted acquisitions for each slab are as follows: FOV=164 mm, phase FOV=28.4% (47 mm), 3 averages of 20 diffusion directions, 6 b0 acquisitions, $b=800 \text{ s/mm}^2$, voxel size= $0.8 \times 0.8 \times 6 \text{ mm}^3$, number of slices =40, TR = 7900 ms, TE=110 ms, acquisition time= 8.49 minutes per slab. The T2-weighted SPACE imaging parameters used were: voxel size= $1 \times 1 \times 1 \text{ mm}^3$, TR=1500 ms, TE=122 ms, flip angle= 140° , number of averages=2 and acquisition time=3.17min (each overlapping slab).

Image Preprocessing:

To perform atlas-based analysis of WM tracts, the DTI data from all the individual subjects were motion corrected and later registered to the template (PAM 50)[57]. In this study, all the pre and post-processing of the data was performed within the framework of the Spinal Cord Toolbox (SCT)[56]. A detailed description of these processes is stated below and illustrated in (figure 23).

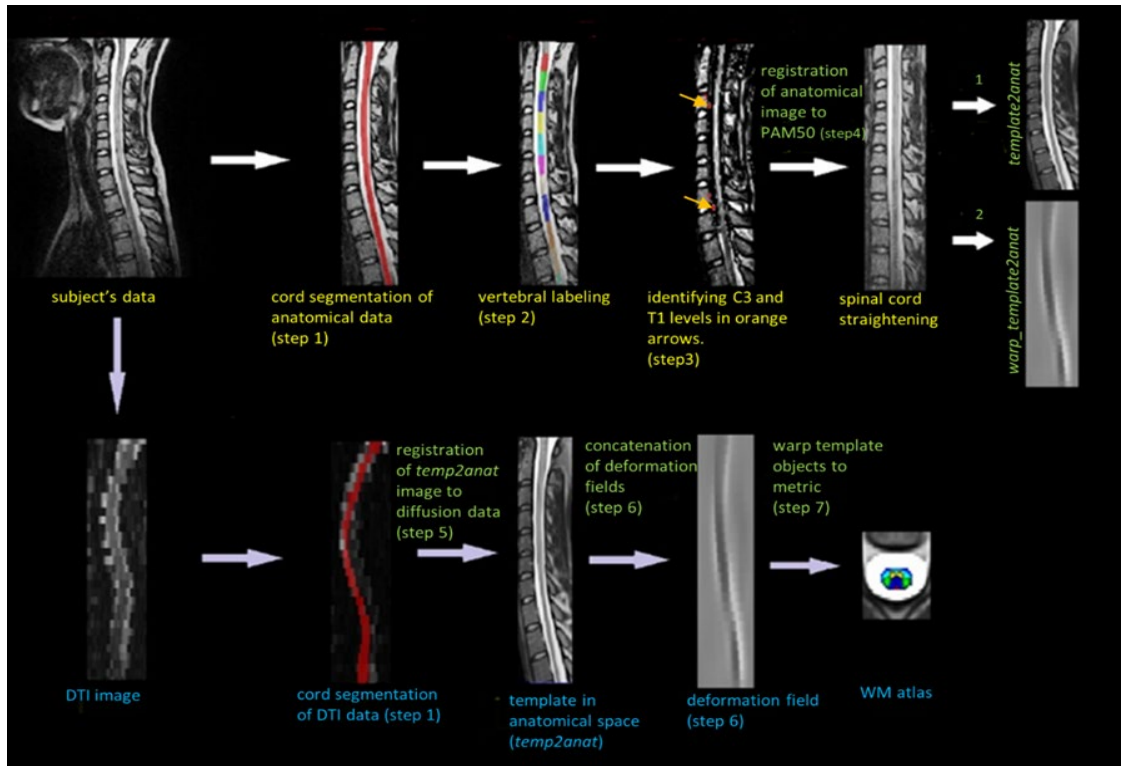


Figure 23: Illustrates an Overview of the template registration pipeline. Initially, T2-weighted scans are registered to the template (top row). DTI data acquired during the same scan session are then registered to the anatomical data and PAM 50 objects are warped to diffusion data (bottom row) to generate the pediatric WM spine atlas. (Shahrampour et al, 2021).

The initial motion-correction was done using a slice-wise algorithm from SCT. The *SliceReg* algorithm, estimates the translation of the diffusion data in a slice-by-slice manner and applies the regularization along the Z-direction.

Procedure for Data Registration to the Template:

After performing motion correction on the diffusion data, the data was registered with the PAM50[57] template (the PAM50 template and atlas has been used in numerous studies

and validated and well suited for our study as well [57], [85], [86]. This is done following a two-step multimodal registration process within SCT. The multimodal registration consists of a registration between the PAM50 template and high-resolution anatomical (T2-w) image of all the individual subjects. The second registration is between the template (in anatomical space) and the diffusion data of the same subjects. In the end, the PAM50 atlas which contained the various WM tracts was warped to each subject-specific diffusion data. The following steps describe the registration process in detail. For better clarity, these steps are also identified in (figure 23).

1. Segmentation of the spinal cord using *PropSeg* [69] module: The cervical spine was segmented using both structural T2-w image and diffusion data of each individual subject. Segmentations were checked visually and corrected manually in case of any issues.
2. Labeling anatomical image: The anatomical images from the previous step, were labeled resulting in a segmented cord labeled with vertebral levels. This was done using the *sct_label_vertebrae* module [70].
3. Identifying two specific vertebral levels: To perform a more accurate registration between the PAM50 and the pediatric anatomical images two vertebral levels were identified as landmarks (C3 and T1). This was done using *sct_label_utils* module. The orange arrows in (figure 23) indicate these two levels.
4. Registration to the template: Each individual T2-w image was registered to PAM 50 using the *sct_register_to_template* module. In this step, the spinal cord is straightened first, and then local deformations are applied using multi-step nonlinear registration constrained in the axial plane and regularized in Z direction. The outputs of this step were the T2-w

template in the anatomical space (*template2anat*), and the corresponding warping field (*warp_template2anat*).

5. A second registration is then performed using the *sct_register_multimodal* module: In this step, the image *template2anat* from the previous step was registered to each subject's diffusion data. This will yield the template in the individual's diffusion native space (*template2diff*) as well as the corresponding warping field (*warp_anat2diff*).

6. Concatenation of deformation fields: The warping fields from the last two steps of registrations were concatenated to create a single global transformation between the template and diffusion data (*warp_template2diff*).

7. Obtaining white matter atlas: The global warping field is used to warp template objects (i.e. WM atlas) to the diffusion data.

Quantifying DTI Metrics Using the Atlas:

After the registration was verified visually for each individual subject, diffusion tensor estimation was performed on the cervical cord. DTI metrics were extracted (*sct_extract_metric*) for each subject at C3 level using a weighted average method [75]. This resulted in quantifying DTI metrics of FA, MD, AD and RD for 34 extracted WM labels from PAM 50 template. The labels were automatically assigned to multiple locations of the cord containing the effective voxels from the respective tissue. Of the 34 labels; 30 represent individual sensory and motor WM tracts; three represent combined labels of dorsal funiculi (DF), lateral funiculi (LF) and ventral funiculi (VF), and one label was assigned to represent the entire WM itself. The normative values were obtained by

averaging all of these WM measurements across all 30 subjects. ROI names and abbreviations are provided in Appendix B and C.

Statistical Analysis

To perform the statistical analysis we used, Prism – GraphPad 8.0 a DOS based scientific graphing application. DTI normative measurements of all 34 labels were plotted using violin plots. To check if there was a significant difference between the laterality (left/right), functionality (motor/sensory) and age-related changes of all the tracts a one-way analysis of variance (ANOVA) was used. Linear regression analysis was used to compare age-related changes of DF, LF and VF labels using DTI metrics. To study the age-related changes, the subject population was divided into two age groups: one group of younger children from 7-11 years old and older group from 12-16 years old. The age groups were defined based on a previous pediatric study [45]. Throughout the study, a P-value of 0.05 was used to determine the statistical significance.

Results:

a) Extracted WM tracts

(Figure 24), shows the results of the analysis of this study and it presents an image of the extracted WM tracts. (Figure 24-A) shows a high-resolution spinal cord white matter atlas derived from Gray's Anatomy Atlas, adapted from Levy et al [75]. (Figure 24-B) illustrates a subset of selected tracts overlaid on a b0 image at C3 level in a representative subject from this study. The labeled WM tracts in this figure are as follows: green_1: right lateral corticospinal tract, green_2: left lateral corticospinal tract, dark blue_3: right fasciculus cuneatus, dark blue_4: left fasciculus cuneatus, red_5: right fasciculus gracilis, red_6: left

fasciculus gracilis, yellow: gray matter, light blue: unlabeled white matter. (Figure 24-C) shows a sagittal T2-weighted cross section of spinal cord marked at C3 level, the level corresponding to the WM tracts shown in (figure 24-B).

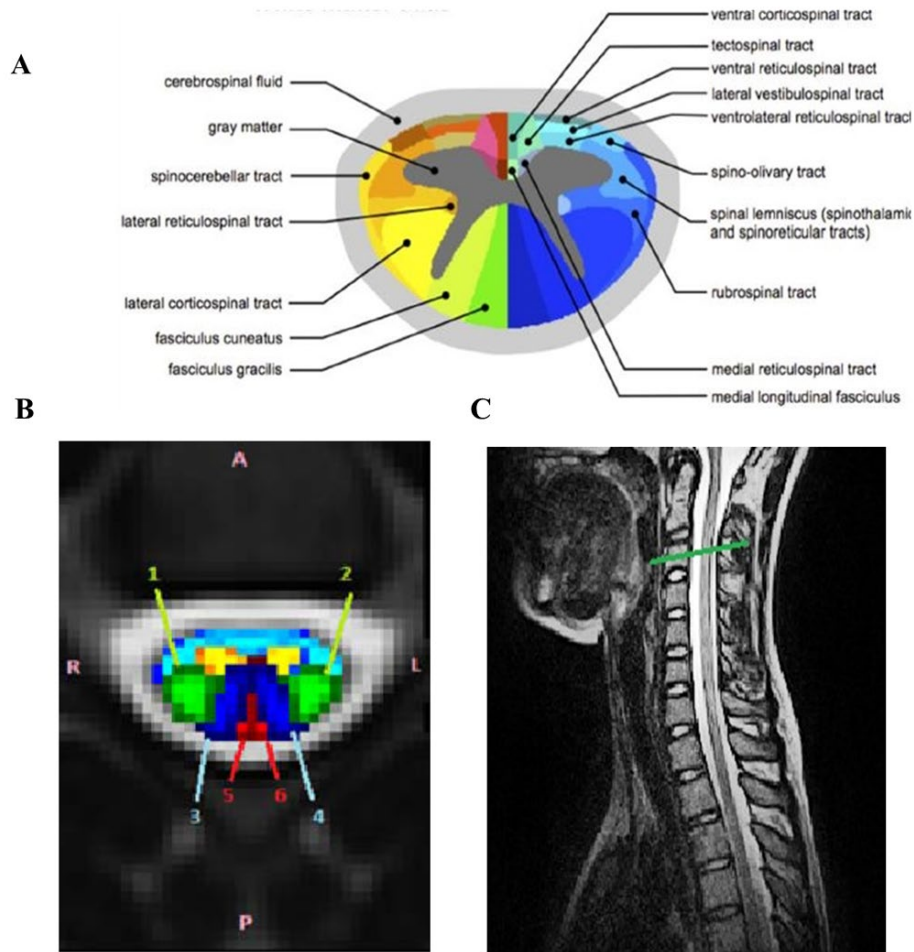


Figure 24: Illustrates the spinal cord WM atlas: **A.** An atlas of spinal white matter tracts derived from the Gray’s Anatomy atlas, adapted from Levy et al [75] **B.** Generated white matter atlas of pediatric spinal cord overlaid on a b0 image. The selected tracts are labeled with multiple colors. **C.** The C3 level is marked with green color on the sagittal T2-weighted scan.

b) Normative values:

The pipeline developed in this study was successful in delineating DTI values from all the various tracts across all 30 subjects (figure (25A-D)). The violin plots are divided into the dorsal, lateral and ventral funiculi as well as combined tracts (WM, DF, LF and VF). Closer inspection of inter-quartile ranges in these violin plots showed low between-subject variability in all the diffusion measurements. The FA appeared to be the highest in dorsal column tracts with a range of 0.61 to 0.62 and a mean of 0.62 and std of 0.09 (0.62 ± 0.09). The corresponding values for lateral and ventral columns were 0.47 ± 0.12 and 0.28 ± 0.12 respectively. FA, MD and RD had higher level of dispersion in all the tracts including dorsal, lateral and ventral when compared to AD. The coefficient of variation (CV) of the measurements in FA was lowest in dorsal column with the value of 14.62% and highest for ventral tracts with a value of 45.74%. The minimum and maximum measurements in MD were 23.75% and 34.06% from dorsal to ventral tracts and in RD from 33.43% to 40.90% respectively. AD showed less variability across all the tracts, with CV of 22% in dorsal columns to 26% in ventral tracts. Ventral funiculi regions present larger variation compared to other white matter tracts. Considering the “combined tracts” WM measurements, FA had the lowest variation with CV of 18.6%, followed by the second lowest in AD (CV=20.11%). VF has higher variation in all the metrics with an average CV of 33% compared to DF and LF ($CV_{(DF)}= 22\%$, $CV_{(LF)}=25\%$).

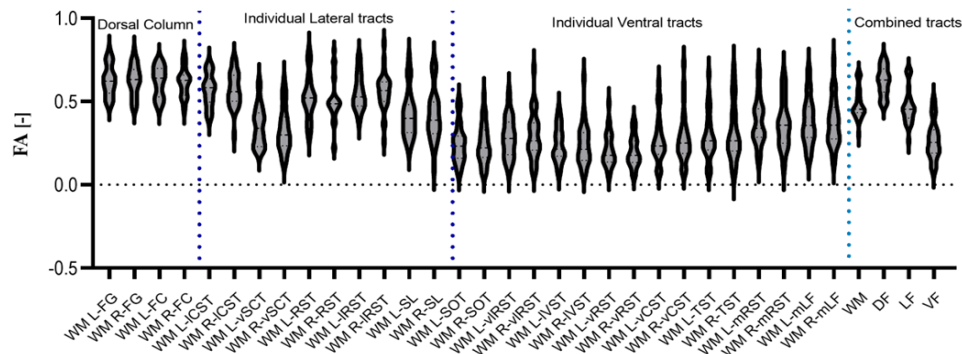
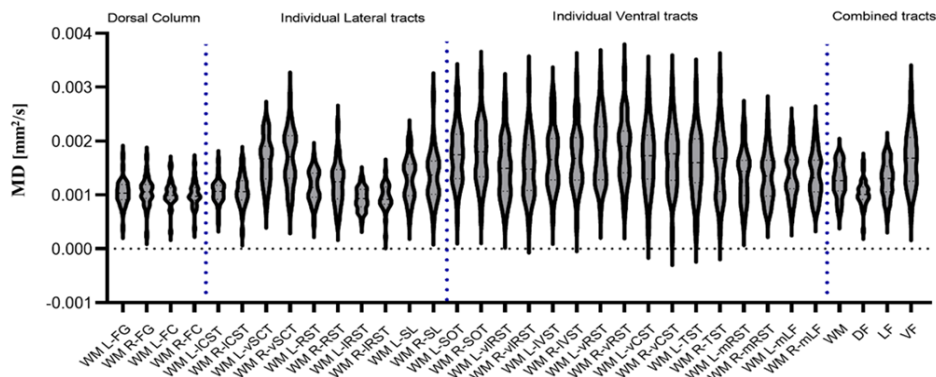
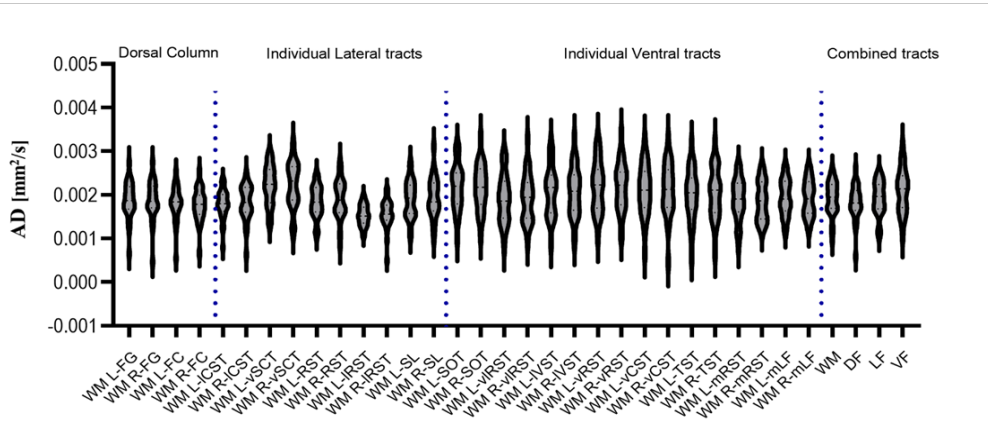
A**B**

Figure 25: Violin plots of normative FA (A), MD (B), AD (C), and RD (D) indices averaged across 30 healthy pediatric subjects for 34 ROIs. ROIs are subdivided in to 30 WM tracts; 3 combined labels of DF, LF, and VF; and 1 label for the entire WM. IVST indicates lateral vestibulospinal tract; vRST, ventral reticulospinal tract; FC, fasciculus cuneatus; ICST, lateral corticospinal tract; TST, tectospinal tract; SL, spinal lemniscus (spinothalamic and spinoreticular tracts); FG, fasciculus gracilis; SOT, spino-olivary tract; mLF, medial longitudinal tract; vCST, ventral corticospinal tract; vRST, ventrolateral reticulospinal tract; IRST, lateral

reticulospinal tract; RST, rubrospinal tract; vSCT, ventral spinocerebellar tract; mRST, medial reticulospinal tract; WM, white matter; DF, dorsal column; LF, lateral funiculi; VF, ventral funiculi; L, left; R, right.(Shahrampour et al., 2021)

C



D

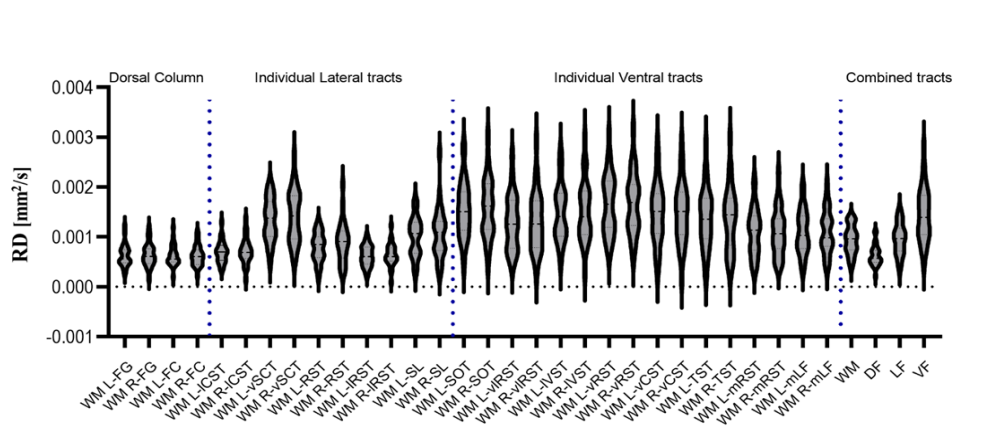


Figure 25- Continued

Table-2 , compares the values obtained for selected tracts displayed in (figure 24). The ‘left fasciculus gracilis’ presents the highest FA of 0.66 which is averaged among all 30 subjects with the lowest variation (CV=14.02%). FA was the lowest in “Right lateral corticospinal tract” with higher CV of 18.26%.

<i>Group</i>	<i>WM tracts</i>	<i>FA</i> <i>(Average± SD)</i>	<i>MD</i> <i>(Average± SD)</i>	<i>RD</i> <i>(Average± SD)</i>	<i>AD</i> <i>(Average± SD)</i>
1	Right lateral corticospinal tract	0.56 ±0.09	1.27 ±0.20	0.87 ±0.24	2.09 ±0.27
2	Left lateral corticospinal tract	0.60 ±0.08	1.17 ±0.14	0.78 ±0.18	1.95 ±0.24
3	Right fasciculus cuneatus	0.64 ±0.08	1.14 ±0.18	0.72 ±0.18	2.00 ±0.31
4	Left fasciculus cuneatus	0.66 ±0.08	1.13 ±0.15	0.68 ±0.18	2.05 ±0.26
5	Right fasciculus gracilis	0.65 ±0.06	1.20 ±0.19	0.72 ±0.20	2.16 ±0.33
6	Left fasciculus gracilis	0.66 ±0.07	1.20 ±0.19	0.72 ±0.20	2.15 ±0.31

Table.2. Results of DTI normative values for 6 selected tracts illustrated in (figure24-B).

C) Effects of Laterality, functionality, and age:

Results of ANOVA using FA, MD, RD and AD showed no effect ($P > 0.05$) between a total of 15 left and 15 right tracts. However, when tested for functionality (i.e. whether a tract is sensory or motor), FA and MD showed significant differences ($P_{FA} = 3.7E^{-5}$, $P_{MD} = 0.043$), but not AD and RD.

Examining the effect of age with each single individual tract as well as combined tracts revealed significant difference between the maturation of some tracts and age. Here, among all the 34 selected tracts only the left spinal lemniscus (spinothalamic and spinoreticular tracts) showed an effect with age using MD, RD and AD ($P < 0.05$). Moreover, linear regression analysis results showed a positive correlation between FA and age (figure 26), while MD, RD and AD showed a negative correlation in all three selected combined tracts (dorsal, ventral and lateral funiculi). MD showed significant differences with age in VF and DF ($P < 0.05$), whereas AD showed an effect in LF and VF but not DF. Similar analysis showed no significant differences for FA but a significant effect for RD in all three combined tracts of DF, LF and VF ($P < 0.05$).

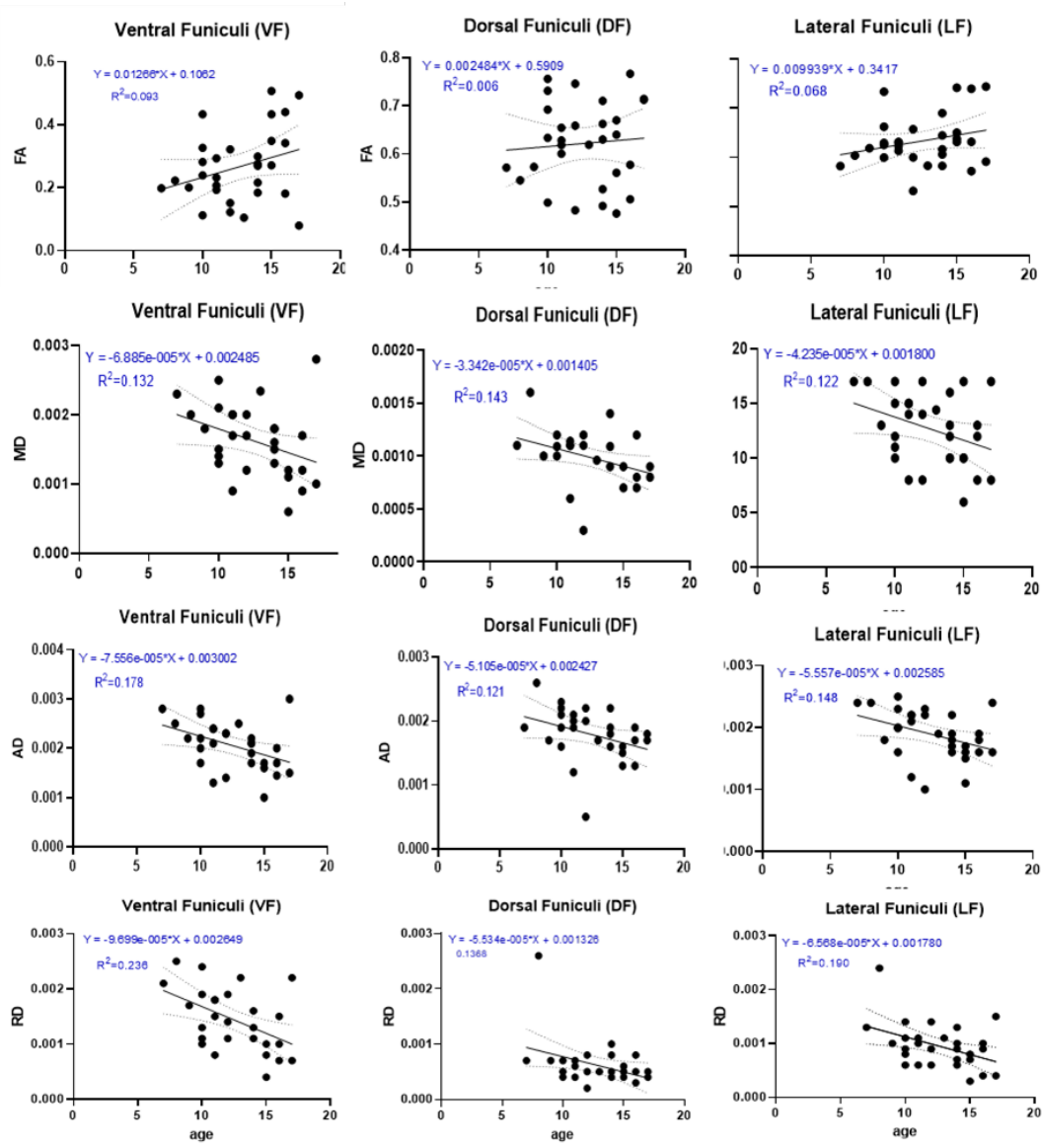


Figure 26: Linear regression plots showing the relationship between age and FA (A), MD (B), AD (C), and RD (D) in the ventral, lateral, and dorsal funiculi. Solid lines indicate the age-related trend, and dashed lines indicate 95% confidence intervals.

Discussion:

In this study, we showed the feasibility of acquiring spinal cord DTI data on the entire spinal cord of all 30 typically developing children. We also developed a processing pipeline for the automatic generation of pediatric spinal cord WM tracts. This pipeline is unique in terms of registering the diffusion data to an external template and enabled the extraction of spinal cord white matter tracts in healthy pediatric cohorts. The quantification of DTI indices was performed using PAM 50[57] from SCT and was followed by establishing DTI normative values for 34 WM tracts. Former studies have addressed the generation of the spinal cord atlas in the adult population [56], [75], however, no atlas of white matter pathways in the pediatric spinal cord is currently available. This study is the first to propose a pipeline for automated WM tract extraction in pediatrics enabling atlas-based analysis of the cord.

WM tract generation pipeline:

WM atlas of spinal cord based on DTI, provides new anatomical information by delineating WM tracts and enables automated atlas-based analysis of WM pathways. The extracted tracts in this study are aligned with PAM 50, T2-weighted template which makes quantification of DTI metrics more accurate by minimizing the interpolation errors during diffusion metric extraction. Registration of the diffusion data to the template guarantees that the tracts are also aligned with the individual subject's spinal cord.

In SCT a digitized version of *Gray's Anatomy* spinal cord white matter atlas [87] is merged with PAM50. This atlas is probably the most complete atlas of human anatomy with one limitation that it doesn't account for inter-subject variability of the spinal cord shape which is a contributing factor as shown in previous studies [88]. A multi-step registration method was used to register the pediatric DTI data to the adult PAM50 atlas. To make this process

more feasible we used a tool from SCT to create two landmarks at C3 and T1 vertebral levels of the cervical cord in the anatomical image of each subject. Using these two labels a series of affine and non-linear transformations were performed to register the anatomical image to the template. This method considers the height difference between the adult and pediatric populations and rectifies the discrepancies. In the final step of the multi-scale registration, we used a BSplineSyN [89] algorithm to maintain a smooth deformation of the cord shape. We visually examined the outcome of the registration in each individual subject and the result was satisfactory. There is currently no known automatic method to delineate the exact location of WM tracts *in vivo*. The suggested method provides a more reliable (free from user-bias and objectivity) and more accurate measurements compared to manual ROI drawing that is heavily dependent on the user knowledge of anatomy and prone to partial volume effect contamination [45], [90]–[93].

DTI metrics quantification of the spinal cord

In this work the normative values of diffusion data were extracted at C3 vertebral level for ventral, dorsal and lateral spinal cord funiculi and other subsets of WM tracts in TD pediatric population. These values could be useful when comparing healthy and patient populations [94]. Differences in quantitative metrics in specific WM pathways may provide some additional insight into disease progression. Although there are several animal studies that have investigated the DTI indices in various WM structures such measurements in the pediatric spinal cord don't exist yet [95]–[97].

Injury to the spinal cord can cause severe consequences to the individual's quality of life by leading to a kind of clinical disability or dysfunction. Hence, it's important to investigate

WM tract damage, to better assist with prognosis and manage the disease treatment and recovery.

In this study, we focused only on a single C3 level of the spinal cord to perform our analysis. This was due to the better performance of proposed segmentation and registration algorithms with lower interrater variability that was reported by *Prados et al [98]*. In another study performed by *Losseff et al [99]*, they found that measurements done at C2/C3 level are the most reproducible ones when looking at spinal cord atrophy. *Stevenson et al [100]*, also highlight the importance of studying the cord at the C2/C3 level and recommend that measurements at this level could eliminate and reduce the variability that occurs using measurements at other cord levels. This could be because of the excellent contrast of the CSF and the cord at the C3 level.

Investigating the function of age and DTI indices, the DTI indices trend of change in the brain WM during maturation are characterized by increasing FA and decreasing AD, RD and MD, with cognitive regions developing later than sensorimotor regions [101], [102] Generally, AD shows weaker development pattern across regions and a decreasing pattern with age in cortical white matter [102], [103] While our observed age-related trend of DTI indices matches that of other spinal cord studies [45], [104], the lack of significant effect with decrease in AD observed in dorsal columns suggests that proportion of larger sized axons increases with the child growth [46].

While examining the effect of age on each individual tract in this study we found no significant difference between FA values of lateral, ventral and dorsal funiculi. However, radial, axial and mean diffusivities values of the ventral funiculi showed significant effects with age-related changes. These differences could reflect the variability of axon diameter,

axon density, and spacing between these funicles [76] containing different kinds of tracts. Although there was no significant difference observed between FA and age, the correlation of age with FA specifically and other DTI-derived indices generally, was consistent with former studies [45], [104], [105] [106].

In this study, we observed that there is a relationship between diffusivity metrics and the maturation of some tracts (i.e. Spinothalamic tract). This could be because of the myelination process in different tracts. Myelination constitutes the last stage of the development of the WM which begins in utero in the second trimester of pregnancy and continues up to the end of adolescence[107]–[110] There are several factors that affect the rate of myelination including the type of fiber; where faster rates are observed in sensory compared to the motor [111]. We believe this could justify the significant difference of Spinothalamic tract (a somatosensory tract) maturation with DTI indices in our study.

We also showed that there's no significant difference in the laterality (left/right) of the tracts that suggest structural similarity between the left and right-sided tracts. In a study done by *Duval et al [112]*, they have shown similar average axon diameters in identical tracts from the left and right side of the spinal cord. Although there was no significant difference in the laterality of the tracts in our work, ANOVA showed a significant difference between sensory (i.e. fasciculus gracilis, fasciculus cuneatus) and motor (i.e. CST) pathways. We tend to believe this is related to the microstructural organization of sensory and motor WM tracts. Data on axonal morphometry in spinal cord is scarce and there's very little data in the literature regarding myelin sheath thickness. In general, the tracts show variation in morphometric features like axon density, axon diameter and spacing. The anatomic variation of axon diameter is pronounced whereby the dorsal

column fasciculus gracilis contains predominantly small diameter axons, whereas the corticospinal tract in the lateral and ventral columns contain a combination of large and small diameter axons [113]. The other anatomic variation to consider is the fiber density variation along the entire length of the spinal cord especially at the exit points of brachial and lumbosacral plexus[87]. In a study by *Ohnishi* group [114], they reported a decrease in a number of myelinated fibers of the fasciculus gracilis in humans between C3 and T5. *Terao et al* [115], also reported an association of axonal diameter variation with the vertebral level in human lateral CST. These observations are in accordance with previous histology work [116] in human, emphasizing the importance of broader studies of histological validation in ex vivo human spinal cord.

Limitations:

One limitation in this study was the accuracy during the registration of the diffusion data to the template space. Due to diffusion data SNR limitations and smaller size of the cord in children, there could be higher intra subject variability resulting from spatial misalignment during registration. This limitation highlights the need for tools that provides robust pre-processing, normalization and motion correction for spinal cord diffusion data. Another limitation stems from the intrinsic variability of spinal cord diffusion imaging which induces inaccuracies in metrics quantification. This issue along with the selected registration algorithm, metric extraction method and partial volume effects contribute to both inter-subject variability and inter-ROI variability, particularly in a smaller cord size. An additional limitation is the small number of subjects as well as the narrow age range of our population as opposed to other pediatric diffusion studies[46]. All these limitations

could be contributing factors in observed discrepancies in our results compared to other similar studies.

Conclusions:

We showed the feasibility of a fully automated WM tract extraction in the pediatric spinal cord. We also established normative values for DTI-derived indices by looking at specific WM regions of the cord. These results show that presented values are microstructure-sensitive and evolve in the pediatric spinal cord during development. This warrants future work with spinal cord patients (i.e. spinal cord injury) as well as examinations of DTI-derived metrics in the entire cord as compared to a single C3 slice.

CHAPTER 6

ARTICLE 3: QUANTITATIVE MAGNETIC RESONANCE IMAGING TO CHARACTERIZE THE MACRO AND MICROSTRUCTURAL CHANGES IN TYPICALLY DEVELOPING PEDIATRIC SUBJECTS AND PATIENTS WITH SPINAL CORD INJURY

In this study we extended the application of DTI to investigate the microstructural and macrostructural changes in pediatrics with spinal cord injury. The overall goal of the study was to incorporate qMRI to quantify these changes remote from the lesion in SCI children and to determine whether DTI and other metrics of the study provide insights and measures of cord abnormalities.

This study has been submitted to the Journal of Neurotrauma in March 2023 and is under review.

Title: Quantitative magnetic resonance imaging to characterize the macro and microstructural changes in typically developing pediatric subjects and patients with spinal cord injury.

Authors: Shiva Shahrapour, Benjamin De Leener, Mahdi Alizadeh, Devon M. Middleton, Laura Krisa, MaryJane Mulcahey , Adam E. Flanders, Scott H. Faro, Julien Cohen-Adad, Feroze B. Mohamed

Abstract

Lack of clarity about the neurological consequence of SCI in children causes speculation about diagnoses and treatment effectiveness. This study aims to measure macrostructural and microstructural neurodegenerative changes remote from a spinal cord injury lesion in children with SCI and compare them with TD children, using qMRI. We hypothesize that the observed changes in those regions of the cord can provide insights into the full extent of injury.

Fifteen SCI patients (AIS A-D, mean age of 12.8 ± 3.1 years) and fifteen TD children (mean age 13.4 ± 2.3 years) were recruited. The scans were obtained using a 3T Verio MRI scanner. Diffusion tensor imaging (DTI) metrics of FA, MD, RD and AD along with the CSA of the whole cord, WM and GM were quantified at C2-C3 and T2-T3 levels using spinal cord toolbox (SCT). An atlas-based approach was used to extract the DTI metrics in 7 selected WM tracts. To examine the difference between the two populations, diffusion metrics as well as T2* WM/GM intensity ratios and CSA measurements were computed for both groups. A two-sample *t-test* was used to test the effect of all the aforementioned imaging metrics between SCI and TD subjects. Relationships between all the metrics and clinical scores in SCI subjects were assessed using Pearson correlation.

Results of *t-tests* showed a significant decrease in FA measurements in all the 7 WM tracts in SCI patients when compared to TDs. MD, AD and RD metrics showed significant increase in SCI subjects ($p < 0.05$). Significant atrophy was observed in the whole cord, WM and GM of the patients compared to TDs in both upper cervical and upper thoracic measurements ($p < 0.05$).

A significant decrease was also found in T2* WM/GM intensity ratio measurements of the SCI subjects in comparison to TDs. Results of the Pearson correlation revealed a good correlation between all the qMRI metrics. The correlation between the qMRI metrics and the ISNCSCI scores in SCI patients was moderate.

This study shows the feasibility of utilizing advanced qMRI protocols that are sensitive to spinal cord pathology and have the potential to predict outcomes in children with SCI. When comparing normal and SCI pediatrics, DTI was sensitive in detecting functional changes of the spinal cord in chronic SCI in regions remote to the injured site. Atrophy measurements also showed potential to become a powerful clinical tool in SCI. The findings for T2* WM/GM intensity ratio are encouraging and indicate the use of this potential biomarker to quantify WM injury.

Keywords: Pediatric, Spinal Cord Injury (SCI), Diffusion Tensor Imaging (DTI), qMRI

Introduction:

Traumatic spinal cord injury (tSCI) is a condition that arises from a mechanical damage to the spinal cord resulting in disruption of the spinal cord [117] . However, non-traumatic injury could be caused by various reasons such as developmental (i.e. spina bifida) and vascular anomalies (i.e. angiomatous malformations), inflammation (i.e. transverse myelitis), ischemia (i.e. cord infarction), pressure on the cord due to expanding lesions (i.e. abscess or tumor extrinsic or intrinsic to the spinal cord). The neurological consequences of SCI from both conditions could lead to demyelination[118]–[121] , axonal damage of spinal nerve fiber tracts (damage to the white matter) [122], [123] or ischemic changes [120], [124]. The degree of neurologic damage is clinically expressed by a level and severity of injury which is based upon clinical assessment of motor and

sensory function as described by the International Standards for Neurological Classification of Spinal Cord Injury (ISNCSCI)[125]. Therefore, SCI can negatively influence the life expectancy and functional capacity of the patients. To help guide therapies and improve functional recovery of these patients, it is paramount to identify the underlying pathophysiology that occurs at the microstructural level.

Prior studies suggest that[62], [64], [126], [127] quantitative magnetic resonance imaging (qMRI), and in particular diffusion tensor imaging (DTI), can infer microstructural changes in patients with spinal cord injury. The spinal cord abnormalities can be detected at the microstructural level with the metrics offered by DTI. In an earlier study, *Saksena et al*[62], utilized DTI to investigate the microstructural changes in a select few WM regions remote from the lesion in pediatrics with SCI using a manual method. *Poplawski et al*[33], performed a study on 23 acute cervical SCI patients. The focus of the study was to determine the accuracy of DTI parameters in predicting the neurological injury in adult cervical SCI. These studies used the manual method to identify the region of interest to obtain DTI metrics. In addition to DTI, CSA measurements are shown to be a strong indicator of spinal cord atrophy and can be computed using T2 [61] and T2* weighted scans. T2*-w images provide good contrast between GM and WM structures, facilitating their segmentation and CSA calculation[128]. *Middleton et al*[61], successfully deployed a semi-automated method to measure CSA of the whole spinal cord using T2-w scans. *Cohen-Adad et al* [35], [129] has shown that injured spinal cord WM is hyperintense on T2*-w images due to pathologic conditions. Moreover, injury to the WM can lead to decreased gray-white contrast and this can be quantified by measuring the T2* WM/GM signal intensity ratio.

In this study, to determine the severity of the neurodegenerative changes induced by the injury, we compared the macrostructural and microstructural derived metrics in typically developing and children with SCI at two different sites of C2-C3 (upper cervical) as well as T2-T3 (upper thoracic). These measured regions were remote from the isocenter of the injury. All prior published pediatric spinal cord studies have employed manual delineation of WM structures in the pediatric spinal cord [62], [126]. In this study, however, we utilized a fully automated atlas-based approach to identify the seven WM regions to further describe the observed DTI changes remote from the lesion. To measure the cord atrophy, we also incorporated an automated CSA measurement of the cord, differentiating WM and GM at selected cord levels (i.e. C2-C3 and T2-T3 levels). The atlas-based approach in our study alleviates any subjectivity in identifying WM structures which to the best of our knowledge has not been used in other pediatric studies.

The purpose of this study was to employ automated extraction of WM (atlas-based approach) in a pediatric spinal cord injury population compared to normal TD controls to derive whole cord CSA, WM, and GM CSA, FA, MD, RD, AD, and T2* WM/GM ratio metrics to distinguish the two population.

Methods and Materials:

a) Patients Demographics:

All subjects provided written informed consent obtained under a protocol approved by the Temple University institutional review board (IRB). A retrospective study used 15, TD pediatric subjects (mean age 13.4 ± 2.3 years old) and 15 chronic SCI subjects (mean age of 12.8 ± 3.1 years old) who underwent spinal cord imaging in 2014-2017. (Table-3), shows

the demographic information of the TD and SCI subjects along with the extent of the lesion in SCIs as defined by conventional structural MRI scans. The superior and inferior margins of the lesion presented on MRI in these subjects were determined based on the neurological level of Injury (NLI) by the ISNCSCI examination (table-3). After a brief assessment of TD subjects using neurological screenings, those with any pre-existing abnormality of the nervous system were excluded. The inclusion criteria for SCI subjects were: stable SCI, being at least 6 months post-SCI. The exclusion criteria included being unable to tolerate MRI without sedation, scoliosis, any abnormality (not associated with the SCI) of the nervous or musculoskeletal system, or orthodontic hardware or other internal metallic material. There were 8 patients who had non-traumatic SCI caused by reasons other than motor vehicle accidents: subjects 118 and 142 had spinal cord infarction and subjects 115, 202, 206, 216, 219, and 220 had focal transverse myelitis (TM) with chronic residual neurological symptoms.

	Group				
<i>Variable</i>	<i>TD (n=15)</i>	<i>SCI (n=15)</i>	<i>P-value</i>		
Age	13.43 ±2.38	12.86 ±3.13	0.57		
Sex	M=7, F=8	M=7, F=8			
<i>SCI subj ID</i>	<i>Superior and Inferior margins of the lesion present on MRI</i>	<i>NLI</i>	<i>AIS grade</i>	<i>ISNCSCI score</i>	
				<i>motor scores</i>	<i>sensory scores</i>
115	mid C5 to mid C6	C6	B	45	108
118	mid T10 to mid T12	T10	B	50	70
142	T11 to mid T12	L2	C	50	112
202	mid C5 to mid C7	L2	- *	50	112
204	C6/C7 to conus	T3	A	50	44
206	- **	C1	D	50	68
207	- **	C5	D	42	112
208	mid C6 to C7-T1	C8	A	50	36
209	T8/T9 to conus	T9	A	50	64
212	T10 to T11	T12	A	50	79
215	mid C6 to T1/T2	C8	A	50	31
216	mid T12 to upper L1	L2	D	50	112
219	mid T4 to mid T6	T4	D	50	81
220	mid T8 to mid T10	L3	D	50	109
221	C6/C7 to mid T6	T3	B	50	44

* Couldn't determine the score since the subject didn't complete the AISA

** No abnormal signal and no hemorrhage observed on MRI

Table-3: The table illustrates the demographic of participants of this study (including 15 SCIs and 15 TDs).

All of the SCI subjects underwent a full neurological evaluation based on ISNCSCI which included the ASIA Impairment Scale (AIS). The assessment consisted of manual muscle strength testing of five upper and lower extremity muscles bilaterally, testing of light touch and sharp–dull, and a rectal examination of sensory and motor function[125]. The upper extremity and lower extremity total motor possible scores ranged from 0 to 25 for each limb. The sensory score ranged from 0 to 56 for each modality on each side. The ISNCSCI total motor score refers to the sum of the bilateral upper extremity and lower extremity motor scores, and the ISNCSCI total light touch sensory score is the sum of right and left light touch scores. (table-3), summarizes these scores, and based on the scores the patients were graded as follows: five AIS A, three AIS B, one AIS C, five AIS D, and one unknown.

b) MR Imaging Acquisition:

All the subjects underwent scanning on a single 3T Verio MR (Siemens Medical Systems) using a similar scan protocol. Scans were all acquired in two slabs, to cover both the cervical and thoracic spine. Scan protocol consisted of an initial T2-weighted gradient-echo scout sagittal acquisition of the cervical and thoracic spinal cord. Followed by an axial T2-weighted gradient recalled-echo (MEDIC-GRE) sequence with parameters as follows: FOV= $159 \times 159 \text{ mm}^2$, Matrix size= 384×384 , TR= 878 ms, TE=7.8 ms, slice thickness= 6 mm, flip angle= 25° , read-out bandwidth= 280 Hz per pixel and the acquisition time = 2 minutes and 7 seconds (per slab). The scan protocol continued by acquiring a sagittal T2-weighted 3D sampling perfection with application-

optimized contrasts by using different flip angle evolution (3D-SPACE) sequence and axial diffusion-weighted scans. The T2-weighted SPACE imaging parameters used were: voxel size = $1 \times 1 \times 1 \text{ mm}^3$, TR = 1500 ms, TE = 122 ms, nominal flip angle = 140° , number of averages = 2, and acquisition time = 3 minutes and 17 seconds (for each overlapping slab, i.e. cervical slab and thoracic slab). Diffusion images were acquired axially using an inner FOV spin-echo-based EPI pulse sequence with a tilted excitation plane. The inner FOV diffusion-weighted sequence consists of a spatially selective 2D radiofrequency excitation profile [66]. The imaging parameters of the diffusion acquisition for each slab (two slabs in total) are as follows: FOV = 164 mm, phase FOV = 28.4% (47 mm), 3 averages of 20 diffusion directions, 6 b = 0 acquisitions, b = 800 s/mm^2 , voxel size = $0.8 \times 0.8 \times 6 \text{ mm}^3$, number of slices = 40, TR = 7900 ms, TE = 110 ms, acquisition time = 8 minutes and 49 seconds per slab.

Cardiac and respiratory gating was not used to keep the scans as short as possible [61].

c) Image processing:

To process the images, the spinal cord toolbox (SCT) [56] was used, which is an open-source library of tools and contains modules for analyzing the multi-parametric MRI scans of the spinal cord.

c-1) Data pre-processing:

All the diffusion images were motion-corrected using *sct_dmri_moco* module from SCT. *SliceReg* is one of the key features of the applied motion correction algorithm, which estimates the slice-by-slice in-planar translations within the diffusion image to correct for intra-participant motion and eddy current artifacts.

c-2) Diffusion tensor imaging (DTI) measurements:

To perform an atlas-based analysis of WM tracts, the pediatric diffusion data from all 15 TD and 15 SCI subjects were registered to the PAM50[57]. The registration procedure is done following a 2-step registration process[59], using diffusion data as well as the corresponding T2-w scans of each subject. The first step of the registration involves registering the anatomical scan of each subject to the PAM 50 space. This is followed by the second registration between the anatomical data and the diffusion data of the same subject. Next, the warping fields from these 2 registrations are concatenated to produce a single transformation field between the PAM 50 and the diffusion data. Then, all DTI maps of FA, MD, AD, and RD are obtained by fitting a diffusion tensor model to the motion-corrected data, using a robust tensor fitting algorithm[130]. Finally, to extract the desired WM tracts, the single warping field that was obtained before, is warped into the DTI maps. After visually verifying the successful registration for every single subject, all the four DTI metrics are quantified at the C2-C3 (upper cervical) and T2-T3 (upper thoracic) for both TD (figure 27-a) and SCI (figure 27-b) subjects. This step resulted in DTI values of FA, MD, RD, and AD for 7 extracted WM labels from PAM50 atlas (figure 27-c). The WM labels selected in this study consist of 4 sensory tracts of right/left fasciculus gracilis, right/left fasciculus cuneatus, 2 motor tracts of right/left lateral corticospinal tract (CST), and 1 label that represents the entire WM itself (figure -28).

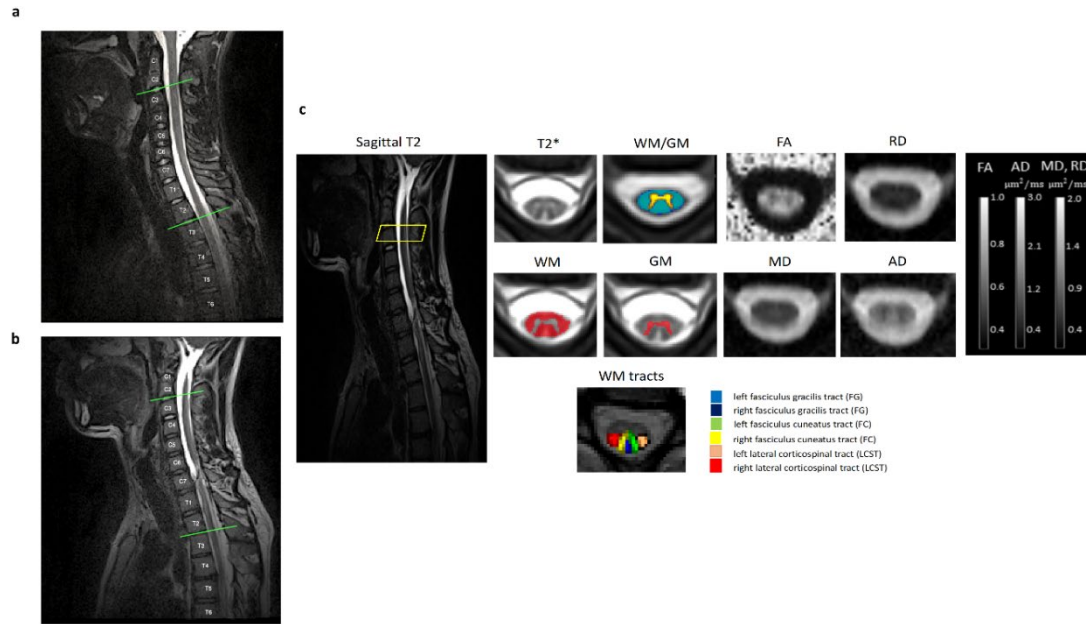


Figure 27: Illustrates (a) The C2-C3 and T2-T3 levels are marked as green on the sagittal T2 scan of a TD subject. (b) The same representative levels on a sagittal T2 scan of an SCI subject with an injury at C7-T1 level and AIS grade of A. (c) a panel of qMRI metrics of our study demonstrating the measurements at C2-C3 level. The DTI maps of FA, MD, RD and AD along with WM, GM CSA and WM/GM map are presented at the top of the panel. The ‘atlas’ image at the bottom of the panel corresponds to the selected WM tracts in this study for the atlas-based analysis.

c-3) Spinal cord cross-sectional area measurements:

Spinal cord cross-sectional area (CSA) measurements were performed for the whole cord, WM, and GM at the aforementioned levels. Initially, the spinal cord in all the 30 subjects (TD as well as SCI) is segmented automatically using a deep learning algorithm (*sct_deepseg_sc*) in SCT[56]. The segmentation is performed on the T2-w and T2*-w images of each subject. After each segmentation is performed, the segmented masks were

revised and corrected manually by the user in case of an error in the generated mask. Following the segmentation step, the segmented T2-w scans of each individual subject were first registered to PAM50, to match the vertebral levels of all the pediatric data to that of the PAM50 template. This will produce two forward (*-initwarp*) and backward (*-initwarpinv*) warping fields that were used in the next step. Then, T2*-w scans were registered to the PAM 50 template using the warping fields from the initial registration. This registration was done by applying the *sct_register_multimodal* module that will register the images nonlinearly to the template/atlas in SCT. Finally, the WM and GM cross-sections were calculated automatically for corresponding vertebral levels (figure 27-c & figure 30). To measure the whole cord CSA, the T2-w segmentations are used to extract the cord area. Subsequently, T2* WM/GM signal intensity ratios are computed for 7 previously described labels (WM tracts) by using the SCT probabilistic atlas (figure 29). This atlas-based method corrects for the partial volume effects by applying the maximum posteriori[75].

d) Statistical Analysis:

GraphPad Prism software 9.0 (GraphPad Software), a DOS-based scientific graphing application, was used for the statistical analysis of the data. For ease of visualization, CSA measurements of the WM, GM, and the whole cord were plotted using violin plots. Comparison of MR imaging metrics (i.e. DTI metrics, T2* WM/GM ratio) between TD and SCI were made using *a two-sample t-test* for the selected tracts. Line plots with error bars were used to demonstrate the difference between the two populations. Relationships between normalized MR imaging metrics (i.e. T2* WM/GM ratio, WM-CSA, GM-SCA, cord-CSA, FA, MD, RD and AD) were assessed using Pearson correlation coefficients

and presented in the correlation matrix (figure 31). This relationship is also analyzed against ISNCSCI clinical scores.

Results

a) Tract Specific Microstructural Changes:

The results demonstrate that atlas-based DTI analysis of WM tracts in SCI subjects shows significant changes in diffusion metrics across the various WM structures when compared with TD controls. The results were consistent for both upper cervical and upper thoracic measurements. The line plots (figure-28) demonstrate the difference between the two populations for all the extracted diffusion metrics in all 7 tracts. (Figure-29) shows the significant difference in T2* WM/GM intensity ratio between TD and SCI.

a-1) Upper-Cervical (C2/C3) analysis of the cord comparing SCI and TD:

There were statistically significant changes observed in FA between the two populations at C2-C3 level. The FA in the dorsal column tracts ranged from 0.56 to 0.46 with a mean of 0.54 ± 0.01 in TD subjects as opposed to the mean FA of $0.48 \pm 4E^{-03}$ in SCI (figure 28). The corresponding values for the right and left lateral corticospinal columns were 0.49 ± 0.03 and $0.40 \pm 4E^{-03}$, respectively. This shows a combined 8 to 20 percent decrease in FA when comparing SCI with TD subjects ($P < 0.05$). MD ($P = 0.019$) and AD ($P = 0.0068$) were both significantly increased in the patients compared to TDs (figure 28-c, 28-g). However, there were no significant changes observed in the increased RD in SCI patients (Figure 28-e). The increase in MD values associated with SCI patients varies from 19% in dorsal columns to 22% in motor tracts of lateral corticospinal columns. Comparing SCI with TDs, the total increase ranges from 12% and 25% in AD and RD, respectively.

The diffusion measurements showed higher levels of dispersion in SCI patients as opposed to TD. This variation was also higher in left and right corticospinal tracts when compared to dorsal columns. The coefficient of variation (CV) of the measurements in FA ranged from 23% to 38% in SCIs compared to 16 to 21 percent in TD cases. The CV was less in AD measurements for SCI, with a maximum of 15% in the left lateral corticospinal tract and 19% in TD for the same WM tract. These variations were 36% in RD in SCI patients and 29% for MD. The corresponding values in TD subjects are 27% and 18%, respectively. In SCI patients, the mean FA across the WM tracts ranged from 0.27 ± 0.061 to 0.44 ± 0.09 . These patients are identified with neurological injury levels (NLI) at the cervical cord. The AIS grade for these patients was AIS B, and AIS D, respectively.

a-2) Upper-Thoracic (T2/T3) analysis of the cord comparing SCI and TD:

Similar analyses have been done for the upper thoracic (T2-T3) level measurements. The FA changes in TD subjects at T2-T3 level ranged from 0.52 ± 0.12 to 0.47 ± 0.11 ; with 0.52 observed in the right fasciculus gracilis tract and 0.47 observed in the right corticospinal tract (figure 28-b). However, the maximum FA observed at this level in SCI patients is 0.34 ± 0.13 followed by the minimum FA of 0.28 ± 0.13 . The max and min FA observations in SCI patients represent the right fasciculus gracilis and right lateral corticospinal tract. The percentage decrease in FA of the SCI patients compared to TDs ranges from a minimum of 31% decrease in FA of the left fasciculus cuneatus tract to a maximum of 39% decrease in FA of the right lateral corticospinal tract. The MD (figure 28-d), AD (figure 28-h), and RD (figure 28-f) all significantly increased in SCI patients when compared to TDs. The mean increase in MD is 28% ($P < 0.0001$), followed by a

39% increase in RD measurements in SCIs ($P < 0.0001$). The lowest mean increase is observed as 0.11 % in AD values of SCI patients as opposed to TD subjects.

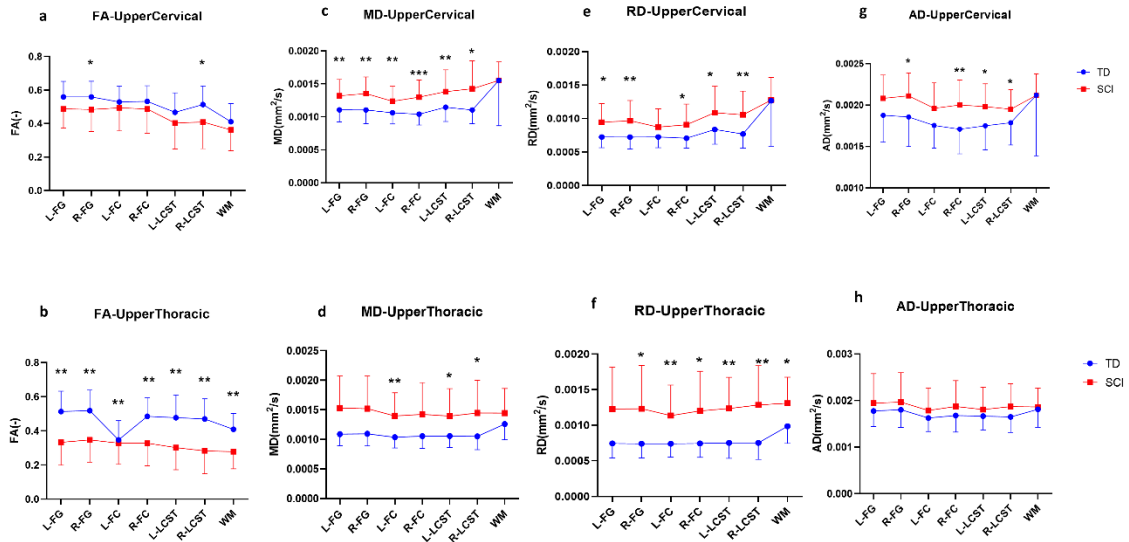


Figure 28: Illustrates DTI metrics of FA (a, b), MD (c, d), RD (e, f) and AD (g, h) averaged across all TD and SCI subjects for 7 WM tracts showing mean and standard deviation bars. The 7 WM tracts are: FG, fasciculus gracilis; FC, fasciculus cuneatus; LCST, lateral corticospinal tract; WM, white matter. L, left; R, right. Figs (a), (c) and (e) and (g) represent measurements at C2-C3 level and Figs (b), (d), (f) and (h) are corresponding measurements at T2-T3 level. There was a significant decrease observed in mean FA of our SCI subjects compared to TDs. MD, RD and AD showed significant increase in SCIs. (* $p < 0.05$; ** $p < 0.01$; *** $p < 0.001$).

The CV of the measurements at the T2-T3 level followed the same trend as upper cervical measurements. The variations of values obtained in patients were higher compared to TD subjects, and essentially higher in motor tracts than sensory ones. A CV of 42% is observed

in FA and RD values of SCI patients with CV of 29% in AD measurements. The corresponding values in TD subjects are CV of 27% in FA and 28% in RD. The measurements in AD show less dispersion in both SCI and TD populations. In the patient population, the mean FA across all the selected WM tracts ranged from 0.14 ± 0.01 to 0.41 ± 0.05 . The SCI patient with FA of 0.14 had an NLI of C8 with an AIS grade of A, whereas the FA of 0.41 was associated with a patient with NLI of T12 and AIS grade of A.

a-3) T2 WM/GM ratio performance:*

There were significant differences between SCI patients and TD subjects when comparing the T2* WM/GM ratio at both upper cervical and upper thoracic levels (figure-29a & b). Two-sample *t-tests* of these measurements showed a significant decrease in SCI patients when compared to TDs ($P=0.0023$) at C2-C3 level. The corresponding p-value for T2-T3 level measurements was 0.01. Normative data extracted from C2-C3 level showed that T2* WM/GM ratio, compared to other imaging metrics, had the smallest inter-subject CV of 3.3% for TD subjects and 4.3 % for SCIs. These values for upper thoracic measurements are 3.5% in TDs and 5.4 % in SCI subjects.

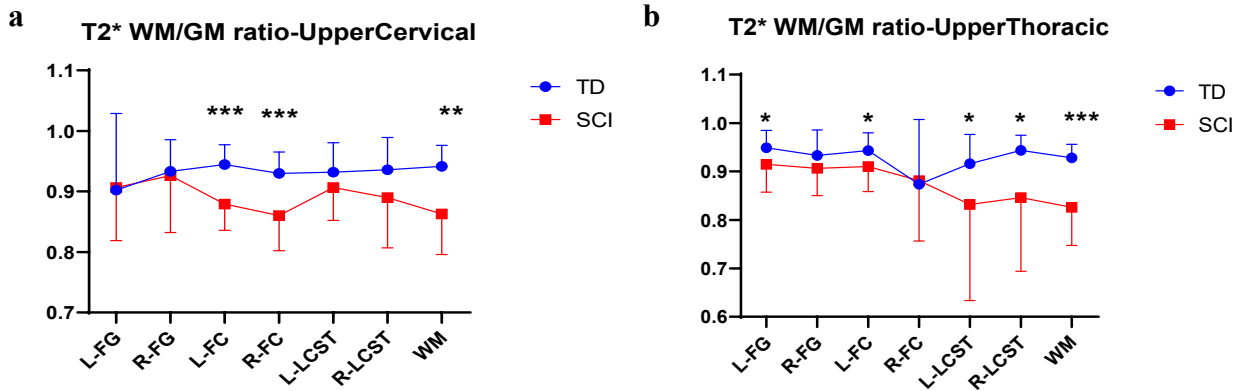


Figure 29: T2* WM/GM ratio averaged across all TD and SCI subjects for 7 WM tracts. The 7 WM tracts are: FG, fasciculus gracilis; FC, fasciculus cuneatus; LCST, lateral corticospinal tract; WM, white matter. L, left; R, right. The graphs show mean and standard deviation bars. Significant differences (decrease) were observed between our SCI patients and TD subjects when comparing the T2* WM/GM ratio at both upper cervical and upper thoracic levels (a & b). Fig (a) represents measurements at C2-C3 level. Fig (b) represents measurements at T2-T3 level.

(*p < 0.05; **p < 0.01; ***p < 0.001).

b) Macrostructural (Cross-Sectional Area) Changes:

The violin plots (figure-30) show the changes in the spinal cord cross-sectional area measurements. The results show that the total cross-sectional area (figure-30 a & b) of the spinal cord significantly decreased in SCI patients in both upper cervical (p=0.0002) and upper thoracic (P=0.0038) measurements when compared with TD subjects. Similar measurements for gray matter area at the corresponding levels resulted in a significant decrease in SCI patients (P_upperCervical=0.0035, P_UpperThoracic=0.0002). The WM

cross-sectional measurements showed a significant decrease in upper cervical (C2-C3 level) measurement in SCI (P=0.0023). The measurement at the upper thoracic level (T2-T3) also decreased in SCI when compared to TD but didn't show any significant changes (P>0.05). (figure-30 c & d), present WM-CSA changes in SCI and TD followed by (figure-30 e & f) illustrating the observed changes for the GM-CSA measurements.

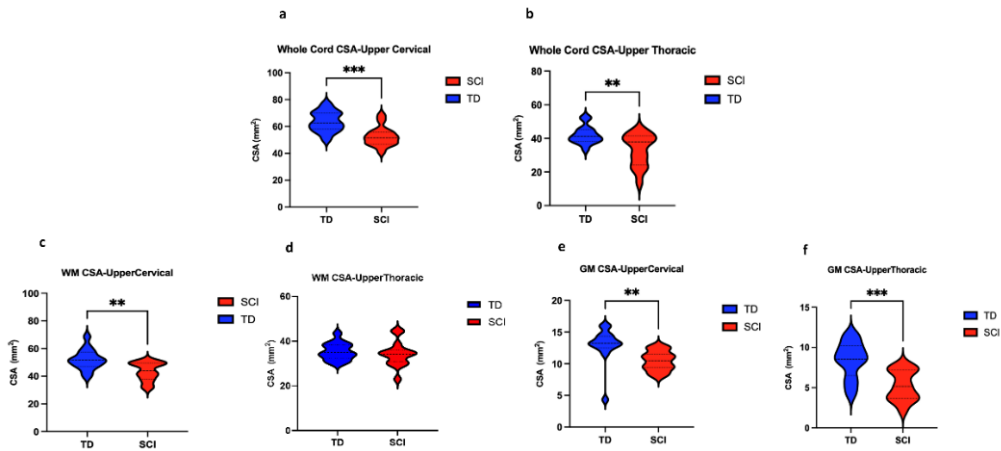


Figure 30: Violin plots of averaged cross-sectional area of the whole spinal cord (a,b), white matter(c,d), and gray matter(e,f) in all the 15 SCI and 15 TD subjects. Figs (a), (c) and (e) represent measurements at C2-C3 level and Figs (b), (d) and (f) are corresponding measurements at T2-T3 level. Smaller spinal cord, gray matter, and white matter area is observed in SCI when compared with TDs. The observed difference was significant in cord atrophy comparing SCI and TD Groups (*p < 0.05; **p < 0.01; ***p < 0.001).

c) Correlation of MR imaging metrics and clinical scores:

Significant correlation between imaging metrics was observed in SCI subjects using Pearson correlation analysis (figure-31). This relationship was also tested against ISNCSCI total motor and light touch sensory scores. In SCI patients at upper cervical measurements (figure-31a), there was a moderate correlation observed with T2* WM/GM ratio and WM-CSA ($r=0.55$, $P=0.035$). FA correlated fairly well with GM-CSA ($r=0.59$, $P=0.019$), WM-CSA ($r=0.58$, $P=0.023$) and Cord-CSA ($r=0.56$, $P=0.030$). A strong but negative correlation is also shown between RD and FA ($r=-0.87$, $P=3E^{-5}$), RD and WM-CSA ($r=-0.65$, $P=0.009$). MD followed the same pattern as RD and showed a strong correlation with WM-CSA ($r=-0.61$, $P=0.017$) and FA ($r=-0.65$, $P=0.008$). The total motor score showed moderate correlation with GM-CSA ($r=0.41$, $P>0.05$), WM-CSA ($r=0.52$, $P=0.049$), Cord-CSA ($r=0.40$, $P>0.05$), RD ($r=-0.41$, $P>0.05$) and MD ($r=-0.42$, $P>0.05$). Total light touch sensory scores revealed a positive correlation with AD ($r=0.43$, $P>0.05$) and total motor scores ($r=-0.41$, $P>0.05$). At the upper thoracic level (figure-31b), T2* WM/GM ratio showed a positive correlation with total light touch sensory score ($r=0.48$, $P=0.049$) and WM-CSA ($r=-0.49$, $P=0.05$). GM-CSA also showed a correlation with FA ($r=0.64$, $P=0.01$) and Cord-CSA ($r=0.77$, $P=0.001$). The total motor score had a moderate correlation with GM-CSA ($r=0.42$, $P>0.05$), Cord-CSA ($r=0.44$, $P>0.05$), RD ($r=-0.55$, $P=0.034$) and MD ($r=-0.56$, $P=0.031$).

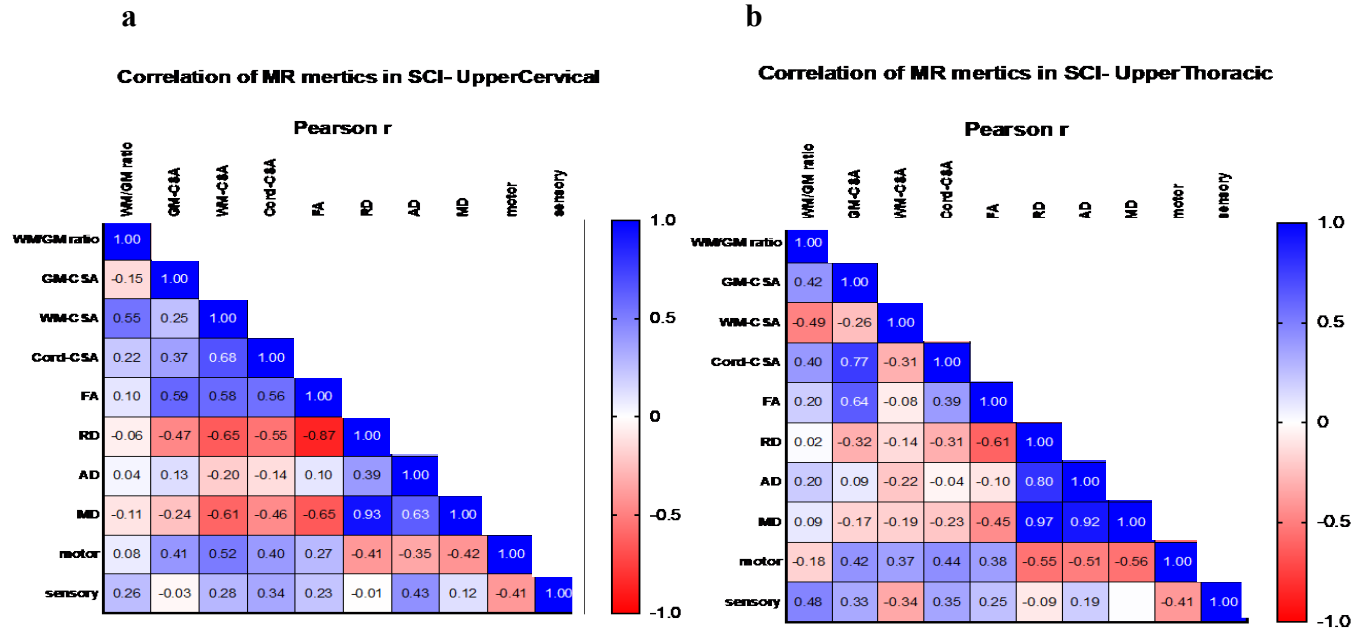


Figure 31: Correlation matrix for MR imaging metrics. Pearson correlation coefficients calculated between MR imaging metrics at C2–C3 (a) and T2-T3 (b) levels are color-coded to represent the degree of cross-correlation by using data from all 15 SCI subjects.

Discussion

In this study, we used multiple qMRI metrics to distinguish between the healthy (TD) and pediatric subjects with spinal cord injury. An in-house generated processing pipeline[59]was utilized to automatically extract WM tracts in the spinal cord of both populations. The DTI indices were quantified in the extracted WM tracts at two different levels of the spinal cord; upper-cervical (C2-C3) and upper-thoracic (T2-T3). The diffusion metrics, as well as 4 other qMRI metrics (WM-CSA, GM-CSA, whole cord CSA and T2* WM/GM ratio), were compared. The comparisons between these qMRI measures demonstrated significant results in terms of group differences and clinical correlations. Previous studies in animal models with SCI have shown changes above and

below the site of injury[131]:[132],[133] . Some diffusion studies have addressed the differences in the diffusion metrics in adults' healthy and SCI cervical spinal cord. These differences were studied in the WM regions that appeared normal on conventional MRI scans[134],[135],[136],[137]. To our knowledge, this is the first study that combines DTI metrics, T2* WM/GM intensity ratio, and CSA measurements in the injured pediatric spinal cord using an atlas-based approach.

DTI and atrophy (CSA) measurement findings:

Based on the distribution of the neurological level of injury (NLI) in our SCI population, the C2-C3 level measurements are considered caudal to the injury site for one SCI patient (with NLI at C1) and rostral to the injury site for 14 other patients. Whereas, T2-T3 level are the measurements caudal to the injury site for all the SCIs with cervical NLI and rostral to the injury site for the patients with thoracic and upper lumbar injuries. Considering the heterogeneous SCI population in our study (with various AIS grades), significant differences were still observed between controls and SCI patients for all the diffusion metrics (FA, MD, AD and RD), and all the CSA measurements.

At the microstructural level, previous studies in adults[134], [138] show that neurodegenerative changes in remote cord regions are evident in traumatic SCI (tSCI). The results of our study are in concordance with the findings of similar studies when comparing FA changes between the two populations[134][136][34]. The FA, which is a measure of white matter integrity in the spinal cord is decreased in our SCI population in all the extracted WM tracts. These changes are reflected in both C2-C3 and T2-T3 measurements and are important findings in studying pediatric SCI populations. Decreased FA values suggest anterograde (Wallerian) and retrograde degeneration of the

WM tracts[139]. The retrograde neural degeneration is resulting from axonal loss [140], demyelination [141],[142], and neural atrophy [143]. Secondary pathological processes, including ischemia, inflammation, and excitotoxic events, may also have occurred[144]. Moreover, the lower FA in SCI subjects could be the result of the reduced number of fibers due to injury, which causes increased diffusivity in the extracellular space[145]. In contrast to FA, MD, which is a measure of membrane density and is more sensitive to changes in cellularity, edema, and necrosis was increased in SCI subjects. The increased MD values in SCI subjects indicate disorganization within the fiber tracts[146]. This rise in MD with an accompanying fall in FA in tSCI has been observed in other studies as well [147],[148],[149]. In terms of directional diffusivities, both axial and radial diffusivity are increased in our SCI patients as opposed to TDs. These findings are supported by some other studies that used animal models of traumatic SCI and reported increased RD and AD remote from the lesion epicenter, at both ex vivo and in vivo experiments[148],[150]. Previous studies performed on animal models with demyelination and axonal damage indicated that RD and AD could predict axonal demyelination and degeneration, respectively[151],[152],[153]. In other works done by *Herrera et al*, in 2008[154] and *Sun et al*, in 2006[155], they reported dependencies between these two diffusivity metrics, resulting in the reduced specificity of these measures.

At the macrostructural level, the use of automated cross-sectional area measurement techniques enabled us for effective and fast characterization of spinal cord atrophy in SCI patients. In all cases of spinal cord injury, atrophy of the cord is expected following the degenerative processes that happen from sub-acute through chronic phases of injury,

resulting in a decrease in cross-sectional area of the cord. In previous adult studies, cervical cord atrophy remote from the injury site was reported in tSCI patients[138],[156] when compared with the healthy controls. In this work, an automated method from the spinal cord toolbox was used, to extract the cross-sectional area of the WM, GM and the whole cord. The method was successful in quantifying significant atrophy in all three regions of the cord in SCI patients when compared to TDs. As shown in the CSA measurements on violin plots, an increase in the variance of the measurements in SCI patients is also expected due to different injury locations and severities.

In summary, the observed macrostructural and microstructural changes in this study are consistent with axonal injury and degenerative processes that occur after the chronic injury in both retrograde and anterograde directions.

*T2*WI WM/GM ratio: A potential biomarker of WM injury:*

T2*-w imaging provides good image contrast between spinal cord GM and WM, allowing their segmentation and cross-sectional area measurement[157]. The idea of using T2* WM/GM intensity ratio stems from the presence of hyperintensity in T2*-w scans which is an indication of WM injury[129], [158], [159].

The hyperintensity itself reflects gliosis, demyelination or increased calcium and non-heme iron stored in ferritin[160]. T2*-w signal intensity, on the other hand, is not an absolute value and requires normalization for quantitative use. The GM signal intensity, as a reference, has been found[161] to produce more consistent results when compared to CSF due to signal variability of the CSF. In our work, T2* WM/GM intensity ratio was successful in discerning the SCI and TD populations in both upper cervical and upper

thoracic measurements of the cord. Additionally, we found a good correlation between the T2* WM/GM ratio and WM-CSA. However, the moderate correlation observed between T2* WM/GM ratio and other metrics of this study didn't show a clear pattern. This may be due to the fact that these findings are an indication of multiple pathologic processes occurring simultaneously. This requires an in-depth histological investigation to discover the underlying changes in the cord more accurately. Although not specific, its simplicity and sensitivity suggest that T2* WM/ GM ratio could be a helpful potential imaging biomarker[161].

Correlation Results:

We tested the correlation of all the metrics in this study with one another and with ISNCSCI total motor score, as well as the ISNCSCI total light touch sensory score for the WM regions. At C2-C3 level, we observed a strong correlation between T2* WM/GM ratio and WM-CSA. FA also correlated positively with all three CSA measurements of the WM, GM and the whole cord. These correlations may provide evidence of microstructural changes occurring during the atrophy process superior to the injury epicenter, which provides useful information in the examination of the injured spinal cord. The total motor score showed a good positive correlation with GM, WM and cord CSA and a moderate negative correlation with RD and MD. Essentially, the remote neurodegenerative changes within the cervical white and gray matter in SCI patients (i.e. atrophy) were associated with upper limb motor function and strength of upper limbs. Microstructural tract-specific changes (RD and MD) above the level of injury had a better correlation than FA and AD with ISNCSCI total motor score. This applies to both upper cervical and upper thoracic measurements in our study. *Freund, P. et al* and *Grabher, P.*

et al reported similar findings showing the association between clinical impairments and MRI-derived measures of the cord macrostructure and microstructure in the cervical spinal cord[156][162]. In addition to motor scores, total light touch sensory scores revealed a positive correlation with AD. At the upper thoracic measurements, T2* WM/GM ratio showed a strong correlation with total light touch sensory score and WM-CSA. Overall, these associations suggest that remote reorganizational changes, such as remodulation of intraspinal circuits,[163] play a role in the level of upper limb function in SCI subjects. It is important to note that these findings present a link between functional and microstructural changes in the cord by means of DTI and clinical measures. Therefore, the combination of these qMRI measurements could be a complementary biomarker to conventional MRI and could provide a more accurate assessment of the clinical state of the SCI patient.

These findings are particularly important given the inaccuracies of some of these measurements at the site of injury due to the presence of debris from the injury or the placement of metal hardware for stabilization after surgery.

Limitations of the Study

One of the limitations of the study is the lack of high SNR, DTI scans. This could be because of the intrinsic nature of diffusion imaging and longer scan times, which add motion artifacts due to breathing and swallowing, and cardiac motion. Studying the pediatric population with smaller cord size as opposed to adults also exacerbates the issue. This problem can be improved by using higher-field MRI scanners or high-performance gradients, and improved coils with reduced imaging times.

Another limitation is the observed intrasubject variability resulting from spatial misalignment during the registration of diffusion and structural scans. This warrants the need for preprocessing, normalization, and motion correction tools for diffusion data of the spinal cord. In addition, the age range of the subjects in our small sample size study was broad, so the age variation could impact the observed changes in DTI metrics[45]. This issue, along with the selected registration algorithms as well as the partial volume effects, plays a role in inter-subject variability. In addition to the limitations presented by DTI scans, T2*-w scans are also challenging to be used for the purpose of WM and GM segmentations. Since these scans are acquired axially with thicker slice selections, the contrast of the gray and white matter is usually low. The issue can be addressed by incorporating better registration techniques.

Conclusion

Multi-parametric qMRI provides sensitive markers of demyelination and degeneration, enabling longitudinal studies that target therapeutic strategies in pediatric patients with spinal cord injury. In this study, we showed the feasibility of utilizing advanced qMRI protocols that are sensitive to spinal cord pathology and have the potential to predict outcomes in children with SCI. In addition, we utilized tract-specific information to predict macrostructural and microstructural changes remote from the injury (specifically at the upper cervical level), which is significant given the inconsistencies with some of these measures at the isocenter of the injury. We showed that DTI, with its quantitative indices, is a valuable tool in the assessment of the cord injury in cases of spinal cord trauma when compared with a normal cord.

Atrophy measurements also showed the potential to become a powerful clinical tool in SCI. T2* WM/GM findings show potential to be used as a novel biomarker of spinal cord WM degeneration.

CHAPTER 7

CONCLUSION AND FUTURE WORK

In this research we demonstrated that multiparametric MRI is a powerful tool for studying the pediatric spinal cord at the microstructure and macrostructure levels. We presented the clinical utility of these biomarkers which specifically addresses a significant knowledge gap between clinicians and researchers. This is helpful in objectively determining the extent of severity and level of injury in pediatric SCIs. This work could also aid clinicians to potentially assess neurological recovery and evaluate treatment effectiveness in clinical trials.

Most importantly, we demonstrated the successful generation of, to date, the first, known structural template of the pediatric spinal cord. This is comprised of a generic template of the full spinal cord in T2-w contrast. The template is a major advancement in the neuroimaging field and specifically in the pediatric spinal cord imaging and enables the objective quantitative comparisons of imaging biomarkers between TD controls and children with spinal cord diseases. We were able to propose normative values for DTI metrics in addition to normative SCCSA values. This will increase the specificity and sensitivity of these noninvasive biomarkers for detecting lesions in children with SCI. In addition, these imaging biomarkers and template could be extended to other pediatric spinal cord diseases in the future.

As a part of future effort, more comprehensive work on analyzing larger cohorts of subjects is warranted. As of today, a workflow of collecting a group of 240 biological age and sex-matched typically developed subjects between 6-17 years is in place. We are extending the template creation pipeline proposed in this study to the new cohort and

aiming to develop a standardized spinal cord template using a high-resolution ($1\mu\text{m}^3$) isotropic T2-weighted scans in 240 biological age and sex matched TD subjects. This data collection also incorporates 50 subjects with chronic SCI (>12 months) that are identified as motor complete (AIS A and B). This will address one of the limitations of the current study which is a small sample size and heterogenous population of injured subjects with SCI (i.e. 15 SCIs used for this work). More specifically, the small SCI pool could also limit the comparison of specific injury sites to healthy control subjects. Despite the small cohort of subjects used in this study, we were able to show significant differences (p-values) when comparing the TD and SCI subjects.

In addition, the MRI sequence used in this research work could be modified to allow multishell acquisition which has the potential to fully characterize the diffusion. This will also help in extending the normative values to a range of diffusion imaging metrics such as diffusion kurtosis imaging (DKI) and Neurite orientation dispersion and density imaging (NODDI). The current diffusion-sensitized, multishell iFoV pulse sequence has enabled us to acquire high in-plane resolution diffusion images of the pediatric spinal cord. Using the new sequence, we can collect DTI, DKI and NODDI of the spinal cord in one acquisition in a reasonable clinically acceptable time. This requires additional optimization of the sequence used in this work to reduce physiological noise. The proposed modified sequence allows for a fast acquisition rate without compromising SNR. In addition, we will implement multiband imaging (simultaneous multi-slice, SMS) which will reduce the scan time and will allow us to perform cardiac gating. To acquire all the data outlined before, the total estimated scan time is 45 minutes. This will reduce

the total acquisition time from 60 minutes (total scan time in this study) to 45 minutes with the new proposed sequence, which is helpful considering intolerance in the scanner.

BIBLIOGRAPHY

- [1] “Spinal cord injury.” <https://www.who.int/news-room/fact-sheets/detail/spinal-cord-injury>.
- [2] G. W. J. Hawryluk, J. Rowland, B. K. Kwon, and M. G. Fehlings, “Protection and repair of the injured spinal cord: a review of completed, ongoing, and planned clinical trials for acute spinal cord injury,” *Neurosurg. Focus*, vol. 25, no. 5, p. E14, 2008.
- [3] J. W. Fawcett *et al.*, “Guidelines for the conduct of clinical trials for spinal cord injury as developed by the ICCP panel: spontaneous recovery after spinal cord injury and statistical power needed for therapeutic clinical trials,” *Spinal Cord*, vol. 45, no. 3, pp. 190–205, Mar. 2007.
- [4] J. W. Rowland, G. W. J. Hawryluk, B. Kwon, and M. G. Fehlings, “Current status of acute spinal cord injury pathophysiology and emerging therapies: promise on the horizon,” *Neurosurg. Focus*, vol. 25, no. 5, p. E2, 2008.
- [5] J. Cohen-Adad and C. Wheeler-Kingshott, *Quantitative MRI of the Spinal Cord*. Academic Press, 2014.
- [6] C. A. Oyinbo, “Secondary injury mechanisms in traumatic spinal cord injury: a nugget of this multiply cascade,” *Acta Neurobiol. Exp.*, vol. 71, no. 2, pp. 281–299, 2011.
- [7] R. J. Dumont, “Okonkwo Do, Verma S, Hurlbert RJ, Boulos PT, Ellegala DB, et al. Acute Spinal Cord Injury, Part I: Pathophysiologic Mechanisms,” *Clin. Neuropharmacol.*
- [8] L. H. Sekhon and M. G. Fehlings, “Epidemiology, demographics, and pathophysiology of acute spinal cord injury,” *Spine*, vol. 26, no. 24 Suppl, pp. S2–12, Dec. 2001.
- [9] A. M.-T. Choo, J. Liu, Z. Liu, M. Dvorak, W. Tetzlaff, and T. R. Oxland, “Modeling spinal cord contusion, dislocation, and distraction: Characterization of vertebral clamps, injury severities, and node of Ranvier deformations,” *J. Neurosci. Methods*, vol. 181, no. 1, pp. 6–17, Jun. 2009.
- [10] M. G. Fehlings *et al.*, “Perioperative and delayed complications associated with the surgical treatment of cervical spondylotic myelopathy based on 302 patients from the AOSpine North America Cervical Spondylotic Myelopathy Study,” *Journal of Neurosurgery: Spine*, vol. 16, no. 5, pp. 425–432, 2012. doi: 10.3171/2012.1.spine11467.
- [11] S. A. Figley, R. Khosravi, J. M. Legasto, Y.-F. Tseng, and M. G. Fehlings, “Characterization of Vascular Disruption and Blood–Spinal Cord Barrier Permeability following Traumatic Spinal Cord Injury,” *J. Neurotrauma*, vol. 31, no. 6, pp. 541–552, Mar. 2014.

- [12] M. G. Fehlings, A. R. Vaccaro, and M. Boakye, *Essentials of Spinal Cord Injury: Basic Research to Clinical Practice*. Thieme, 2012.
- [13] J. R. Wilson, D. W. Cadotte, and M. G. Fehlings, “Clinical predictors of neurological outcome, functional status, and survival after traumatic spinal cord injury: a systematic review,” *J. Neurosurg. Spine*, vol. 17, no. 1 Suppl, pp. 11–26, Sep. 2012.
- [14] J. W. McDonald and C. Sadowsky, “Spinal-cord injury,” *Lancet*, vol. 359, no. 9304, pp. 417–425, Feb. 2002.
- [15] C. H. Tator and M. G. Fehlings, “Review of the secondary injury theory of acute spinal cord trauma with emphasis on vascular mechanisms,” *J. Neurosurg.*, vol. 75, no. 1, pp. 15–26, Jul. 1991.
- [16] E. Tessitore, “M.G. Fehlings, A.R. Vaccaro, M. Boakye, S. Rossignol, J.F. Ditunno Jr, A.S. Burns (eds): Essentials of Spinal Cord Injury—Basic Research to Clinical Practice,” *Acta Neurochirurgica*, vol. 155, no. 5. pp. 949–950, 2013. doi: 10.1007/s00701-013-1654-8.
- [17] R. E. von Leden, R. E. von Leden, Y. J. Yauger, G. Khayrullina, and K. R. Byrnes, “Central Nervous System Injury and Nicotinamide Adenine Dinucleotide Phosphate Oxidase: Oxidative Stress and Therapeutic Targets,” *Journal of Neurotrauma*, vol. 34, no. 4. pp. 755–764, 2017. doi: 10.1089/neu.2016.4486.
- [18] A. P. Tran, P. M. Warren, and J. Silver, “The Biology of Regeneration Failure and Success After Spinal Cord Injury,” *Physiol. Rev.*, vol. 98, no. 2, pp. 881–917, Apr. 2018.
- [19] S. M. Dyck and S. Karimi-Abdolrezaee, “Chondroitin sulfate proteoglycans: Key modulators in the developing and pathologic central nervous system,” *Exp. Neurol.*, vol. 269, pp. 169–187, Jul. 2015.
- [20] A. Alizadeh, S. M. Dyck, and S. Karimi-Abdolrezaee, “Myelin damage and repair in pathologic CNS: challenges and prospects,” *Front. Mol. Neurosci.*, vol. 8, p. 35, Jul. 2015.
- [21] R. L. Waters, R. H. Adkins, J. S. Yakura, and I. Sie, “Motor and sensory recovery following incomplete tetraplegia,” *Arch. Phys. Med. Rehabil.*, vol. 75, no. 3, pp. 306–311, Mar. 1994.
- [22] P. J. Brown, R. J. Marino, G. J. Herbison, and J. F. Ditunno Jr, “The 72-hour examination as a predictor of recovery in motor complete quadriplegia,” *Arch. Phys. Med. Rehabil.*, vol. 72, no. 8, pp. 546–548, Jul. 1991.
- [23] K. Fouad, A. Krajacic, and W. Tetzlaff, “Spinal cord injury and plasticity: opportunities and challenges,” *Brain Res. Bull.*, vol. 84, no. 4–5, pp. 337–342, Mar. 2011.

- [24] F. Bloch, "Nuclear Induction," *Phys. Rev.*, vol. 70, no. 7–8, pp. 460–474, Oct. 1946.
- [25] K. Edler and D. Hoult, "Spherical harmonic inductive detection coils for dynamic pre-emphasis," *Magn. Reson. Med.*, vol. 60, no. 2, pp. 277–287, Aug. 2008.
- [26] A. Einstein, "On the movement of small particles suspended in a stationary liquid demanded by the molecular-kinetic theory of heat (English translation, 1956)," *Investigations on the theory of the Brownian movement*, 1905, Accessed: Mar. 17, 2023. [Online]. Available: <https://cir.nii.ac.jp/crid/1571698600330726912>
- [27] A. Fick, "V. On liquid diffusion," *The London, Edinburgh, and Dublin Philosophical Magazine and Journal of Science*, vol. 10, no. 63, pp. 30–39, Jul. 1855.
- [28] D. Le Bihan, E. Breton, D. Lallemand, P. Grenier, E. Cabanis, and M. Laval-Jeantet, "MR imaging of intravoxel incoherent motions: application to diffusion and perfusion in neurologic disorders," *Radiology*, vol. 161, no. 2, pp. 401–407, Nov. 1986.
- [29] S. Mori and J.-D. Tournier, Eds., "Chapter 4 - Principle of Diffusion Tensor Imaging," in *Introduction to Diffusion Tensor Imaging (Second Edition)*, San Diego: Academic Press, 2014, pp. 27–32.
- [30] P. J. Basser, J. Mattiello, and D. LeBihan, "MR diffusion tensor spectroscopy and imaging," *Biophys. J.*, vol. 66, no. 1, pp. 259–267, Jan. 1994.
- [31] E. O. Stejskal and J. E. Tanner, "Spin Diffusion Measurements: Spin Echoes in the Presence of a Time-Dependent Field Gradient," *J. Chem. Phys.*, vol. 42, no. 1, pp. 288–292, Jan. 1965.
- [32] G. C. DeLuca *et al.*, "Casting light on multiple sclerosis heterogeneity: the role of HLA-DRB1 on spinal cord pathology," *Brain*, vol. 136, no. 4, pp. 1025–1034, 2013. doi: 10.1093/brain/awt031.
- [33] M. M. Poplawski *et al.*, "Application of Diffusion Tensor Imaging in Forecasting Neurological Injury and Recovery after Human Cervical Spinal Cord Injury," *J. Neurotrauma*, vol. 36, no. 21, pp. 3051–3061, Nov. 2019.
- [34] G. David *et al.*, "Traumatic and nontraumatic spinal cord injury: pathological insights from neuroimaging," *Nat. Rev. Neurol.*, vol. 15, no. 12, pp. 718–731, Dec. 2019.
- [35] J. Cohen-Adad, W. Zhao, B. Keil, and E. M. Ratai, "7-T MRI of the spinal cord can detect lateral corticospinal tract abnormality in amyotrophic lateral sclerosis," *Muscle &*, 2013, [Online]. Available: https://onlinelibrary.wiley.com/doi/abs/10.1002/mus.23720?casa_token=7o-Q2eJN_hEAAAAA:8LpIahWlbp-NDI_si0QgkJNwlobABp4zYCEXekBWlhNef8-KwRNng8driAxNjdJgH04JHGd0jnpUnp8

- [36] P. W. Stroman *et al.*, “The current state-of-the-art of spinal cord imaging: Methods,” *NeuroImage*, vol. 84, pp. 1070–1081, 2014. doi: 10.1016/j.neuroimage.2013.04.124.
- [37] P. Summers, A. Bauleo, S. Favilla, F. Cretti, F. Lui, and C. Porro, “Gross structure of magnetic field inhomogeneity in the human cervical spinal cord,” in *Proc 22nd Scientific Meeting of the ISMRM, Milan, Italy*, 2014, p. 1721.
- [38] T. Verma and J. Cohen-Adad, “Effect of respiration on the B0 field in the human spinal cord at 3T,” *Magn. Reson. Med.*, vol. 72, no. 6, pp. 1629–1636, Dec. 2014.
- [39] P. Summers, P. Staempfli, T. Jaermann, S. Kwiecinski, and S. Kollias, “A preliminary study of the effects of trigger timing on diffusion tensor imaging of the human spinal cord,” *AJNR Am. J. Neuroradiol.*, vol. 27, no. 9, pp. 1952–1961, Oct. 2006.
- [40] C. A. Wheeler-Kingshott *et al.*, “The current state-of-the-art of spinal cord imaging: Applications,” *NeuroImage*, vol. 84, pp. 1082–1093, 2014. doi: 10.1016/j.neuroimage.2013.07.014.
- [41] P. J. Basser, “Inferring microstructural features and the physiological state of tissues from diffusion-weighted images,” *NMR Biomed.*, vol. 8, no. 7–8, pp. 333–344, Nov. 1995.
- [42] N. Barakat *et al.*, “Diffusion tensor imaging of the normal pediatric spinal cord using an inner field of view echo-planar imaging sequence,” *AJNR Am. J. Neuroradiol.*, vol. 33, no. 6, pp. 1127–1133, Jun. 2012.
- [43] C. Rossi *et al.*, “Water diffusion anisotropy in white and gray matter of the human spinal cord,” *J. Magn. Reson. Imaging*, vol. 27, no. 3, pp. 476–482, Mar. 2008.
- [44] C. A. M. Wheeler-Kingshott *et al.*, “Investigating cervical spinal cord structure using axial diffusion tensor imaging,” *Neuroimage*, vol. 16, no. 1, pp. 93–102, May 2002.
- [45] S. Saksena *et al.*, “Diffusion Tensor Imaging of the Normal Cervical and Thoracic Pediatric Spinal Cord,” *AJNR Am. J. Neuroradiol.*, vol. 37, no. 11, pp. 2150–2157, Nov. 2016.
- [46] B. B. Reynolds *et al.*, “Quantification of DTI in the Pediatric Spinal Cord: Application to Clinical Evaluation in a Healthy Patient Population,” *American Journal of Neuroradiology*, vol. 40, no. 7, pp. 1236–1241, 2019. doi: 10.3174/ajnr.a6104.
- [47] S. Tuček, “The Central Nervous System: Structure and Function by Per Brodal. Oxford University Press, New York, 1992, ISBN 0-19-505518-7, xi 464 pp., \$39.95 (cloth),” *Journal of Neurochemistry*, vol. 63, no. 1, pp. 390–390, 2002. doi: 10.1046/j.1471-4159.1994.63010390.x.

- [48] M. J. Mulcahey *et al.*, “Diffusion tensor imaging in pediatric spinal cord injury: preliminary examination of reliability and clinical correlation,” *Spine*, vol. 37, no. 13, pp. E797–803, Jun. 2012.
- [49] M. J. Mulcahey *et al.*, “Diagnostic accuracy of diffusion tensor imaging for pediatric cervical spinal cord injury,” *Spinal Cord*, vol. 51, no. 7, pp. 532–537, Jul. 2013.
- [50] P. W. Stroman, C. R. Figley, and C. M. Cahill, “Spatial normalization, bulk motion correction and coregistration for functional magnetic resonance imaging of the human cervical spinal cord and brainstem,” *Magn. Reson. Imaging*, vol. 26, no. 6, pp. 809–814, Jul. 2008.
- [51] F. Eippert, J. Finsterbusch, U. Bingel, and C. Büchel, “Direct evidence for spinal cord involvement in placebo analgesia,” *Science*, vol. 326, no. 5951, p. 404, Oct. 2009.
- [52] P. Valsasina, M. A. Horsfield, M. A. Rocca, M. Absinta, G. Comi, and M. Filippi, “Spatial normalization and regional assessment of cord atrophy: voxel-based analysis of cervical cord 3D T1-weighted images,” *AJNR Am. J. Neuroradiol.*, vol. 33, no. 11, pp. 2195–2200, Dec. 2012.
- [53] M.-M. El Mendili *et al.*, “Fast and accurate semi-automated segmentation method of spinal cord MR images at 3T applied to the construction of a cervical spinal cord template,” *PLoS One*, vol. 10, no. 3, p. e0122224, Mar. 2015.
- [54] M. Taso *et al.*, “A reliable spatially normalized template of the human spinal cord—Applications to automated white matter/gray matter segmentation and tensor-based morphometry (TBM) mapping of gray matter alterations occurring with age,” *Neuroimage*, vol. 117, pp. 20–28, Aug. 2015.
- [55] V. S. Fonov *et al.*, “Framework for integrated MRI average of the spinal cord white and gray matter: the MNI-Poly-AMU template,” *Neuroimage*, vol. 102 Pt 2, pp. 817–827, Nov. 2014.
- [56] B. De Leener *et al.*, “SCT: Spinal Cord Toolbox, an open-source software for processing spinal cord MRI data,” *Neuroimage*, vol. 145, no. Pt A, pp. 24–43, Jan. 2017.
- [57] B. De Leener, V. S. Fonov, D. L. Collins, V. Callot, N. Stikov, and J. Cohen-Adad, “PAM50: Unbiased multimodal template of the brainstem and spinal cord aligned with the ICBM152 space,” *Neuroimage*, vol. 165, pp. 170–179, Jan. 2018.
- [58] S. Shahrampour *et al.*, “Development of a Standardized Normative Pediatric Spinal Cord structural template: Demonstration of an automatic estimation of Spinal Cord Cross Sectional Area measurements (SCCSA),” in *Proc. Intl. Soc. Mag. Reson. Med*, 2019, vol. 27, p. 2624.

- [59] S. Shahrapour *et al.*, “Atlas-Based Quantification of DTI Measures in a Typically Developing Pediatric Spinal Cord,” *AJNR Am. J. Neuroradiol.*, vol. 42, no. 9, pp. 1727–1734, Sep. 2021.
- [60] C. Blanc, S. Shahrapour, F. B. Mohamed, and B. de Leener, “Combining PropSeg and a convolutional neural network for automatic spinal cord segmentation in pediatric populations and patients with spinal cord injury,” *Int. J. Imaging Syst. Technol.*, vol. n/a, no. n/a, Feb. 2023, doi: 10.1002/ima.22859.
- [61] D. M. Middleton *et al.*, “Correlations of diffusion tensor imaging and clinical measures with spinal cord cross-sectional area measurements in pediatric spinal cord injury patients,” *J. Spinal Cord Med.*, pp. 1–8, Dec. 2021.
- [62] S. Saksena *et al.*, “Diffusion Tensor Imaging Assessment of Regional White Matter Changes in the Cervical and Thoracic Spinal Cord in Pediatric Subjects,” *J. Neurotrauma*, vol. 36, no. 6, pp. 853–861, Mar. 2019.
- [63] A. R. Martin *et al.*, “Correction: Monitoring for myelopathic progression with multiparametric quantitative MRI,” *PLoS One*, vol. 13, no. 9, p. e0204082, Sep. 2018.
- [64] J. Cohen-Adad, “Microstructural imaging in the spinal cord and validation strategies,” *Neuroimage*, vol. 182, pp. 169–183, Nov. 2018.
- [65] “Welcome to NeuroPoly — NeuroPoly Lab.” <https://neuro.polymtl.ca/>. (accessed Mar. 30, 2023).
- [66] J. Finsterbusch, “Improving the performance of diffusion-weighted inner field-of-view echo-planar imaging based on 2D-selective radiofrequency excitations by tilting the excitation plane,” *J. Magn. Reson. Imaging*, vol. 35, no. 4, pp. 984–992, Apr. 2012.
- [67] “Welcome to NeuroPoly — NeuroPoly Lab.” <https://neuro.polymtl.ca/>. (accessed Mar. 30, 2023).
- [68] C. Gros *et al.*, “Automatic spinal cord localization, robust to MRI contrasts using global curve optimization,” *Med. Image Anal.*, vol. 44, pp. 215–227, Feb. 2018.
- [69] B. De Leener, S. Kadoury, and J. Cohen-Adad, “Robust, accurate and fast automatic segmentation of the spinal cord,” *Neuroimage*, vol. 98, pp. 528–536, Sep. 2014.
- [70] E. Ullmann, J. F. Pelletier Paquette, W. E. Thong, and J. Cohen-Adad, “Automatic labeling of vertebral levels using a robust template-based approach,” *Int. J. Biomed. Imaging*, vol. 2014, p. 719520, Jul. 2014.
- [71] B. De Leener *et al.*, “Topologically preserving straightening of spinal cord MRI,” *J. Magn. Reson. Imaging*, vol. 46, no. 4, pp. 1209–1219, Oct. 2017.

- [72] B. De Leener, J. Cohen-Adad, and S. Kadoury, "Automatic Segmentation of the Spinal Cord and Spinal Canal Coupled With Vertebral Labeling," *IEEE Trans. Med. Imaging*, vol. 34, no. 8, pp. 1705–1718, Aug. 2015.
- [73] A. R. Martin *et al.*, "Monitoring for myelopathic progression with multiparametric quantitative MRI," *PLoS One*, vol. 13, no. 4, p. e0195733, Apr. 2018.
- [74] D. L. Collins, C. J. Holmes, T. M. Peters, and A. C. Evans, "Automatic 3-D model-based neuroanatomical segmentation," *Hum. Brain Mapp.*, vol. 3, no. 3, pp. 190–208, 1995.
- [75] S. Lévy, M. Benhamou, C. Naaman, P. Rainville, V. Callot, and J. Cohen-Adad, "White matter atlas of the human spinal cord with estimation of partial volume effect," *Neuroimage*, vol. 119, pp. 262–271, Oct. 2015.
- [76] Y. Assaf, T. Blumenfeld-Katzir, Y. Yovel, and P. J. Basser, "AxCaliber: a method for measuring axon diameter distribution from diffusion MRI," *Magn. Reson. Med.*, vol. 59, no. 6, pp. 1347–1354, Jun. 2008.
- [77] A. Saliiani, B. Perraud, T. Duval, N. Stikov, S. Rossignol, and J. Cohen-Adad, "Axon and Myelin Morphology in Animal and Human Spinal Cord," *Front. Neuroanat.*, vol. 11, p. 129, Dec. 2017.
- [78] C. Mb, "Gross anatomy and internal structure," *Core Text of Neuroanatomy.*, pp. 57–86, 1991.
- [79] D. Chard and D. Miller, "Is multiple sclerosis a generalized disease of the central nervous system? An MRI perspective," *Curr. Opin. Neurol.*, vol. 22, no. 3, pp. 214–218, Jun. 2009.
- [80] H. Krum, W. J. Louis, D. J. Brown, and L. G. Howes, "Pressor dose responses and baroreflex sensitivity in quadriplegic spinal cord injury patients," *J. Hypertens.*, vol. 10, no. 3, pp. 245–250, Mar. 1992.
- [81] D. Le Bihan *et al.*, "Diffusion tensor imaging: concepts and applications," *J. Magn. Reson. Imaging*, vol. 13, no. 4, pp. 534–546, Apr. 2001.
- [82] B. M. Ellingson, J. L. Ulmer, S. N. Kurpad, and B. D. Schmit, "Diffusion tensor MR imaging of the neurologically intact human spinal cord," *AJNR Am. J. Neuroradiol.*, vol. 29, no. 7, pp. 1279–1284, Aug. 2008.
- [83] B. M. Ellingson, J. L. Ulmer, S. N. Kurpad, and B. D. Schmit, "Diffusion tensor MR imaging in chronic spinal cord injury," *AJNR Am. J. Neuroradiol.*, vol. 29, no. 10, pp. 1976–1982, Nov. 2008.

- [84] H. Mamata, U. De Girolami, W. S. Hoge, F. A. Jolesz, and S. E. Maier, “Collateral nerve fibers in human spinal cord: visualization with magnetic resonance diffusion tensor imaging,” *Neuroimage*, vol. 31, no. 1, pp. 24–30, May 2006.
- [85] H. Liu *et al.*, “Myelin Water Fraction and Intra/Extracellular Water Geometric Mean T2 Normative Atlases for the Cervical Spinal Cord from 3T MRI,” *J. Neuroimaging*, vol. 30, no. 1, pp. 50–57, Jan. 2020.
- [86] M. Hori *et al.*, “Application of Quantitative Microstructural MR Imaging with Atlas-based Analysis for the Spinal Cord in Cervical Spondylotic Myelopathy,” *Sci. Rep.*, vol. 8, no. 1, p. 5213, Mar. 2018.
- [87] S. Standring and N. R. Borley, “Gray’s anatomy: the anatomical basis of clinical practice. 2008 40th ed., anniversary ed.[Edinburgh]: Churchill Livingstone.” Elsevier.
- [88] L. Fradet, P.-J. Arnoux, J.-P. Ranjeva, Y. Petit, and V. Callot, “Morphometrics of the entire human spinal cord and spinal canal measured from in vivo high-resolution anatomical magnetic resonance imaging,” *Spine*, vol. 39, no. 4, pp. E262–9, Feb. 2014.
- [89] N. J. Tustison and B. B. Avants, “Explicit B-spline regularization in diffeomorphic image registration,” *Front. Neuroinform.*, vol. 7, p. 39, Dec. 2013.
- [90] P. G. Lindberg, A. Feydy, and M. A. Maier, “White matter organization in cervical spinal cord relates differently to age and control of grip force in healthy subjects,” *J. Neurosci.*, vol. 30, no. 11, pp. 4102–4109, Mar. 2010.
- [91] J. Cohen-Adad, M. Descoteaux, S. Rossignol, R. D. Hoge, R. Deriche, and H. Benali, “Detection of multiple pathways in the spinal cord using q-ball imaging,” *Neuroimage*, vol. 42, no. 2, pp. 739–749, Aug. 2008.
- [92] P. A. Narayana, R. J. Grill, T. Chacko, and R. Vang, “Endogenous recovery of injured spinal cord: longitudinal in vivo magnetic resonance imaging,” *J. Neurosci. Res.*, vol. 78, no. 5, pp. 749–759, Dec. 2004.
- [93] M. Onu *et al.*, “Human cervical spinal cord funiculi: investigation with magnetic resonance diffusion tensor imaging,” *J. Magn. Reson. Imaging*, vol. 31, no. 4, pp. 829–837, Apr. 2010.
- [94] S. By, J. Xu, B. A. Box, F. R. Bagnato, and S. A. Smith, “Application and evaluation of NODDI in the cervical spinal cord of multiple sclerosis patients,” *NeuroImage: Clinical*, vol. 15, pp. 333–342, Jan. 2017.
- [95] S. Madi, K. M. Hasan, and P. A. Narayana, “Diffusion tensor imaging of in vivo and excised rat spinal cord at 7 T with an icosahedral encoding scheme,” *Magn. Reson. Med.*, vol. 53, no. 1, pp. 118–125, Jan. 2005.

- [96] B. M. Ellingson, S. N. Kurpad, S.-J. Li, and B. D. Schmit, "In vivo diffusion tensor imaging of the rat spinal cord at 9.4T," *J. Magn. Reson. Imaging*, vol. 27, no. 3, pp. 634–642, Mar. 2008.
- [97] J. Gullapalli, J. Krejza, and E. D. Schwartz, "In vivo DTI evaluation of white matter tracts in rat spinal cord," *J. Magn. Reson. Imaging*, vol. 24, no. 1, pp. 231–234, Jul. 2006.
- [98] F. Prados *et al.*, "Fully automated grey and white matter spinal cord segmentation," *Sci. Rep.*, vol. 6, p. 36151, Oct. 2016.
- [99] N. A. Losseff *et al.*, "Spinal cord atrophy and disability in multiple sclerosis. A new reproducible and sensitive MRI method with potential to monitor disease progression," *Brain*, vol. 119 (Pt 3), pp. 701–708, Jun. 1996.
- [100] V. L. Stevenson *et al.*, "Spinal cord atrophy and disability in MS: a longitudinal study," *Neurology*, vol. 51, no. 1, pp. 234–238, Jul. 1998.
- [101] V. Engelbrecht, A. Scherer, M. Rassek, H. J. Witsack, and U. Mödder, "Diffusion-weighted MR imaging in the brain in children: findings in the normal brain and in the brain with white matter diseases," *Radiology*, vol. 222, no. 2, pp. 410–418, Feb. 2002.
- [102] U. Löbel, J. Sedlacik, D. Güllmar, W. A. Kaiser, J. R. Reichenbach, and H.-J. Mentzel, "Diffusion tensor imaging: the normal evolution of ADC, RA, FA, and eigenvalues studied in multiple anatomical regions of the brain," *Neuroradiology*, vol. 51, no. 4, pp. 253–263, Apr. 2009.
- [103] A. V. Faria *et al.*, "Atlas-based analysis of neurodevelopment from infancy to adulthood using diffusion tensor imaging and applications for automated abnormality detection," *Neuroimage*, vol. 52, no. 2, pp. 415–428, Aug. 2010.
- [104] S. Singhi *et al.*, "Diffusion tensor imaging of the maturing paediatric cervical spinal cord: from the neonate to the young adult," *J. Neuroradiol.*, vol. 39, no. 3, pp. 142–148, Jul. 2012.
- [105] M. Alizadeh *et al.*, "Age related diffusion and tractography changes in typically developing pediatric cervical and thoracic spinal cord," *Neuroimage Clin*, vol. 18, pp. 784–792, Mar. 2018.
- [106] I. Izbudak, N. Dumrongpisutikul, and C. B. Thompson, "Diffusion tensor scalars vary with age and across spinal levels in children," *J. Neurol. Neurosci.*, vol. 06, no. 04, 2015, doi: 10.21767/2171-6625.100047.
- [107] D. Prayer and L. Prayer, "Diffusion-weighted magnetic resonance imaging of cerebral white matter development," *Eur. J. Radiol.*, vol. 45, no. 3, pp. 235–243, Mar. 2003.

- [108] R. L. Friede, "Control of myelin formation by axon caliber (with a model of the control mechanism)," *J. Comp. Neurol.*, vol. 144, no. 2, pp. 233–252, Feb. 1972.
- [109] B. A. Brody, H. C. Kinney, A. S. Kloman, and F. H. Gilles, "Sequence of central nervous system myelination in human infancy. I. An autopsy study of myelination," *J. Neuropathol. Exp. Neurol.*, vol. 46, no. 3, pp. 283–301, May 1987.
- [110] H. C. Kinney, B. A. Brody, A. S. Kloman, and F. H. Gilles, "Sequence of central nervous system myelination in human infancy. II. Patterns of myelination in autopsied infants," *J. Neuropathol. Exp. Neurol.*, vol. 47, no. 3, pp. 217–234, May 1988.
- [111] G. Coll, E. de Schlichting, L. Sakka, J.-M. Garcier, H. Peyre, and J.-J. Lemaire, "Assessment of Maturational Changes in White Matter Anisotropy and Volume in Children: A DTI Study," *AJNR Am. J. Neuroradiol.*, vol. 41, no. 9, pp. 1726–1732, Sep. 2020.
- [112] T. Duval *et al.*, "In vivo mapping of human spinal cord microstructure at 300mT/m," *Neuroimage*, vol. 118, pp. 494–507, Sep. 2015.
- [113] H. Johansen-Berg and T. E. J. Behrens, *Diffusion MRI: From Quantitative Measurement to In vivo Neuroanatomy*. Academic Press, 2013.
- [114] A. Ohnishi, P. C. O'Brien, H. Okazaki, and P. J. Dyck, "Morphometry of myelinated fibers of fasciculus gracilis of man," *J. Neurol. Sci.*, vol. 27, no. 2, pp. 163–172, Feb. 1976.
- [115] S. Terao, G. Sobue, Y. Hashizume, N. Shimada, and T. Mitsuma, "Age-related changes of the myelinated fibers in the human corticospinal tract: a quantitative analysis," *Acta Neuropathol.*, vol. 88, no. 2, pp. 137–142, 1994.
- [116] R. Nieuwenhuys, J. Voogd, and C. van Huijzen, *The Human Central Nervous System: A Synopsis and Atlas*. Springer Science & Business Media, 2007.
- [117] C. S. Ahuja *et al.*, "Traumatic spinal cord injury," *Nature Reviews Disease Primers*, vol. 3, no. 1. 2017. doi: 10.1038/nrdp.2017.18.
- [118] R. N. Lemon and J. Griffiths, "Comparing the function of the corticospinal system in different species: organizational differences for motor specialization?," *Muscle Nerve*, vol. 32, no. 3, pp. 261–279, Sep. 2005.
- [119] M. L. Starkey and M. E. Schwab, "Anti-Nogo-A and training: can one plus one equal three?," *Exp. Neurol.*, vol. 235, no. 1, pp. 53–61, May 2012.
- [120] S. K. Karadimas, G. Gatzounis, and M. G. Fehlings, "Pathobiology of cervical spondylotic myelopathy," *Eur. Spine J.*, vol. 24 Suppl 2, pp. 132–138, Apr. 2015.

- [121] W. R. Yu, T. Liu, T.-R. Kiehl, and M. G. Fehlings, “Human neuropathological and animal model evidence supporting a role for Fas-mediated apoptosis and inflammation in cervical spondylotic myelopathy,” *Brain*, vol. 134, no. Pt 5, pp. 1277–1292, May 2011.
- [122] H. H. Bohlman and S. E. Emery, “The pathophysiology of cervical spondylosis and myelopathy,” *Spine*, vol. 13, no. 7, pp. 843–846, Jul. 1988.
- [123] M. G. Fehlings and G. Skaf, “A Review of the Pathophysiology of Cervical Spondylotic Myelopathy With Insights for Potential Novel Mechanisms Drawn From Traumatic Spinal Cord Injury,” *Spine*, vol. 23, no. 24, pp. 2730–2736, 1998. doi: 10.1097/00007632-199812150-00012.
- [124] F. Akter and M. Kotter, “Pathobiology of Degenerative Cervical Myelopathy,” *Neurosurg. Clin. N. Am.*, vol. 29, no. 1, pp. 13–19, Jan. 2018.
- [125] S. C. Kirshblum *et al.*, “International standards for neurological classification of spinal cord injury (Revised 2011),” *The Journal of Spinal Cord Medicine*, vol. 34, no. 6, pp. 535–546, 2011. doi: 10.1179/204577211x13207446293695.
- [126] M. Alizadeh *et al.*, “Reduced Field of View Diffusion Tensor Imaging and Fiber Tractography of the Pediatric Cervical and Thoracic Spinal Cord Injury,” *J. Neurotrauma*, vol. 35, no. 3, pp. 452–460, Feb. 2018.
- [127] L. Krisa *et al.*, “Clinical Utility of Diffusion Tensor Imaging as a Biomarker to Identify Microstructural Changes in Pediatric Spinal Cord Injury,” *Top. Spinal Cord Inj. Rehabil.*, vol. 28, no. 2, pp. 1–12, Apr. 2022.
- [128] M. C. Yiannakas *et al.*, “Feasibility of grey matter and white matter segmentation of the upper cervical cord in vivo: a pilot study with application to magnetisation transfer measurements,” *Neuroimage*, vol. 63, no. 3, pp. 1054–1059, Nov. 2012.
- [129] J. Cohen-Adad, B. Buchbinder, and A. L. Oaklander, “Cervical spinal cord injection of epidural corticosteroids: comprehensive longitudinal study including multiparametric magnetic resonance imaging,” *Pain*, vol. 153, no. 11, pp. 2292–2299, Nov. 2012.
- [130] R. B. Kamble, N. K. Venkataramana, A. L. Naik, and S. V. Rao, “Diffusion tensor imaging in spinal cord injury,” *Indian J. Radiol. Imaging*, vol. 21, no. 3, pp. 221–224, Jul. 2011.
- [131] J. Cohen-Adad, H. Leblond, H. Delivet-Mongrain, M. Martinez, H. Benali, and S. Rossignol, “Wallerian degeneration after spinal cord lesions in cats detected with diffusion tensor imaging,” *Neuroimage*, vol. 57, no. 3, pp. 1068–1076, Aug. 2011.

- [132] F. H. Brennan, G. J. Cowin, N. D. Kurniawan, and M. J. Ruitenberg, “Longitudinal assessment of white matter pathology in the injured mouse spinal cord through ultra-high field (16.4 T) in vivo diffusion tensor imaging,” *Neuroimage*, vol. 82, pp. 574–585, Nov. 2013.
- [133] L. M. Sundberg, J. J. Herrera, and P. A. Narayana, “In vivo longitudinal MRI and behavioral studies in experimental spinal cord injury,” *J. Neurotrauma*, vol. 27, no. 10, pp. 1753–1767, Oct. 2010.
- [134] J. Cohen-Adad *et al.*, “Demyelination and degeneration in the injured human spinal cord detected with diffusion and magnetization transfer MRI,” *Neuroimage*, vol. 55, no. 3, pp. 1024–1033, Apr. 2011.
- [135] J. A. Petersen *et al.*, “Chronic cervical spinal cord injury: DTI correlates with clinical and electrophysiological measures,” *J. Neurotrauma*, vol. 29, no. 8, pp. 1556–1566, May 2012.
- [136] E. Koskinen *et al.*, “Assessing the state of chronic spinal cord injury using diffusion tensor imaging,” *J. Neurotrauma*, vol. 30, no. 18, pp. 1587–1595, Sep. 2013.
- [137] S.-Y. Kim *et al.*, “Correlation of diffusion tensor imaging and phase-contrast MR with clinical parameters of cervical spinal cord injuries,” *Spinal Cord*, vol. 53, no. 8, pp. 608–614, Aug. 2015.
- [138] E. Huber, G. David, A. J. Thompson, N. Weiskopf, S. Mohammadi, and P. Freund, “Dorsal and ventral horn atrophy is associated with clinical outcome after spinal cord injury,” *Neurology*, vol. 90, no. 17, pp. e1510–e1522, Apr. 2018.
- [139] B. Beirowski *et al.*, “The progressive nature of Wallerian degeneration in wild-type and slow Wallerian degeneration (Wlds) nerves,” *BMC Neurosci.*, vol. 6, p. 6, Feb. 2005.
- [140] M. J. Crowe, J. C. Bresnahan, S. L. Shuman, J. N. Masters, and M. S. Beattie, “Apoptosis and delayed degeneration after spinal cord injury in rats and monkeys,” *Nat. Med.*, vol. 3, no. 1, pp. 73–76, Jan. 1997.
- [141] A. Buss *et al.*, “Gradual loss of myelin and formation of an astrocytic scar during Wallerian degeneration in the human spinal cord,” *Brain*, vol. 127, no. Pt 1, pp. 34–44, Jan. 2004.
- [142] M. O. Totoiu and H. S. Keirstead, “Spinal cord injury is accompanied by chronic progressive demyelination,” *J. Comp. Neurol.*, vol. 486, no. 4, pp. 373–383, Jun. 2005.
- [143] B. K. Kwon *et al.*, “Survival and regeneration of rubrospinal neurons 1 year after spinal cord injury,” *Proc. Natl. Acad. Sci. U. S. A.*, vol. 99, no. 5, pp. 3246–3251, Mar. 2002.

- [144] E. Park, A. A. Velumian, and M. G. Fehlings, "The role of excitotoxicity in secondary mechanisms of spinal cord injury: a review with an emphasis on the implications for white matter degeneration," *J. Neurotrauma*, vol. 21, no. 6, pp. 754–774, Jun. 2004.
- [145] D. Facon, A. Ozanne, P. Fillard, J.-F. Lepeintre, C. Tournoux-Facon, and D. Ducreux, "MR diffusion tensor imaging and fiber tracking in spinal cord compression," *AJNR Am. J. Neuroradiol.*, vol. 26, no. 6, pp. 1587–1594, Jun-Jul 2005.
- [146] S. Rajasekaran, R. M. Kanna, and A. P. Shetty, "Diffusion tensor imaging of the spinal cord and its clinical applications," *The Journal of Bone and Joint Surgery. British volume*, vol. 94-B, no. 8, pp. 1024–1031, 2012. doi: 10.1302/0301-620x.94b8.29618.
- [147] F. B. Mohamed *et al.*, "Diffusion tensor imaging of the pediatric spinal cord at 1.5 T: preliminary results," *AJNR Am. J. Neuroradiol.*, vol. 32, no. 2, pp. 339–345, 2011.
- [148] A. A. Deo, R. J. Grill, K. M. Hasan, and P. A. Narayana, "In vivo serial diffusion tensor imaging of experimental spinal cord injury," *J. Neurosci. Res.*, vol. 83, no. 5, pp. 801–810, Apr. 2006.
- [149] M. M. D'souza, A. Choudhary, M. Poonia, P. Kumar, and S. Khushu, "Diffusion tensor MR imaging in spinal cord injury," *Injury*, vol. 48, no. 4, pp. 880–884, Apr. 2017.
- [150] E. D. Schwartz *et al.*, "Apparent diffusion coefficients in spinal cord transplants and surrounding white matter correlate with degree of axonal dieback after injury in rats," *AJNR Am. J. Neuroradiol.*, vol. 26, no. 1, pp. 7–18, Jan. 2005.
- [151] M. D. Budde *et al.*, "Toward accurate diagnosis of white matter pathology using diffusion tensor imaging," *Magn. Reson. Med.*, vol. 57, no. 4, pp. 688–695, Apr. 2007.
- [152] M. D. Budde, J. H. Kim, H.-F. Liang, J. H. Russell, A. H. Cross, and S.-K. Song, "Axonal injury detected by in vivo diffusion tensor imaging correlates with neurological disability in a mouse model of multiple sclerosis," *NMR Biomed.*, vol. 21, no. 6, pp. 589–597, Jul. 2008.
- [153] A. A. Hofling, A. Alex Hofling, J. H. Kim, C. R. Fantz, M. S. Sands, and S.-K. Song, "Diffusion tensor imaging detects axonal injury and demyelination in the spinal cord and cranial nerves of a murine model of globoid cell leukodystrophy," *NMR in Biomedicine*, vol. 22, no. 10, pp. 1100–1106, 2009. doi: 10.1002/nbm.1420.
- [154] J. J. Herrera, T. Chacko, and P. A. Narayana, "Histological correlation of diffusion tensor imaging metrics in experimental spinal cord injury," *J. Neurosci. Res.*, vol. 86, no. 2, pp. 443–447, Feb. 2008.

- [155] S.-W. Sun, H.-F. Liang, K. Trinkaus, A. H. Cross, R. C. Armstrong, and S.-K. Song, “Noninvasive detection of cuprizone induced axonal damage and demyelination in the mouse corpus callosum,” *Magn. Reson. Med.*, vol. 55, no. 2, pp. 302–308, Feb. 2006.
- [156] P. Freund *et al.*, “MRI investigation of the sensorimotor cortex and the corticospinal tract after acute spinal cord injury: a prospective longitudinal study,” *Lancet Neurol.*, vol. 12, no. 9, pp. 873–881, Sep. 2013.
- [157] E. Datta, N. Papinutto, R. Schlaeger, A. Zhu, J. Carballido-Gamio, and R. G. Henry, “Gray matter segmentation of the spinal cord with active contours in MR images,” *Neuroimage*, vol. 147, pp. 788–799, Feb. 2017.
- [158] J. Cohen-Adad *et al.*, “7-T MRI of the spinal cord can detect lateral corticospinal tract abnormality in amyotrophic lateral sclerosis,” *Muscle Nerve*, vol. 47, no. 5, pp. 760–762, May 2013.
- [159] M. L. White, Y. Zhang, and K. Healey, “Cervical spinal cord multiple sclerosis: evaluation with 2D multi-echo recombined gradient echo MR imaging,” *J. Spinal Cord Med.*, vol. 34, no. 1, pp. 93–98, 2011.
- [160] J. Cohen-Adad, “What can we learn from T2* maps of the cortex?,” *Neuroimage*, vol. 93 Pt 2, pp. 189–200, Jun. 2014.
- [161] A. R. Martin *et al.*, “A Novel MRI Biomarker of Spinal Cord White Matter Injury: T2*-Weighted White Matter to Gray Matter Signal Intensity Ratio,” *AJNR Am. J. Neuroradiol.*, vol. 38, no. 6, pp. 1266–1273, Jun. 2017.
- [162] P. Grabher *et al.*, “Voxel-based analysis of grey and white matter degeneration in cervical spondylotic myelopathy,” *Sci. Rep.*, vol. 6, p. 24636, Apr. 2016.
- [163] F. M. Bareyre, M. Kerschensteiner, O. Raineteau, T. C. Mettenleiter, O. Weinmann, and M. E. Schwab, “The injured spinal cord spontaneously forms a new intraspinal circuit in adult rats,” *Nat. Neurosci.*, vol. 7, no. 3, pp. 269–277, Mar. 2004.

APPENDIX A

ASIA SCORING TEMPLATE

The International Standards for Neurological Classification of Spinal Cord Injury (ISNCSCI), referred to as the ASIA Impairment Scale (AIS), was developed by the American Spinal Injury Association (ASIA).

The neurological assessment based on this system is divided into motor and sensory examinations. During a sensory examination, a key point in each of the 28 dermatomes (figure 32) is tested bilaterally using light touch and pin-prick. A three-point scale of 0 to 2 is used for scoring. 0=absent, 1=impaired or partial appreciation, 2= normal or intact.

Deep anal pressure examinations include a gentle pressure to the anorectal wall by the examiner's finger. The pressure perceived from this exam is scored as absent or present.

Motor examination consists of testing key muscle functions of the myotomes (C5-T1) and (L2-S1). The scale of 0 to 5* is used for scoring motor functionality.

0= total paralysis

1= palpable contraction


2=active movement (full range of motion with no gravity)

3=active movement (full range of motion against gravity)

4= active movement (full range of motion against gravity and moderate resistance in a muscle specific position)

5= active movement (normal)= full range of motion against gravity and full resistance in a muscle specific position expected from an otherwise unimpaired person.

In addition, the ISNCSCI total motor score is considered as the sum of upper and lower extremity motor scores with the max of 100. Total sensory score is the sum of left and right sensory scores. The light touch and pinprick max scores are 112 for each category. The ISNCSCI total score is defined as the sum of total motor score and total sensory with the maximum score of 324.


 INTERNATIONAL STANDARDS FOR NEUROLOGICAL CLASSIFICATION OF SPINAL CORD INJURY (ISNCSCI)

Patient Name _____ Date/Time of Exam _____
 Examiner Name _____ Signature _____

RIGHT

MOTOR KEY MUSCLES

UER (Upper Extremity Right)

C2
C3
C4
C5
C6
C7
C8
T1


LER (Lower Extremity Right)

L2
L3
L4
L5
S1
S2
S3
S4-5

(VAC) Voluntary Anal Contraction (Yes/No)

RIGHT TOTALS (MAXIMUM)

UER + UEL = **UEMS TOTAL** (50)
 LER + LEL = **LEMS TOTAL** (25)



Key Sensory Points

SENSORY KEY SENSORY POINTS

Light Touch (LTR) Pin Prick (PPR)

C2
C3
C4
C5
C6
C7
C8
T1
T2
T3
T4
T5
T6
T7
T8
T9
T10
T11
T12
L1
L2
L3
L4
L5
S1
S2
S3
S4-5

SENSORY SUBSCORES

LTR + LTL = **LT TOTAL** (56)
 PPR + PPL = **PP TOTAL** (56)

LEFT

MOTOR KEY MUSCLES

UEL (Upper Extremity Left)

C5 Elbow flexors
C6 Wrist extensors
C7 Elbow extensors
C8 Finger flexors
T1 Finger abductors (5th finger)

LEL (Lower Extremity Left)

L2 Hip flexors
L3 Knee extensors
L4 Ankle dorsiflexors
L5 Long toe extensors
S1 Ankle plantar flexors

S2
S3
S4-5 (DAP) Deep Anal Pressure (Yes/No)

LEFT TOTALS (MAXIMUM)

UEL + UEL = **UEMS TOTAL** (50)
 LEL + LEL = **LEMS TOTAL** (25)

NEUROLOGICAL LEVELS

1. SENSORY R L
 2. MOTOR R L

3. NEUROLOGICAL LEVEL OF INJURY (NLJ)

4. COMPLETE OR INCOMPLETE?
 Incomplete - Any sensory or motor function in S4-5

5. ASIA IMPAIRMENT SCALE (AIS)

(In complete motor only)
ZONE OF PARTIAL PRESERVATION
 Most caudal level with any innervation

SENSORY R L
 MOTOR R L

This form may be copied freely but should not be altered without permission from the American Spinal Injury Association. REV 04/15

Figure 32: The figure illustrates actual scoring template used for neurological assessment of SCI patients. The figure is adapted from the <https://asia-spinalinjury.org/>

APPENDIX B

ROI NAMES

The list of 34 ROI names that was used from the WM atlas in Article-2. All regions of interest have both a left (L) and right (R) label.

FG: fasciculus gracilis; **FC**: fasciculus cuneatus; **ICST**: lateral corticospinal tract; **vSCT**: ventral spinocerebellar tract; **RST**: rubrospinal tract; **IRST**: lateral reticulospinal tract; **SL**: spinal lemniscus (spinothalamic and spinoreticular tracts); **SOT**: spino-olivary tract; **vIRST**: ventrolateral reticulospinal tract; **IVST**: lateral vestibulospinal tract; **vRST**: ventral reticulospinal tract; **vCST**: ventral corticospinal tract; **TST**: tectospinal tract; **mRST**: medial reticulospinal tract; **mLF**: medial longitudinal tract; **WM**: white matter; **DF**: dorsal column; **LF**: lateral funiculi; **VF**: ventral funiculi.

APPENDIX C

GROUP REGIONS NAMES

WM dorsal column: **DF** (FG+ FC)

WM lateral funiculi: **LF** (ICST+ vSCT+ RST+ IRST+ SL)

WM ventral funiculi: **VF** (SOT+ vIRST+ IVST+ vRST+ vCST+ TST+ mRST+ mLF)

WM: **DF+ LF+ VF**

APPENDIX D

PERMISSION LETTER FOR INCLUSION OF COPYRIGHTED MATERIAL



This is a License Agreement between Shiva Shahrampour ("User") and Copyright Clearance Center, Inc. ("CCC") on behalf of the Rightsholder identified in the order details below. The license consists of the order details, the Marketplace Permissions General Terms and Conditions below, and any Rightsholder Terms and Conditions which are included below.
All payments must be made in full to CCC in accordance with the Marketplace Permissions General Terms and Conditions below.

Order Date	29-May-2023	Type of Use	Photocopy for library reserves
Order License ID	1359841-1	Publisher	WILLIAMS & WILKINS CO.;
ISSN	0195-6108		American Society of Neuroradiology

LICENSED CONTENT

Publication Title	AJNR, American journal of neuroradiology	Country	United States of America
Author/Editor	AMERICAN SOCIETY OF NEURORADIOLOGY., AMERICAN ROENTGEN RAY SOCIETY.	Rightsholder	American Society of Neuroradiology
Date	01/01/1980	Publication Type	Journal
Language	English		

REQUEST DETAILS

Publication Year of Title Being Used	2021	Number of Copies	1
Total Number of Pages	7	Currency	USD

ADDITIONAL DETAILS

Article/Chapter	Atlas-Based Quantification of DTI Measures in a Typically Developing Pediatric Spinal Cord	Your Reference	N/A
-----------------	--	----------------	-----